Physico-Chemical Studies of Co-ordination Complexes of the Platinum Group Metals

Eric J. L. McInnes

Ph.D. Thesis

University of Edinburgh

1995

Declaration

Except where specific reference is made to other sources, the work presented in this thesis is the original work of the author. It has not been submitted, in whole or in part, for any other degree.

Eric McInnes.

Abstract

This thesis is concerned with the electrochemistry and spectroscopy of redox-active late transition metal complexes of the 2,2'-bipyridine ligand (bpy) and their reduction products.

Complexes of general formula [Pt(4,4'-X_2-bpy)L_2] (where L is a non redox-active ligand and X=NH_2, OEt, Me, H, Ph, Cl, CO_2Me) undergo two one-electron reductions as revealed by cyclic voltammetry. The absorption spectra of the one-electron reduction products reveal the first of these reductions to be localised on the bpy ligand giving rise to radical anion ligand complexes of Pt(II). Epr spectra of the reduced, seventeen-electron species indicate a significant (*ca.* 10%) admixture of metal 5d orbitals in the SOMO, in good agreement with EHMO calculations. Both the $E_{1/2}$ value of the first reduction process and the MLCT ν_{max} value vary linearly with the Hammett parameter of the substituent X. The second reduction electron spin-pairs with the first in the same π^* orbital. The LUMO of [Pd(4,4'-X_2-bpy)Cl_2] is Pd 4d based and these complexes undergo chemically irreversible two-electron reductions.

Complexes of the 4,4'-$(NO_2)_2$-bpy ligand undergo up to four one-electron reductions. Epr spectroscopy of the di-reduction products of [M(4,4'-$(NO_2)_2$-bpy)L_2] (M=Pd, Pt, $L=Cl^-$; M=Rh, L_2=1,5-cod) shows that spin-triplet species are formed on di-reduction and consequently that the LUMO-SLUMO gap is smaller than the spin-pairing energy for these complexes. The redox-active orbitals are highly localised on the nitro-groups. EHMO calculations are in good agreement.

$[Pt(bpy)_2]^{2+}$ undergoes a redox-induced dimerisation reaction at room temperature. Low-temperature cyclic voltammetry reveals the redox-active orbital to be bpy-based.

The single-crystal x-ray structures of [Pt(4,4'-$(NO_2)_2$-bpy)Cl_2] and [Au(bpy)Cl_2]BF_4 are reported.

List of Abbreviations

a_{iso}	isotropic ligand superhyperfine coupling constant (Gauss or cm^{-1})
a^2	metal d-orbital admixture to SOMO
A	absorbance (arbitary units)
A_i	anisotropic metal hyperfine coupling constant (Gauss or cm^{-1})
A_{iso}	isotropic metal hyperfine coupling constant (Gauss or cm^{-1})
<A>	averaged anisotropic metal hyperfine coupling constant (Gauss or cm^{-1})
bpy	2,2'-bipyridine
cod	1,5-cyclooctadiene
DMF	N,N-dimethylformamide
DMSO	dimethylsulphoxide
EHMO	extended Hückel molecular orbital
en	ethylenediamine
epr	electron paramagnetic resonance
Et	ethyl
E_f, E_r	potentials of forward and return peaks in cyclic voltammogram (Volts)
eV	electron volts
$E_{1/2}$	half-wave potential (=$(E_f+E_r)/2$) (Volts)
g_i	anisotropic g value
g_e	free electron g value (2.0023)
g_{iso}	isotropic g value
G	Gauss
HOMO	highest-occupied molecular orbital

i	current (arbitary units)
I	nuclear spin quantum number
ir	infra-red
J_{PPt}	^{31}P-^{195}Pt nuclear coupling constant (Hertz)
L	ligand
LF	ligand field
LUMO	lowest-unoccupied molecular orbital
M	mol dm^{-3} or transition metal
Me	methyl
MLCT	metal-to-ligand charge transfer
mnt	maleonitriledithiolate
nir	near infra-red
nmr	nuclear magnetic resonance
OTE	optically transparent electrode
Ph	phenyl
ppm	parts per million
py	pyridine
P_d	electron-nuclear dipolar coupling parameter
$^{31}P\{^{1}H\}$	^{1}H decoupled ^{31}P nmr
RR	resonance-enhanced Raman
S	solvent
SCE	standard calomel electrode
SLUMO	second-lowest-unoccupied molecular orbital
SOMO	singly-occupied molecular orbital
TBA	tetrabutylammonium
THF	tetrahydrofuran
uv	ultra-violet
vis	visible

V	Volts
X	substituent
δ	chemical shift (ppm)
Δ	crystal field splitting energy
Δg_i	shift of g_i from g_e
ε	extinction coefficient ($M^{-1}cm^{-1}$)
σ_p	Hammett parameter
υ_{max}	energy of absorption maximum (cm^{-1})
I	$[Pt(bpy)Cl_2]$
II	$[Pt(bpy)(NH_3)_2]^{2+}$
III	$[Pt(bpy)(en)]^{2+}$
IV	$[Pt(bpy)(py)_2]^{2+}$
V	$[Pt(bpy)(PMe_3)_2]^{2+}$
VI	$[Pt(bpy)(CN)_2]$
VII	$[Pt(4,4'\text{-}(NH_2)_2\text{-}bpy)Cl_2]$
VIII	$[Pt(4,4'\text{-}(OEt)_2\text{-}bpy)Cl_2]$
IX	$[Pt(4,4'\text{-}Me_2\text{-}bpy)Cl_2]$
X	$[Pt(4,4'\text{-}Ph_2\text{-}bpy)Cl_2]$
XI	$[Pt(4,4'\text{-}Cl_2\text{-}bpy)Cl_2]$
XII	$[Pt(4,4'\text{-}(CO_2Me)_2\text{-}bpy)Cl_2]$
XIII	$[Pt(4,4'\text{-}(NO_2)_2\text{-}bpy)Cl_2]$
XIV	$[Pd(4,4'\text{-}(NO_2)_2\text{-}bpy)Cl_2]$
XV	$[Rh(4,4'\text{-}(NO_2)_2\text{-}bpy)(cod)]^+$
XVI	$[Re(4,4'\text{-}(NO_2)_2\text{-}bpy)(CO)_3Cl]$
XVII	$[Pt(bpy)_2]^{2+}$

Contents

	Page
Abstract	i
Abbreviations	ii
Contents	v
List of Figures	vii
List of Tables	x
Chapter 1. Introduction	1
Chapter 2. Experimental	8
2.1 Syntheses and Chemicals	8
2.2 X-ray Crystallography	10
2.3 EHMO Calculations	11
2.4 Electrochemistry and Spectroelectrochemistry	12
Chapter 3. (2,2'-bipyridine)bis(L)platinum(II), $[Pt(bpy)L_2]$	15
3.1 Introduction	15
3.2 EHMO Calculations	17
3.3 Redox Chemistry	18
3.4 Uv/vis/nir Spectroelectrochemistry	19
3.5 Epr Spectroelectrochemistry	23
3.6 Redox Chemistry of $[Pd(bpy)Cl_2]$	33
3.7 Conclusions	33
Chapter 4. (4,4'-X_2-2,2'-bipyridine)dichloroplatinum(II), $[Pt(4,4'-X_2-bpy)Cl_2]$	35
4.1 Introduction	35
4.2 4,4'-X_2-bipyridine Ligands	36
4.3 Synthesis of $[Pt(4,4'-X_2-bpy)Cl_2]$	37
4.4 Redox Chemistry of $[Pt(4,4'-X_2-bpy)Cl_2]$	38
4.5 Uv/vis/nir Spectroelectrochemistry	40

4.6 Epr Spectroelectrochemistry 44
4.7 Redox Chemistry of [Pd(4,4'-$(CO_2Me)_2$-bpy)Cl_2] 46
4.8 Conclusions 48
Chapter 5. Complexes of 4,4'-dinitro-2,2'-bipyridine 49
5.1 Introduction 49
5.2 Redox Chemistry of 4,4'-$(NO_2)_2$-bpy 49
5.3 Synthesis of $[M(4,4'-(NO_2)_2\text{-bpy})L_2]^{n+}$ 50
5.4 Redox Chemistry of $[M(4,4'-(NO_2)_2\text{-bpy})L_2]^{n+}$ 51
5.5 Crystal Structure of [Pt(4,4'-$(NO_2)_2$-bpy)Cl_2] 56
5.6 EHMO Calculations of **I** *versus* **XIII** 58
5.7 Epr Spectroelectrochemistry 60
5.8 Uv/vis/nir Spectroelectrochemistry 68
5.9 Conclusions 69
Chapter 6. $[Bis(2,2'\text{-bipyridine})platinum(II)]^{2+}$ 73
6.1 Introduction 73
6.2 Redox Chemistry and Spectroelectrochemistry 74
6.3 Conclusions 81
Conclusions and Discussion 82
Appendix A. Structure of [Pt(4,4'-$(NO_2)_2$-bpy)Cl_2] 84
Appendix B. Structure of (2,2'-bipyridine)dichlorogold(III) tetrafluoroborate 89
Acknowledgements 95
References 96

List of Figures

Figure	Page
1.1 Structure and numbering scheme of 2,2'-bipyridine	1
1.2 d-orbital manifold splitting in an octahedral, tetragonally distorted and square-planar environment	2
1.3 $[M(mnt)_2]^{n-}$ (d^7, M=Ni, Pd, Pt, Co, Rh ; d^9, M=Ni, Pd, Cu, Au)	2
1.4 Uv/vis/nir spectra of $Na^+(bpy^-)$ and $[Ru(bpy)_3]^-$	4
1.5 $[M(4,4'\text{-}X_2\text{-}bpy)L_2]$	7
2.1 Schematic representation of OTE cell	13
3.1 Cyclic voltammogram of $[Pt(bpy)Cl_2]$ in 0.1 M $TBABF_4$/DMF at 293 K	19
3.2 OTE reduction of $\mathbf{I}^{0/-}$ in 0.1 M $TBABF_4$/DMF at 243 K	21
3.3 Uv/vis/nir spectra of **IV**$^-$ (a) and **VI**$^-$ (b) in 0.1 M $TBABF_4$/DMF at 243 K	22
3.4 Solution epr spectrum of **III**$^-$ in DMF at 293 K	24
3.5 Solution epr spectrum of **VI**$^-$ in DMF at 293 K (a) and simulation (b)	25
3.6 77 K X-band epr spectra of **I**$^-$ electrochemically generated in 0.1 M $TBABF_4$/DMF (a), chemically generated with $NaBH_4$ (b) and simulation using the parameters in table 3.5 with Gaussian half linewidths of 10 G, 12 G and 30 G for g_1, g_2 and g_3 respectively (c)	28
3.7 77 K X-band epr spectrum of **IV**$^-$ in 0.1 M $TBABF_4$/DMF (a) and simulation using the parameters in table 3.5 with Gaussian half linewidths of 9 G, 10 G and 18 G for g_1, g_2 and g_3 respectively (b)	29
3.8 77 K X-band epr spectrum of **V**$^-$ in 0.1 M $TBABF_4$/DMF	30
3.9 77 K X-band epr spectrum of **VI**$^-$ in 0.1 M $TBABF_4$/DMF (a), 150 K Q-band epr spectrum in DMF (b) and simulation using the parameters in table 3.5 with Gaussian half linewdiths of 12 G, 11 G and 26 G for g_1, g_2 and g_3 respectively (c)	32
3.10 Cyclic voltammogram of $[Pd(bpy)Cl_2]$ in 0.1 M $TBABF_4$/DMF at 293 K	33
4.1 Cyclic voltammogram of **VII** at 213 K in 0.1 M $TBABF_4$/DMF	39

4.2 Cyclic voltammogram of **XII** at 293 K in 0.1 M $TBABF_4$/DMF 39

4.3 Graph of E_1 of [Pt(4,4'-X_2-bpy)Cl_2] *versus* Hammett parameter σ_p 40

4.4 Uv/vis spectrum of **XII** in DMF solution 41

4.5 Graph of MLCT ν_{max} of [Pt(4,4'-X_2-bpy)Cl_2] *versus* Hammett parameter σ_p 42

4.6 OTE reduction of $\mathbf{XII}^{0/-}$ in 0.1 M $TBABF_4$/DMF at 243 K 43

4.7 77 K X-band epr spectra of $\mathbf{VIII}^-$ (a) and $\mathbf{XII}^-$ (b) in 0.1 M $TBABF_4$/DMF 47

5.1 Cyclic voltammogram of 4,4'-$(NO_2)_2$-bpy in 0.1 M $TBABF_4$/DMF at 293 K 50

5.2 Cyclic voltammograms of **XIII** (a) and **XIV** (b) in 0.1 M $TBABF_4$ /DMF at 293 K 52

5.3 Cyclic voltammograms of **XV** in 0.5 M $TBABF_4/CH_2Cl_2$ at 293 K 54

5.4 Cyclic voltammogram of **XVI** in 0.1 M $TBABF_4$/MeCN at 293 K 56

5.5 Crystal Structure of **XIII** 58

5.6 Energy level scheme for **I** and **XIII** 59

5.7 Solution (a) and frozen glass (b) X-band epr spectra of $\mathbf{XIII}^-$ in 0.1 M $TBABF_4$/DMF 61

5.8 Solution epr spectrum of $\mathbf{XIII}^{2-}$ in 0.1 M $TBABF_4$/DMF at 293 K (a) and simulation (b) 63

5.9 77 K X-band epr spectrum of $\mathbf{XIII}^{2-}$ in 0.1 M $TBABF_4$/DMF 64

5.10 77 K X-band epr spectra of $\mathbf{XIV}^-$ in DMF (a) and $\mathbf{XV}^-$ in CH_2Cl_2 (b) 65

5.11 Soltuion (a) and frozen glass (b) X-band epr spectra of $\mathbf{XIV}^{2-}$ in 0.1 M $TBABF_4$/DMF 66

5.12 CH_2Cl_2 solution epr spectrum of $\mathbf{XV}^{2-}$ at 293 K (a) and simulation (b) 67

5.13 Uv/vis spectra of **XIII** (a) and **XIV** (b) in DMF solution at 293 K 70

5.14 Uv/vis/nir spectra of $\mathbf{XIII}^-$ (a) and $\mathbf{XIV}^-$ (b) in 0.1 M $TBABF_4$/DMF at 243 K 71

5.15 OTE reduction of **XIII**$^{-/2-}$ (a) and **XIV**$^{-/2-}$ (b) in 0.1 M $TBABF_4$/DMF at 243 K 72

6.1 Distortions of the $[Pt(bpy)_2]^{2+}$ cation 73

6.2 Cyclic voltammograms of **XVII** in 0.1 M $TBABF_4$/DMF at 293 K 75

6.3 Cyclic voltammogram of "**XVII**" in 0.1 M $TBABF_4$/DMF at 293 K 76

6.4 OTE reduction of **XVII**→"**XVII**" in 0.1 M $TBABF_4$/DMF at 293 K 77

6.5 Uv/vis/nir spectrum of di-reduced dimeric species 77

6.6 77 K epr spectrum of di-reduced dimeric species 78

6.7 Cyclic voltammograms of **XVII** in 0.1 M $TBABF_4$/DMF at 213 K 80

A.1 Packing of $[Pt(4,4'\text{-}(NO_2)_2\text{-}bpy)Cl_2]$ 84

A.2 Packing of $[Pt(4,4'\text{-}(NO_2)_2\text{-}bpy)Cl_2]$ 85

A.3 Packing of $[Pt(4,4'\text{-}(NO_2)_2\text{-}bpy)Cl_2]$ 86

B.1 Structure of $[Au(bpy)Cl_2]BF_4$ 91

List of Tables

Table	Page
1.1 Redox potentials of $[M(mnt)_2]^{n-}$	5
2.1 Synthesis conditions and analyses of $[Pt(4,4'\text{-}X_2\text{-}bpy)Cl_2]$	9
3.1 Nuclear coefficients to LUMO of $[Pt(bpy)L_2]$	18
3.2 Redox potentials of $[Pt(bpy)L_2]$ in 0.1 M $TBABF_4$/DMF at 293 K	19
3.3 Uv/vis spectra of $[Pt(bpy)L_2]$ in DMF solution at 293 K	20
3.4 Uv/vis/nir spectra of $[Pt(bpy)L_2]^-$ in 0.1 M $TBABF_4$/DMF at 243 K	23
3.5 Epr parameters for $[Pt(bpy)L_2]^-$	26
3.6 Pt $5d_{yz}$ orbital admixtures to the SOMO of $[Pt(bpy)L_2]^-$	31
4.1 Redox potentials of 4,4'-X_2-bpy in 0.1 M $TBABF_4$/DMF at 293 K	37
4.2 Redox potentials of $[Pt(4,4'\text{-}X_2\text{-}bpy)Cl_2]$ in 0.1 M $TBABF_4$/DMF	38
4.3 MLCT ν_{max} of $[Pt(4,4'\text{-}X_2\text{-}bpy)Cl_2]$ in DMF solution	41
4.4 Uv/vis/nir spectra of $[Pt(4,4'\text{-}X_2\text{-}bpy)Cl_2]^-$ in 0.1 M $TBABF_4$/DMF at 243 K	44
4.5 Epr parameters for $[Pt(4,4'\text{-}X_2\text{-}bpy)Cl_2]^-$	45
4.6 Pt $5d_{yz}$ orbital admixtures to the SOMO of $[Pt(4,4'\text{-}X_2\text{-}bpy)Cl_2]^-$	46
5.1 Redox potentials of $[M(4,4'\text{-}(NO_2)_2\text{-}bpy)L_2]^{n+}$	53
5.2 Interatomic distances (Å) and interbond angles (°) for **XIII**	56
5.3 Nuclear coefficients of LUMO and SLUMO of **XIII**	59
A.1 Fractional atomic co-ordinates for **XIII**	87
B.1 Fractional atomic co-ordinates and equivalent isotropic displacement parameters ($Å^2$) for $[Au(bpy)Cl_2]BF_4$	93
B.2 Interatomic distances (Å) and interbond angles (°) for $[Au(bpy)Cl_2]BF_4$	94

Chapter 1. Introduction

The fascinating electrochemical, photophysical and photoelectrochemical properties of transition metal complexes of 2,2'-bipyridine (bpy, figure 1.1) have led to their use as, for example, photosensitisers, photocatalysts and catalysts.[1] Much of the interesting chemistry is related to bpy's ability to stabilise both very high and very low formal oxidation states where it acts as a π-donor and π-acceptor respectively.[1]

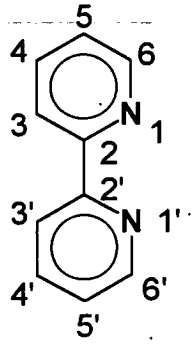

Figure 1.1 2,2'-Bipyridine

This thesis is concerned with the redox chemistry and spectroscopy of sixteen-electron, square planar d^8 bpy complexes of some late transition metals - namely platinum, palladium and rhodium - and their redox related species. The sixteen-electron rule dictates that the d^8 parent species are relatively stable and such compounds are important in, for example, catalysis (Wilkinson's catalyst) and medicinal chemistry (cis-platin). Thus, square planar complexes of Rh(I), Ir(I), Pd(II), Pt(II) and Au(III) are all common.[2] By contrast the related seventeen-electron d^9 species are very rare for second and third row transition metals due to the large crystal field splitting energy, Δ (figure 1.2). Indeed most formal Pt(I) complexes are diamagnetic binuclear species.[2]

However, it is often possible to stabilise the seventeen-electron species by use of a highly electron-withdrawing or conjugated ligand set, thus stabilising the "extra" electron. It is then often easier to access the possibly unstable seventeen-electron system by the electrochemical one-electron reduction of the stable sixteen-electron precursor. For example the bis(maleonitriledithiolate) transition metal complexes can allow isolation of

up to three different formal oxidation states for one particular metal, where the d^7 and d^9 species can be generated from the d^8 complexes (figure 1.3).[3-8]

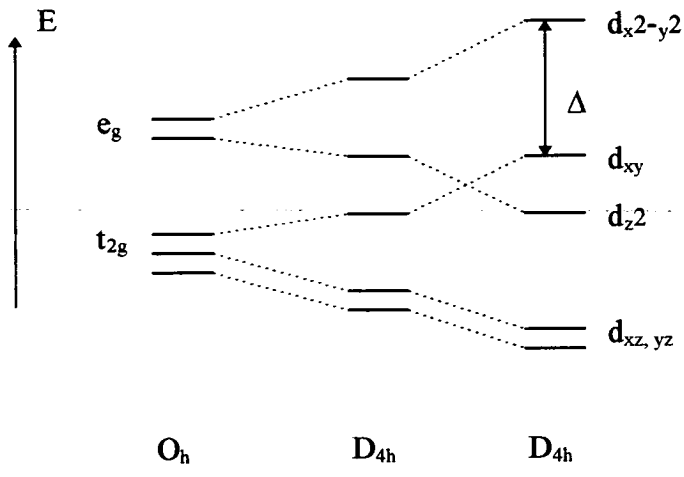

Figure 1.2 d-orbital manifold splitting in an octahedral, tetragonally distorted and square-planar environment.

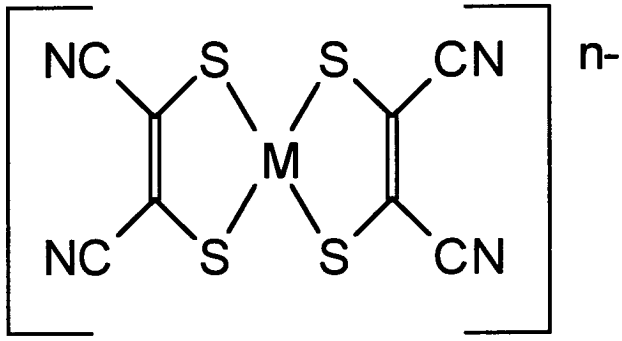

Figure 1.3 $[M(mnt)_2]^{n-}$ (d^7, M=Ni, Pd, Pt, Co, Rh ; d^9, M=Ni, Pd, Cu, Au)

Where a redox-active ligand such as maleonitriledithiolate (mnt) or bpy is coordinated to a transition metal centre the one-electron reduction products are often characterised by one of two extreme descriptions: (i) a d^9 metal complex, *i.e.* the unpaired electron resides at the metal, or (ii) a ligand anion radical complex of a d^8 metal centre, *i.e.* the unpaired electron resides on the ligand set.[9] However, it is usually the case that neither description is satisfactory and a delocalised molecular orbital approach is necessary.

Spectroelectrochemical techniques, *i.e.* the coupling of an electrochemical technique to a spectroscopic method, naturally lend themselves to the characterisation of such species. Ultra-violet/visible/near infra-red (uv/vis/nir),[10] infra-red (ir),[11] electron paramagnetic resonance (epr),[12] and resonance-Raman (RR)[13] spectroscopies have all been used in this manner. Two examples where a combination of spectroelectrochemical techniques have been used to electronically characterise redox-active systems are given below.

(i) The series of redox-related complexes $[Ru(bpy)_3]^{2+/+/0/-}$ has been studied *via in situ* uv/vis/nir, RR and epr spectroelectrochemistry. $[Ru(bpy)_3]^{2+}$ undergoes three reversible one-electron reductions at -1.27, -1.46 and -1.70 V *vs.* SCE in 0.1M $TBABF_4$/MeCN solution as shown by cyclic voltammetry.[14] The uv/vis/nir spectrum of the fully reduced species $[Ru(bpy)_3]^-$ characterised it as $[Ru^{II}(bpy^-)_3]^-$ due to the similarity of the spectrum to that of the ion-pair $Na^+(bpy^-)$ (figure 1.4),[10,15] *i.e.* the reduction electrons enter the bpy π^* orbitals resulting in a Ru^{II} complex of coordinated radical anion bpy^- ligands. It was further concluded from the uv/vis/nir spectra of the intermediate species $[Ru(bpy)_3]^{+/0}$ which contained bands characteristic of $[Ru(bpy)_3]^{2+}$ and $[Ru(bpy^-)_3]^-$ that these complexes were best formulated with discrete bpy and bpy^- ligands, *i.e.* $[Ru^{II}(bpy)_2(bpy^-)]^+$ and $[Ru^{II}(bpy)(bpy^-)_2]^0$, rather than charge-averaged models. A similar series of uv/vis/nir spectra is observed for $[Ir(bpy)_3]^{3+/2+/+/0}$.[16]

Yellowlees *et al.* have concluded from such studies that the following absorption bands are diagnostic for the presence of coordinated bpy^-: (i) a nir band at *ca.* 10 kcm^{-1} comprising of three peaks (or shoulders), (ii) a doublet visible band at *ca.* 20 kcm^{-1}, and (iii) an intense near uv band at *ca.* 25 kcm^{-1}.[16]

The charge localised model was confirmed by *in situ* RR spectroelectrochemical studies on $[Ru(bpy)_3]^+$ where vibrational modes of both bpy and bpy^- are observed, characterised by the RR spectra of $[Ru(bpy)_3]^{2+}$ and $[Ru(bpy^-)_3]^-$ respectively.[13]

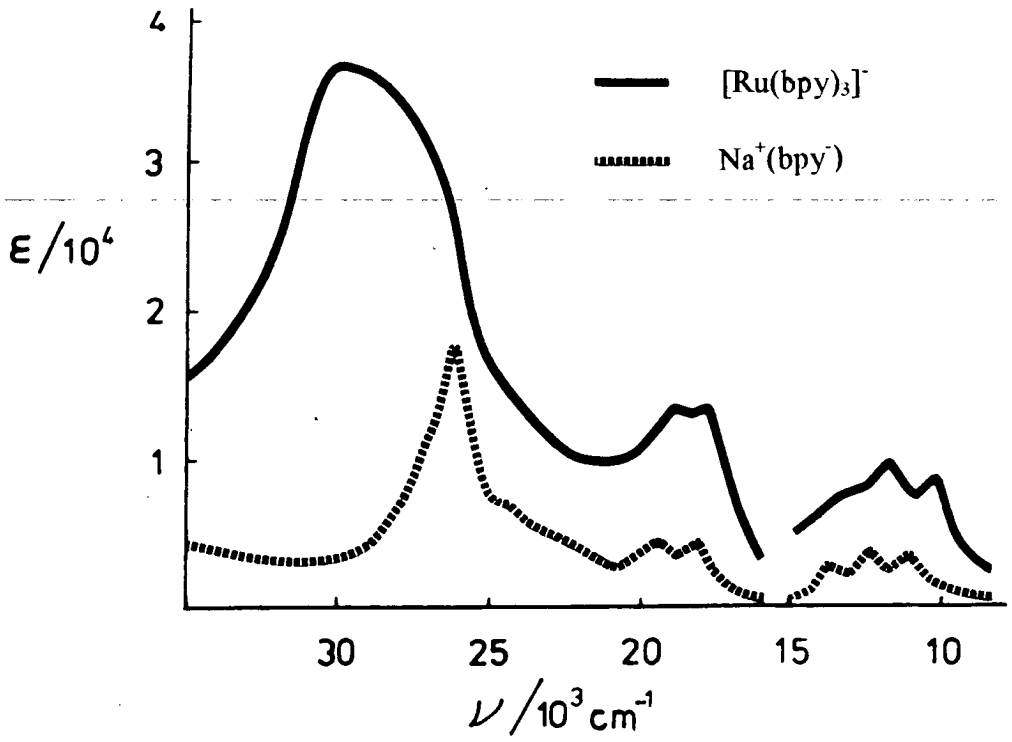

Figure 1.4. Uv/vis/nir spectra of $Na^+(bpy^-)$ and $[Ru(bpy)_3]^-$

De Armond *et al.* studied the epr spectra of the paramagnetic complexes $[Ru(bpy)_3]^{+/0/-}$. In each case signals close to g=2.00 were observed confirming ligand-based radicals (a metal-based radical would result in a large g-shift from the free electron value of g_e=2.0023).[17,18] The observation of temperature dependent line-broadening due to electron-hopping between chelate rings in the solution epr spectra of $[Ru(bpy)_3]^+$ and $[Ru(bpy)_3]^0$ (no such line-broadening is observed for $[Ru(bpy)_3]^-$) supported the charge-localised model and De Armond was able to estimate energy barriers for the electron-hopping process from variable temperature epr studies. This was further backed by the apparently non-interacting nature of the two added electrons in the epr spectrum of $[Ru(bpy)_3]^0$.

(ii) The family of complexes $[M(mnt)_2]^{n-}$ (M=Ni, Pd, n=1, 2, 3; M=Pt, Au, n=1, 2) have been extensively studied by epr spectroelectrochemistry, single-crystal epr spectroscopy and, more recently, by ir spectroelectrochemistry. These studies reveal the extent of mixing of metal and ligand orbitals in the paramagnetic formally d^7 and d^9 complexes which have been chemically or electrochemically generated from the diamagnetic d^8 complexes. Table 1.1 summarises the redox chemistry of these complexes.

Table 1.1 Redox potentials of $[M(mnt)_2]^{n-}$

M	0/-[a]	-/2-	2-/3-
Ni[b]	-	-0.14	-1.94
Pd[b]	-	+0.04	-2.17
Pt[b]	-	-0.16	-
Au[c]	+1.51	-0.41	-

(a) redox couple, E in V

(b) *vs.* Ag/AgCl in 0.1M $NaClO_4$/MeCN solution, reference 19

(c) *vs.* SCE in 0.1M $TBABF_4$/DMSO solution, reference 5

Geiger *et al.* reported the epr spectra of the formally d^9 $[M(mnt)_2]^{3-}$ (M=Ni, Pd) complexes generated by the one-electron reduction of $[M(mnt)_2]^{2-}$. The epr spectrum of 90% ^{61}Ni enriched $[Ni(mnt)_2]^{3-}$ in a frozen MeCN solution showed rhombic g ($g_1 \neq g_2 \neq g_3 > g_e$) and ^{61}Ni (spin, I=3/2) hyperfine tensors with $A_1=-53\times10^{-4}$ cm^{-1}, $A_2=\pm5.8\times10^{-4}$ cm^{-1} and $A_3=\pm5.8\times10^{-4}$ cm^{-1}.[6] From these parameters the Ni 3d orbital contribution to the singly-occupied molecular orbital (SOMO) was calculated to be in the range 70-85% depending on the signs of A_2 and A_3. Thus, assignment as a genuine d^9 metal complex with little metal-ligand covalency seems reasonable. Both the solution and frozen glass spectra of $[Pd(mnt)_2]^{3-}$ showed hyperfine coupling of the unpaired electron to the ^{105}Pd nucleus in natural abundance (22%, I=5/2) with $A_{iso}=+30\times10^{-4}$ cm^{-1}, $A_1=+44\times10^{-4}$ cm^{-1}, $A_2=+29\times10^{-4}$ cm^{-1} and $A_3=+26\times10^{-4}$ cm^{-1}.[6] Calculations from the spectra reveal a metal 4d orbital contribution to the SOMO of 45% and it was concluded that considerably more covalency existed for the Pd complex than the Ni analogue.

Single-crystal epr studies on $[Au(mnt)_2]^{2-}$ concluded a still smaller metal character of 15% in the SOMO.[5] Thus, this complex is clearly more accurately described as a ligand-based radical rather than a Au^{II} complex. This formulation was supported by ir spectroelectrochemical measurements which showed the CN stretch of the mnt ligands to red-shift by 12 cm^{-1} on reduction of $[Au(mnt)_2]^-$ to $[Au(mnt)_2]^{2-}$, *i.e.* the reduction electron is considerably delocalised onto the π^* anti-bonding orbitals of the CN moieties.[11]

Solution epr spectra of $[M(mnt)_2]^-$ (M=Ni, Pd, Pt) reveal hyperfine coupling of the unpaired electron to the metal nuclei in each case with A_{iso}=4.5 G ($M=^{61}Ni$ enriched), 7.7 G ($M=^{105}Pd$) and 82 G ($M=^{195}Pt$, 34% natural abundance, I=1/2).[20] Single-crystal epr studies reveal rhombic g ($g_1 \neq g_2 > g_e > g_3$) and metal hyperfine tensors.[3,21,22] The metal d orbital admixtures in the SOMOs of these formally d^7 complexes are calculated to be 24, 21 and 34% for M=Ni, Pd and Pt respectively, *i.e.* in each case there is extensive metal-ligand covalency. These results are supported by ir spectroelectrochemical experiments which show the CN stretch of the mnt ligands to blue-shift by *ca.* 15 cm^{-1} on oxidation of $[M(mnt)_2]^{2-}$ to $[M(mnt)_2]^-$ in each case.[11]

In this work the redox chemistry and absorption uv/vis spectra of a series of simple complexes of general formula $[M(4,4'\text{-}X_2\text{-bpy})L_2]$ ($M=Pt^{II}$, Pd^{II} and Rh^{I}) where L is a non redox-active ligand have been studied and the spectroscopy (uv/vis/nir, epr) of the derived one-electron reduction products studied in order to electronically characterise the seventeen-electron species. The effect of systematic variations in both the "trans" ligand L (X=H) and the substituent X ($L=Cl^-$) are studied with a view to observing the effect of changes in the ligand set on the frontier orbitals of the complex.

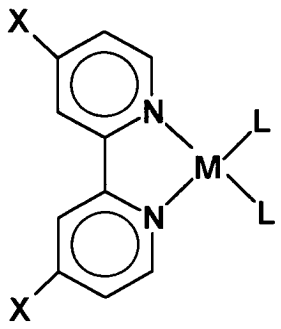

Figure 1.5. [M(4,4'-X_2-bpy)L_2]

Chapter 2. Experimental

2.1 Syntheses and Chemicals

CH_2Cl_2 was pretreated with KOH pellets then distilled over P_2O_5 prior to use. N,N'-dimethylformamide (DMF, hplc grade, Aldrich) was used as supplied. MeCN was distilled over CaH_2 prior to use.

Bpy, 4,4'-Me_2-bpy and 4,4'-Ph_2-bpy (Ph=phenyl) were commercially available (Aldrich). All other ligands were prepared by literature methods.[23-27] $[Pt(bpy)Cl_2]$,[28] $[Pt(bpy)(NH_3)_2](PF_6)_2$,[29] $[Pt(bpy)(en)](BF_4)_2$,[30] $[Pt(bpy)(py)_2](BF_4)_2$,[30] $[Pt(bpy)(CN)_2]$,[30] $[Pt(4,4'\text{-}Me_2\text{-}bpy)Cl_2]$,[30] $[Re(4,4'\text{-}(NO_2)_2\text{-}bpy)(CO)_3Cl]$,[31] $[Pt(bpy)_2](BF_4)_2$[32] and $[Pd(bpy)Cl_2]$[33] (en=ethylenediamine, py=pyridine) were all prepared by literature methods. A minor change from the literature preparations was the replacement of $NaClO_4$ by $NaBF_4$.

$[Pt(bpy)(PMe_3)_2](BF_4)_2$ was prepared as follows. 1.0M PMe_3 in THF solution (2.2 ml, $2.2x10^{-3}$ mol PMe_3) was syringed into a $N_{2(g)}$ saturated suspension of $[Pt(bpy)Cl_2]$ (0.455 g, $1.08x10^{-3}$ mol) in H_2O (50 ml) and heated under reflux in an atmosphere of $N_{2(g)}$ with stirring until the suspension had all dissolved to give a yellow solution. Addition of $NaBF_4$ (0.5 g, excess) yielded an immediate yellow precipitate which was collected, washed with H_2O and air dried. Recrystallisation twice from H_2O gave yellow needles of the desired product (0.45 g, 62%). C:H:N 28.36%:3.19%:5.15% (predicted 28.38%:3.88%:4.14%). $^{31}P\{^1H\}$ nmr in CD_3NO_2 : singlet at δ=-27.46 ppm with ^{195}Pt satellites, J_{PPt}=3423 Hz. $^{31}P\{^1H\}$ nmr spectrum recorded on a Bruker WP200SY spectrometer.

Complexes of general formula **$[Pt(4,4'\text{-}X_2\text{-}bpy)Cl_2]$** were prepared by the following general procedure. A suspension of the appropriate ligand (1 equivalent) was heated

under reflux with stirring in an aqueous solution of $K_2[PtCl_4]$ (1 equivalent). The resultant precipitate was filtered, washed with H_2O, dried *in vacuo* and recrystallised from a saturated hot DMF solution. $[Pt(4,4'\text{-}(NH_2)_2\text{-bpy})Cl_2]$ decomposed on attempted recrystallisation and was used without further purifiction. Reflux times, percentage yields and analyses are given in table 2.1. Red $[Pt(4,4'\text{-}(NO_2)_2\text{-bpy})Cl_2]$ readily absorbs moisture from air turning to a dark green/black colour. The moisture uptake may be reversed by drying *in vacuo* at 313K for a few hours.

Table 2.1 Synthesis conditions and analyses of $[Pt(4,4'\text{-}X_2\text{-bpy})Cl_2]$

X	t/minutes[a]	yield/%	colour	C	H	N
NH_2	15	80	yellow	25.22[b]	2.73	11.46
				(26.56[c]	2.23	12.39)
OEt	75	100	yellow	32.60	3.28	5.67
				(32.95	3.17	5.49)
Ph	120	60	yellow	46.45	2.96	5.42
				(46.00	2.81	4.88)
Cl	240	85	yellow	27.23	1.79	7.45
				(24.46	1.23	5.71)
CO_2Me	240	79	yellow	31.18	2.33	5.14
				(31.24	2.25	5.21)
NO_2	300	84	red[d]	-	-	-

(a) reflux time, (b) experimental, (c) predicted, (d) anhydrous

$[Pd(4,4'\text{-}X_2\text{-bpy})Cl_2]$ ($X=CO_2Me$, NO_2) were made by analogous routes to the Pt complexes. Heating the suspensions under reflux for 3 hours gave solids which on recrystallisation twice from hot DMF yield yellow needles of the desired product (93%, $X=CO_2Me$; 76%, $X=NO_2$). C:H:N $X=CO_2Me$: 37.50%:2.75%:6.27% (predicted

37.40%:2.70%:6.23%); X=NO_2: 27.46%:1.12%:11.63% (predicted 28.36%:1.43%:13.23%).

[Rh(4,4'-$(NO_2)_2$-bpy)(cod)]ClO_4 (cod=1,5-cyclooctadiene) was prepared by an analogous route to [Rh(bpy)(cod)]ClO_4.[34] An excess of 4,4'-$(NO_2)_2$-bpy (200 mg, 8.13×10^{-4} mol) was stirred with a suspension of $[Rh(cod)Cl]_2$ [35] (2.94×10^{-4} mol) in MeOH (10 ml) for 1 hour. The mixture was filtered and $NaClO_4$ (150 mg) in H_2O (10 ml) added to the green filtrate to yield a dark microcrystalline solid which was separated by filtration, washed with H_2O then Et_2O and air dried (66%). The product was further purified by passage through a sephadex column with CH_2Cl_2/MeCN eluent (1:1 v/v). C:H:N 37.41%:3.22%:9.66% (predicted 38.83%:3.27%:10.07%).

2.2 *X*-ray Crystallography

A red block of **[Pt(4,4'-$(NO_2)_2$-bpy)Cl_2]** was grown by slow cooling of a saturated MeCN solution.

Crystal Data: $C_{10}H_6Cl_2N_4O_4Pt$, M_r = 512.19, a = 5.4788(17) Å, b= 19.253(4) Å, c = 30.115(5) Å, V = 3176.6 $Å^3$, from the setting angles of 25 centered reflections, $9.5<\theta<10.5°$, Mo-K_α *X*-radiation, λ = 0.761073 Å, orthorhombic, space group $Pc2_1n$ (non-standard setting of $Pna2_1$, no. 33), Z = 8 (two independent molecules), D_x = 2.142 gcm^{-3}, μ(Mo-K_α) = 92.8 cm^{-1}, $F(000)$ = 1904. Intensity data (+h, +k, +l) were collected to $\theta_{max}=25°$, T = 291 K, over 69 *X*-ray hours on an Enraf-Nonius CAD4 diffractometer. Of 3286 reflections measured (including 396 systematically absent) 2130 [$F \geq 2.0\sigma(F)$] were retained for solution and refinement.

Space group confirmed by ultimately successful refinement. Atomic scattering factors from *International Tables* and SHELX76.[36,37] Structure solution and refinement *via* SHELX76. Other programs used include CALC and SHELXTL/PC.[38,39] Pt atoms

located by analysis of the Patterson function, and all other atoms (except H) by iterative full-matrix least-squares and ΔF syntheses. Ghost atoms (Pt(A2) and Pt(B2)) visible at *ca.* 1 Å from the Pt atoms, almost normal to the co-ordination plane. Further refinement included tied occupancies, converging at 0.844(5) and 0.156(5) for main and ghost atoms respectively. Only disordered Pt atoms located. Following an empirical absorption correction[40] (maximum and minimum corrections 1.111 and 0.841 respectively) and inclusion of the weighting scheme $w^{-1} = [\sigma^2(F)+0.002211F^2]$, full-matrix least-squares refinement (main Pt and Cl atoms anisotropic; ghost Pt and all other atoms isotropic, H atoms in idealised positions (C-H 1.08 Å: U_H = 0.06 Å^2)) converged to R = 0.0830, wR = 0.1091 and S = 1.046 for 213 variables and 2130 observed reflections. Several atoms of the bipyridyl ligand were unstable under non-constrained refinement. For this reason constraints were applied to the lengths of similar bonds between the two independent molecules. Specifically, the two C-C (bridge) distances were constrained to within 0.05 Å, as were the eight C-N (ring) distances, the sixteen C-C (ring) distances, the four C-NO_2 distances and the eight N-O distances. Final fractional co-ordinates are listed in appendix A and derived molecular parameters in chapter 5.

Even with the refinement constraints some bond distances and angles clearly appear distorted. We suspect this arises, at least in part, from the fact that the array of heavy atoms in this non-centrosymmetric lattice is pseudo centrosymmetric, giving rise to unstable refinement. In this context it could be instructive to repeat the experiment with the Pd analogue (if isomorphous) where this effect could be less. Nevertheless, in the present case the molecular stereochemistry is unequivocally established, and some interesting packing features are evident, as discussed in appendix A.

2.3 Extended Hückel Molecular Orbital (EHMO) Calculations

EHMO calculations used a locally modified version of ICON8 and the weighted H_{ij} formula,[41,42] and were performed on models of $[Pt(bpy)Cl_2]$, $[Pt(bpy)(NH_3)_2]^{2+}$,

$[Pt(bpy)(CN)_2]$ and $[Pt(4,4'-(NO_2)_2-bpy)Cl_2]$ based on crystallographic data.[43-45] The same Pt(bpy) fragment was used in each case with C-C and C-N bond lengths of 1.37 Å, Pt-N of 1.99 Å and a N-Pt-N bite angle of 80°. Other bond lengths used were: Pt-Cl 2.31 Å, N-O 1.20 Å. The molecule lies in the xy plane with the y-axis bisecting the N-Pt-N angle. The H_{ii}'s for Pt orbitals were initially optimised by charge iteration calculations (H_{ii}=-VSIE(Q), where VSIE(Q)=valence state ionisation energy of orbital i when atom has charge Q). The full list of orbital exponents and H_{ii}'s (eV) used is: H_{1s}: H_{ii}=-13.60, ζ=1.30; C_{2s}: H_{ii}=-21.40, ζ=1.625, C_{2p}: H_{ii}=-11.40, ζ=1.625; N_{2s}: H_{ii}=-26.00, ζ=1.95, N_{2p}: H_{ii}=-13.40, ζ=1.95; O_{2s}: H_{ii}=-32.30, ζ=2.275, O_{2p}: H_{ii}=-14.80, ζ=2.275; Cl_{3s}: H_{ii}=-30.00, ζ=2.033, Cl_{3p}: H_{ii}=-15.00, ζ=2.033; Pt_{6s}: H_{ii}=-10.93, ζ=2.554, Pt_{6p}: H_{ii}=-5.439, ζ=2.554, Pt_{5d}: H_{ii}=-13.52, ζ^1=6.013, ζ^2=2.696, c^1=0.63338, c^2=0.55128, where c^1 and c^2 are coefficients in the double-ζ expansion.

2.4 Electrochemistry and Spectroelectrochemistry

Electrochemical studies were performed using a DSL 286-D PC with General Purpose Electrochemical System (GPES) Version 3 software connected to an Autolab system containing a PSTAT10 potentiostat and data were plotted using Origin Version 3.1 software.

Cyclic voltammetry used a standard three electrode configuration with Pt microworking and counter electrodes and a Ag/AgCl reference electrode against which the ferrocene/ferrocinium couple was measured at +0.55 V. Redox potentials and peak-to-peak values are reported for a scan rate of $100mVs^{-1}$. Bulk electrolysis was performed at 243 K in a compartmentalised H-cell with Pt grid working and counter electrodes, the reference electrode was as before. All electrochemical studies were performed on $N_{2(g)}$ purged DMF, MeCN or CH_2Cl_2 solutions. Inert electrolyte, $TBABF_4$ (TBA=tetrabutylammonium), was used in 0.5 M concentration in CH_2Cl_2 and 0.1 M concentration in MeCN and DMF.

In situ uv/vis/nir electrogenerations employed the optically transparent electrode cell (OTE, figure 2.1).[46] A Pt/Rh gauze working electrode (transparency ~40%) is housed in a quartz cell such that the spectrometer beam passes through the grid. An extension is fitted to the quartz cell to act as a reservoir. The Pt wire counter and Ag/AgCl reference electrodes are isolated from the working electrode by sintered frits. The temperature of the cell is controlled by passing prechilled $N_{2(g)}$ over the cell. Unless otherwise stated in the text reductions were performed at 243 K as a function of potential with spectra recorded every 15 minutes. After each experiment the electrogeneration potential was set at 0 V to regenerate the starting material in order to ensure the chemical integrity of the system. Uv/vis/nir spectra were recorded on a Perkin-Elmer λ9 spectrophotometer.

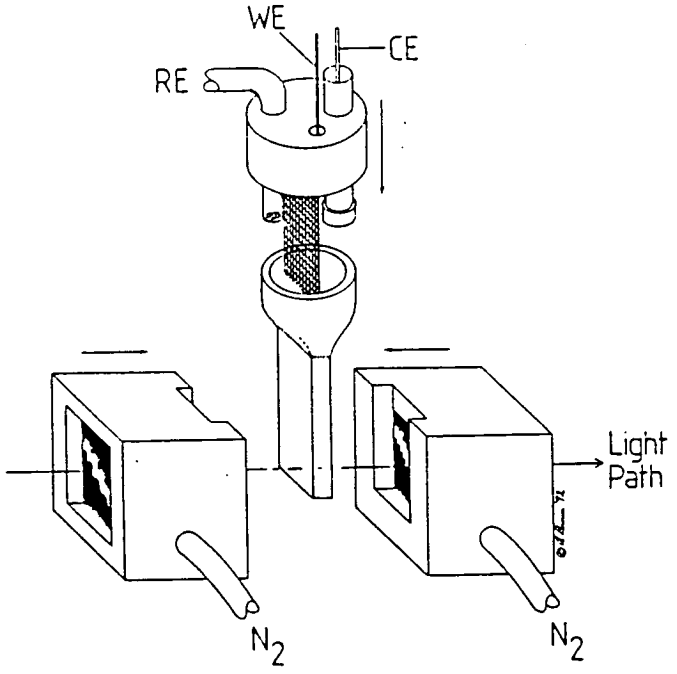

Figure 2.1 Schematic representation of OTE cell

X-band epr spectra were recorded on a Bruker ER200D-SCR spectrometer. Fluid solution spectra used a flat cell. Q-band spectra were recorded on a Varian E112 spectrometer at 150 K (University of Manchester). Samples for epr study were prepared by either bulk electrolysis at 243 K or chemical reduction with an appropriate reducing agent under Schlenk conditions and transfered to an epr sample tube under $N_{2(g)}$. Anisotropic epr spectra were computer simulated using a University of Manchester programme.[47] Isotropic epr spectra were simulated using a local programme.[48]

Chapter 3. (2,2'-bipyridine)bis(L)platinum(II), [Pt(bpy)L_2]

3.1 Introduction

Since their initial synthesis by Morgan and Burstall[28] platinum bipyridyl complexes have been of great interest due to their interesting structural,[43-45,49,50] absorption and emission spectral[51-57] and electrochemical properties.[58-61]

[Pt(bpy)Cl_2] exhibits dimorphism in the solid state having yellow and red forms. Crystal structure determinations reveal both structures to consist of stacks of monomeric units. The red form has a "staggered" arrangement of molecules in adjacent layers, *i.*e. there is pseudo two fold symmetry down the stack, with the Pt-Pt vector perpendicular to the layer stacking.[44] A Pt-Pt distance of 3.45 Å is measured for the red form. The essentially monomeric yellow form shows a rotated orientation between adjacent molecules (*ca.* 120°) and a layer stacking which is no longer perpendicular to the Pt-Pt vector, leading to a larger Pt-Pt distance of 4.44 Å.[43] Both forms dissolve to give yellow solutions with identical absorption spectra. Similar structural forms are observed for [Pd(bpy)Cl_2].[49,50] [Pt(bpy)$(CN)_2$] has a smaller Pt-Pt distance of 3.33 Å and this stronger intermolecular interaction may be partly responsible for this compound's poor solubility in all common solvents.[45]

The electronic structure of these compounds has been the subject of much debate. Gidney *et al.* reported the uv/vis absorption spectrum of [Pt(bpy)Cl_2], identifying the bands at 323 and 311 nm as singlet-singlet intra-ligand ($^1\pi-\pi^*$) transitions and a singlet-singlet metal-to-ligand charge transfer transition (^{1}MLCT, d-π^*) at 370 nm in MeOH solution.[51] Webb and Rossiello noted the presence of weak ($\varepsilon\approx50$ $M^{-1}cm^{-1}$) absorption bands at 440, 462 and 500 nm in MeOH solution and suggested their origin to be either ligand field (LF) or spin-forbidden triplet charge transfer.[52] They also reported a structured emission spectrum originating at *ca.* 480 nm in a MeOH glass at 77 K which they tentatively assigned as charge-transfer emission from a bpy-based orbital. Miskowski and Holding, however, failed to reproduce this result,

instead finding a broad unstructured emission at 610 nm which they assigned as a LF emission due to its lack of vibronic structure and non-solvent sensitivity, and consequently assign the weak, low-energy absorption bands as LF transitions.[53,54] Curiously they assign very similar features in the absorption spectrum of $[Pt(bpy)(en)](ClO_4)_2$ at 447 nm in aqueous solution as singlet-triplet $\pi-\pi^*$ transitions, and the emissive excited state as $^3\pi-\pi^*$ due to the vibronically structured nature of the emission spectrum (originating at 458 nm in a MeOH/EtOH glass at 77 K). Similar structured emissions have been observed for $[Pt(bpy)(NH_3)_2](PF_6)_2$, $[Pt(bpy)(CN)_2]$ and $[Pt(5,5'\text{-}Me_2\text{-}bpy)(CN)_2]$.[55-57] Thus, the lowest-unoccupied molecular orbital (LUMO) of $[Pt(bpy)L_2]$ was assigned as metal-based for $L=Cl^-$ but bpy π^*-based where L is a nitrogen- or carbon-donor. The anomalous electronic structure of $[Pt(bpy)Cl_2]$ has been attributed to the weak-field nature of the halide ligand compared to the N- or C-donors.[53]

A number of electrochemical studies have been performed to probe further the electronic structure of these complexes.[58-61] Typically two consecutive one-electron reductions are observed which various authors have tentatively assigned as bpy-based simply on the value of their reduction potentials and their electrochemical and chemical reversibility.[58,59] Braterman *et al.* have assigned the first reductions to be bpy-based and the second reductions as metal-based on the basis of uv/vis/nir and epr spectroelectrochemical experiments on $[Pt(bpy)(en)](BF_4)_2$, $[Pt(bpy)(py)_2](BF_4)_2$ and $[Pt(bpy)(Ph)_2]$. Thus they conclude the LUMO to be bpy-based with a metal-based orbital at slightly higher energy.[60,61]

In this chapter we perform a more complete spectroelectrochemical investigation of these species and a more detailed analysis of the uv/vis/nir and epr spectra of the reduction products of a series of complexes of general formula $[Pt(bpy)L_2]$ where L is changed systematically from a π-donor, weak-field ligand ($L=Cl^-$) to a π-acceptor, strong-field ligand ($L=CN^-$). We present strong evidence that the LUMO of $[Pt(bpy)Cl_2]$ is in fact ligand-based in common with all complexes $[Pt(bpy)L_2]$, and

that the two reductive processes seen in the cyclic voltammograms of these species are both centered on the bpy ligand. In marked contrast we show that the LUMO of $[Pd(bpy)Cl_2]$ is metal-based, *i.e.* the vacant metal 4d-orbital on the Pd centre is lower in energy than the first π^* orbital on the bpy ligand.

3.2 EHMO Calculations

EHMO calculations were performed on idealised models of $[Pt(bpy)Cl_2]$, $[Pt(bpy)(NH_3)_2]^{2+}$ and $[Pt(bpy)(CN)_2]$. The models are detailed in chapter 2. In each case the molecule lies in the xy plane with the y axis bisecting the N-Pt-N angle.

The LUMO of $[Pt(bpy)Cl_2]$ is computed to be of b_2 symmetry with 96% bpy π^* character (the lowest energy bpy π^* orbital, $\pi(7)$) and small Pt $5d_{yz}$ and $6p_z$ admixtures of 2.0% and 1.7% respectively. These results are in general agreement with those of Eisenberg *et al.* on complexes such as [Pt(bpy)(mnt)].[62] The major contributions to the bpy-based π^* LUMO are from the two nitrogen nuclei and the C2, 2', 4 and 4' nuclei where the numbering scheme is the same as that for free bpy as shown in figure 1.1. Calculations performed for $[Pt(bpy)(NH_3)_2]^{2+}$ and $[Pt(bpy)(CN)_2]$ give similar molecular orbital schemes as for $[Pt(bpy)Cl_2]$. Nuclear coefficients for the LUMOs $[Pt(bpy)Cl_2]$, $[Pt(bpy)(NH_3)_2]^{2+}$ and $[Pt(bpy)(CN)_2]$ are given in table 3.1. The results show the $5d_{yz}$ admixture to the primarily ligand-based orbital to decrease as L is changed from Cl^- to CN^-. Interestingly the calculations show the $6p_z$ contributions to the LUMO to increase down the series. In no cases were there any significant contributions from orbitals based on the L ligands.

The calculations indicate that the two highest occupied molecular orbitals are very close in energy for $[Pt(bpy)Cl_2]$, $[Pt(bpy)(NH_3)_2]^{2+}$ and $[Pt(bpy)(CN)_2]$. One is predominantly the Pt $d_{x^2-y^2}$ orbital and the other is the highest energy bpy-based π orbital ($\pi(6)$). This supports the assignment of the uv/vis spectra with internal π–π^* bands ($\pi(6\text{-}7)$) and an MLCT (d-$\pi(7)$) at similar energies.

Table 3.1 Nuclear coefficients to LUMO of $[Pt(bpy)L_2]$

Atom	Orbital	$[Pt(bpy)Cl_2]$	$[Pt(bpy)(NH_3)_2]^{2+}$	$[Pt(bpy)(CN)_2]$
N1,1'	$2p_z$	0.129	0.128	0.107
C2,2'	$2p_z$	0.130	0.131	0.120
C3,3'	$2p_z$	0.003	0.003	0.032
C4,4'	$2p_z$	0.117	0.118	0.109
C5,5'	$2p_z$	0.046	0.046	0.040
C6,6'	$2p_z$	0.055	0.055	0.055
Pt	$5d_{yz}$	0.020	0.020	0.012
	$6p_z$	0.017	0.018	0.042
C7,7'[a]	$2p_z$	-	-	0.024
N3,3'[a]	$2p_z$	-	-	0.015

(a) complex **VI** only, L=CN where C=C7,7' ; N=N3,3'

3.3 Redox Chemistry

Cyclic voltammetric studies of $[Pt(bpy)Cl_2]$ **(I)**, $[Pt(bpy)(NH_3)_2]^{2+}$ **(II)**, $[Pt(bpy)(en)]^{2+}$ **(III)**, $[Pt(bpy)(py)_2]^{2+}$ **(IV)**, $[Pt(bpy)(PMe_3)_2]^{2+}$ **(V)** and $[Pt(bpy)(CN)_2]$ **(VI)** in 0.1 M $TBABF_4$/DMF solution reveal a fully reversible one-electron (by coulometry at 243 K) reduction at *ca.* -1 V *vs.* Ag/AgCl (table 3.2, figure 3.1). There are no oxidation processes observed prior to the solvent breakdown at +2 V for any of the compounds studied. Complexes **I-IV** and **VI** undergo a second reversible or quasi-reversible reduction at more negative potentials. The separation of reductions of 500-700 mV is typical of succesive reductions of bipyridyls, *i.e.* spin pairing of the two added electrons in the same molecular orbital. The second reduction of **V** is irreversible.

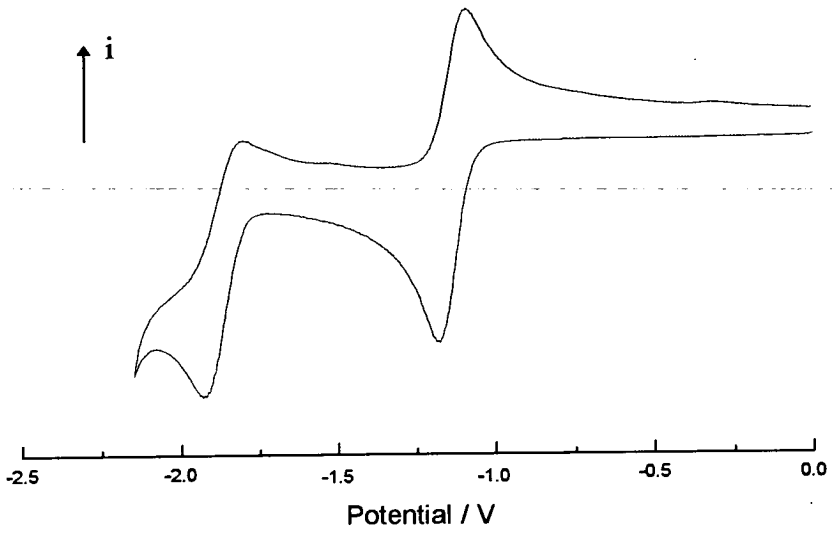

Figure 3.1 Cyclic voltammogram of $[Pt(bpy)Cl_2]$ in 0.1 M $TBABF_4$/DMF at 293 K

Table 3.2 Redox potentials of $[Pt(bpy)L_2]$ in 0.1 M $TBABF_4$/DMF solution at 293 K

Complex	E_1/ V	E_2/ V
I	-1.06[a](0.070)[b]	-1.79(0.110)
II	-0.99(0.060)	-1.65(0.080)
III	-0.90(0.070)	-1.56(0.070)
IV	-0.91(0.060)	-1.45(0.070)
V	-0.94(0.060)	-1.48[c]
VI	-0.94(0.060)	-1.61(0.090)

(a) $(E_f+E_r)/2$, (b) (E_f-E_r), (c) anodic peak not observed, cathodic peak quoted

3.4 Uv/Vis/Nir Spectroelectrochemistry

The electronic spectra of **I-VI** in DMF solution are dominated by the intense intraligand $\pi-\pi^*$ bands of bpy and a lower energy metal-to-ligand charge transfer (d-bpy π^*, MLCT) transition, which appears as a shoulder for **II-VI** but is clearly

resolved for **I** (table 3.3). Extinction coefficients for $[Pt(bpy)(CN)_2]$ are not quoted in table 3.3 because of the extreme solubility problems associated with this complex.

Table 3.3 Uv/vis spectra of **I-VI** in DMF solution at 293 K

Complex	MLCT/ kcm^{-1}	$\pi-\pi^*$/ kcm^{-1}	
I	25.7(0.45)[a]	30.8(1.28)	32.0(1.19)
II	29.4(0.33)[b]	31.1(1.67)	32.3(1.35)
III	29.4(0.41)[b]	31.2(2.25)	32.4(1.86)
IV	29.8(0.41)[b]	31.1(1.70)	32.4(1.43)
V	27.4(0.12)[b]	30.9(1.24)	31.8(1.05)
VI	29.4[b]	31.3	32.6[b]

(a) ε / $10^4 M^{-1}cm^{-1}$, (b) shoulder

The spectral changes of **I** on reduction to **I**$^-$ in 0.1M $TBABF_4$/DMF solution at 243 K involve the collapse of bands associated with coordinated neutral bpy and the growth of bands associated with coordinated radical anion bpy$^-$ (figure 3.2 and figure 1.4).[15,16] Thus, the new bands at 11.2, 20.1, 21.6 and 27.9 kcm^{-1} are all intraligand transitions of coordinated bpy$^-$. The band at 23.9 kcm^{-1} has not been assigned to an internal bpy$^-$ transition. Braterman *et al.* tentatively assigned this to a ligand-to-metal charge transfer transition for $[Pt(bpy)(Ph)_2]^-$.[60,61] However, assignment as an MLCT band would be consistent with the expected red-shift of this transition on semi-occupancy of the π^* orbital.

Complexes **II-VI** exhibit similar spectra on reduction and may be assigned as above. Typical spectra of the reduced complexes are shown in figure 3.3 and assignments of the electronic transitions are given in table 3.4. In the assignments given in table 3.4 the $\pi(7)$ orbital is the lowest unoccupied bpy-based π^* orbital of the parent complexes, and is the orbital occupied on reduction. Extinction coefficient values are quoted in table 3.4 but yield little useful information and are not discussed further. The reduced species were found to be unstable at ambient temperatures as witnessed

by the absorption spectrum failing to return to that of the parent species on reoxidation of the solution. However the reduced species were all indefinitely stable at 243 K.

Thus, the uv/vis/nir spectra of **I**-**VI** suggest that these species should be formulated as $[Pt^{II}(bpy^{-})L_2]^{-}$.

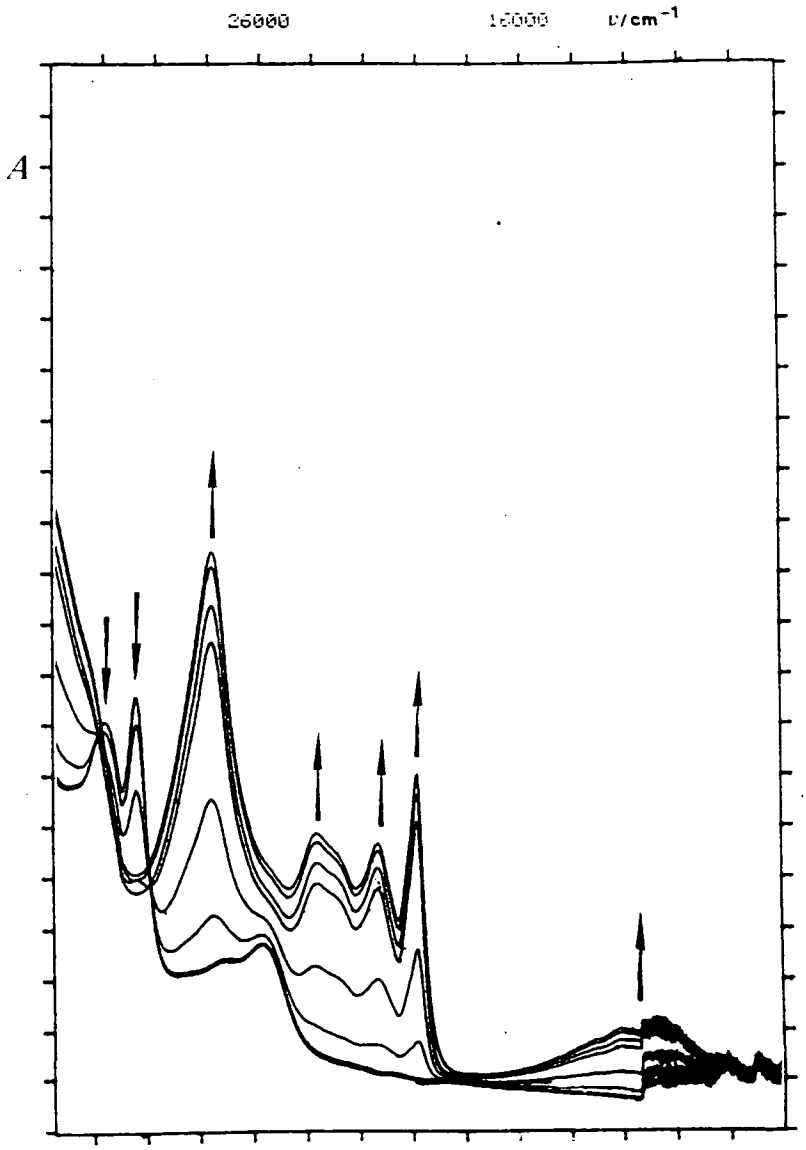

Figure 3.2 OTE reduction of $\mathbf{I}^{0/-}$ in 0.1 M $TBABF_4$/DMF solution at 243 K

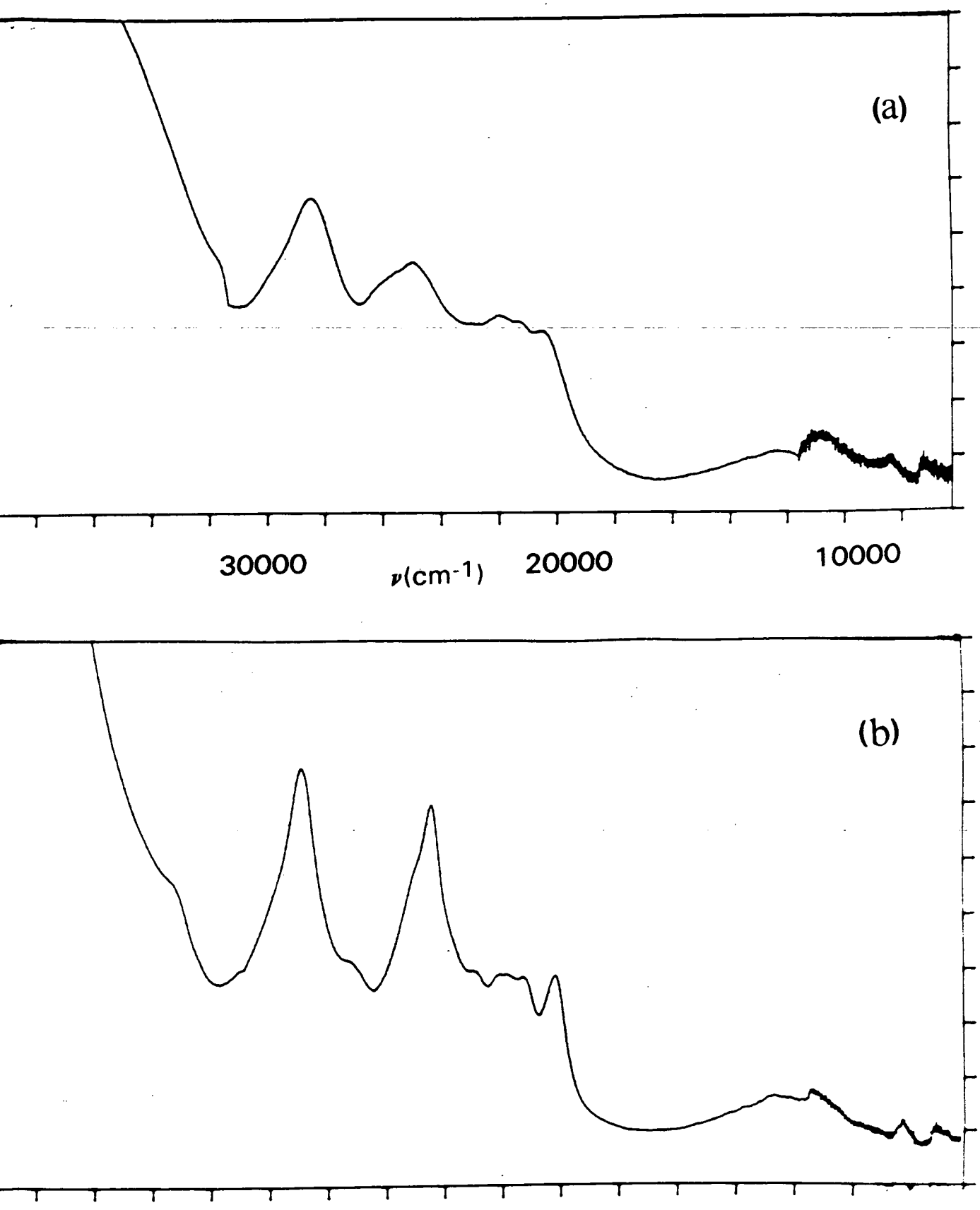

Figure 3.3 Uv/vis/nir spectra of $\mathbf{IV}^-$ (a) and $\mathbf{VI}^-$ (b) in 0.1 M $TBABF_4$/DMF at 243 K

Table 3.4 Uv/vis/nir spectra of $[Pt(bpy)L_2]^-$ in 0.1 M $TBABF_4$/DMF at 243 K

Complex	$\pi(7\text{-}8,9)^{*a}$	$\pi(7\text{-}10)^*$	MLCT	$\pi(6\text{-}7)^*$/ kcm^{-1}
Na(bpy)[b]	12.0(0.15)[c]	17.8(0.62), 18.8(0.62)	-	25.9(2.95)
I⁻	11.2(0.21)	20.1(1.00), 21.6(0.54)	23.9(0.81)	27.9(1.72)
II⁻	12.4(0.23)	19.7(0.54), 20.9(0.57)	24.8(0.53)	28.0(1.10)
III⁻	12.4(0.33)	20.5(0.68), 22.0(0.65)	24.8(1.14)	29.3(1.35)
IV⁻	10.7(0.24)	20.4(0.51), 22.0(0.57)	24.9(0.73)	28.4(0.92)
V⁻	11.4(0.13)	20.6(0.44), 22.1(0.41)	24.7(0.63)	28.9(0.65)
VI⁻	11.5	20.5, 22.0	24.9	29.4

(a) Transitions assigned by comparison with Na(bpy), (b)THF solution, reference 15,

(c) ε / 10^4 $M^{-1}cm^{-1}$

3.5 Epr Spectroelectrochemistry

The solution spectra of the one-electron reduction products of **I-V** in DMF solution are as expected for interaction of the unpaired electron with platinum in natural abundance (^{195}Pt, 34%, spin 1/2). A typical spectrum is shown in figure 3.4. A broad singlet resonance is observed with ^{195}Pt satellites. The isotropic hyperfine coupling constants for **I⁻-V⁻** are in the range 40 to 55x10^{-4} cm^{-1} (table 3.5). The reduction products can be generated electrochemically or chemically (with excess $NaBH_4$) to give rise to identical spectra, *i.e.* the same reduction product is generated regardless of the method of generating the sample.

The observed isotropic epr signals of **I⁻-V⁻** show that the coupling of the unpaired electron is mainly to the Pt nucleus, with any coupling to ligand nuclei unresolved and therefore much smaller in magnitude. Direct admixture of the Pt 6s orbital to the singly occupied molecular orbital (SOMO) of b_2 symmetry is forbidden in C_{2v} point symmetry and consequently the isotropic hyperfine coupling must arise *via* inner-core polarisation and is probably negative in sign.[63]

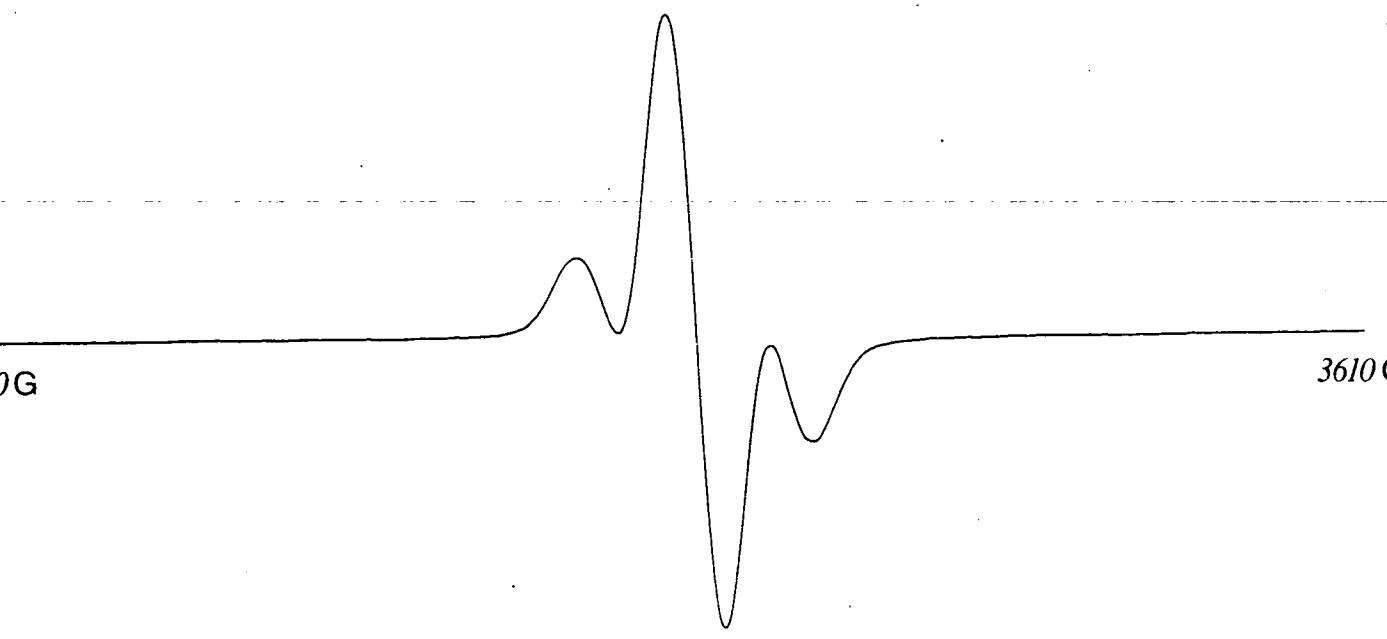

Figure 3.4 Solution epr spectrum of **III** in DMF at 293 K

For **VI** superhyperfine coupling of the unpaired electron to nuclei of the bpy ligand is observed (figure 3.5a). A good simulation of this isotropic spectrum is possible assuming coupling of the unpaired electron to ^{195}Pt (A_{iso}=20.5 G (19.1x10^{-4} cm^{-1})), to two equivalent ^{14}N nuclei ($a_{iso}(^{14}N)$=3.4 G (3.2x10^{-4} cm^{-1})), to two sets of two equivalent ^{1}H nuclei ($a_{iso(1)}$=2.8 G (2.6x10^{-4} cm^{-1}) and $a_{iso(2)}$=2.2 G (2.1x10^{-4} cm^{-1})) with a Lorentzian linewidth of 1.7 G (figure 3.5b). We assign the larger ^{1}H coupling to H4 and H4', and the ^{14}N coupling to the ring nitrogens of the bpy ligand in agreement with the EHMO calculations (see section 3.2). The smaller ^{1}H coupling

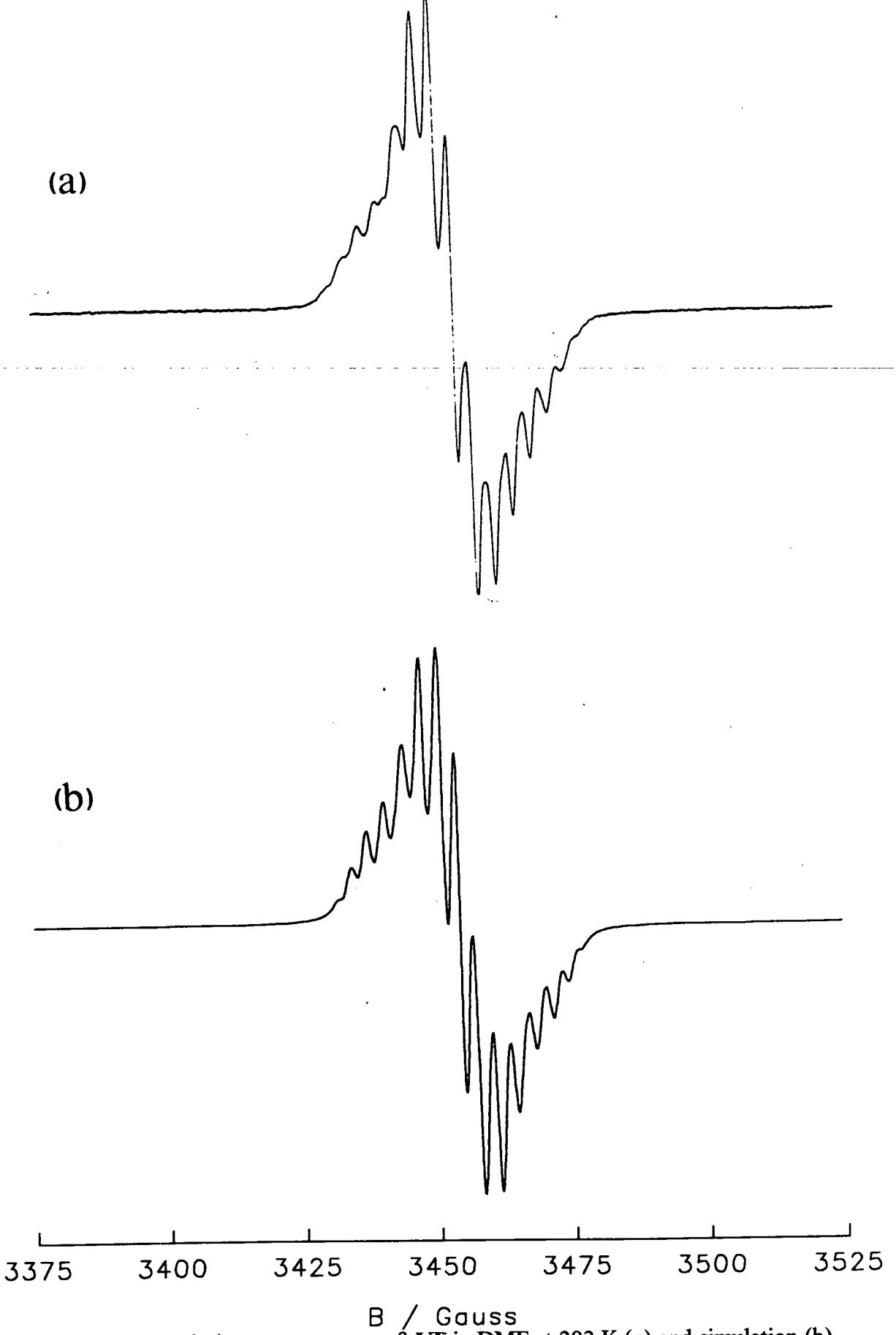

Figure 3.5 Solution epr spectrum of **VI** in DMF at 293 K (a) and simulation (b)

has not been assigned as the calculations do not favour another pair of ^{1}H nuclei. EHMO calculations show that the nitrogen atoms of the cyanides should make little contribution to the SOMO. Brown *et al.* assigned the largest ^{1}H couplings in the isotropic epr spectra of species such as mer-$[Mn^{I}(CO)(CNBu^{t})_3(bpy^{-})]$ similarly.[64] The coupling to ^{195}Pt is considerably smaller in **VI**$^{-}$ than for **I**$^{-}$ to **V**$^{-}$, hence we suggest that this allows the resolution of the superhyperfine structure in the epr spectrum of $[Pt(bpy)(CN)_2]^{-}$.

Table 3.5 Epr parameters for $[Pt(bpy)L_2]^{-}$

		g_{iso}[a]	g_1[b]	g_2	g_3	$A_{iso}(Pt)$[c]	A_1	A_2	A_3
I^{-}	exp[d]	1.998	2.038	2.009	1.935	-54	-56	-95	-
	sim[e]	-	2.038	2.011	1.938	-	-57.4	-80.6	-20.8
II^{-}	exp[d]	1.998	2.029	2.003	1.936	-40	-59	-91	-
	sim[e]	-	2.027	2.002	1.936	-	-58.2	-71.2	-31.6
III^{-}	exp[d]	1.998	2.026	2.009	1.954	-42	-53	-78	-
IV^{-}	exp[d]	1.994	2.017	2.004	1.960	-40	-60	-75	-
	sim[e]	-	2.018	2.004	1.960	-	-56.5	-65.5	-27.5
V^{-}	exp[d]	1.999	2.022	2.016	1.970	-	-56	-65	-
VI^{-}	exp[d,f]	1.994	2.013	2.009	1.974	-	-38	-49	-
	sim[e,f]	1.994[g]	2.014	2.009	1.974	-19.1[g]	-35.7	-38.5	+27.6

(a) isotropic data from chemically generated species, DMF solution, (b) anisotropic data from electrochemically generated species, 0.1M $TBABF_4$/DMF, (c) A / 10^{-4} cm^{-1}, (d) parameters estimated directly from the spectra, (e) parameters from computer simulations, (f) Q-band spectrum, (g) from simulations as described in the text.

On freezing the solutions at 77 K, X-band epr spectra exhibit rhombic g and Pt hyperfine tensors (for example, figures 3.6 and 3.7). The high field component of each of these spectra (g_3) does not show any resolution of the ^{195}Pt coupling and the values of A_3 in table 3.5 are those required to give the best fit between experimental

and simulated spectra. Experiments with mixed solvent systems also failed to give resolution of this g_3 component. Excellent simulations of the X-band spectra of $\mathbf{I}^-$, $\mathbf{II}^-$ and $\mathbf{IV}^-$ were obtained using the parameters in table 3.5. The magnitude of A_3 has an uncertainty of *ca.* $\pm 5 \times 10^{-4}$ cm^{-1}. For $\mathbf{I}^-$ to $\mathbf{IV}^-$ the averaged values of g and A used in the simulations are in good agreement with the experimental isotropic values and hence A_1, A_2 and A_3 all have the same sign as each other and as A_{iso}. The frozen solution spectra of $\mathbf{V}^-$ and $\mathbf{VI}^-$ appear to be axial at X-band frequency but their rhombicity is clearly shown in the Q-band spectrum of $\mathbf{VI}^-$ (figures 3.8 and 3.9). The X-band spectrum of $\mathbf{VI}^-$ shows no change between 77 K and 150 K, *i.e.* the X- and Q-band spectra are of the same species. For $\mathbf{VI}^-$ a good simulation of the Q-band spectrum is possible using the parameters in table 3.5 (figure 3.9c). In order that the averaged values of A_1, A_2 and A_3 are compatible with the observed A_{iso}, it is necessary to have A_3 opposite in sign to A_1, A_2 and A_{iso}. The physical ramifications of this change in sign of A_3 are, as yet, unclear. No superhyperfine splittings have been resolved in any of the frozen solution spectra, presumably because of the greater linewidths of the frozen solution spectra compared to the solution spectra.

It is interesting to note that the Q-band spectrum of $\mathbf{VI}^-$ at 150 K is best simulated with a Gaussian lineshape while the solution spectrum of $\mathbf{VI}^-$ at 293 K is best simulated with a Lorentzian lineshape. We suggest that this is due to the unresolved superhyperfine coupling to ligand nuclei in the 150 K spectrum.

The small shift of g_{iso} from the free-electron value, g_e of 2.0023 is suggestive of only a small admixture of metal orbitals in the SOMO, and that the reduction electron is therefore mainly localised on the bpy ligand. A quantitative estimate of the Pt d orbital admixture to the SOMO of $[Pt(bpy)L_2]^-$ can be calculated using Maki's equations[3] (but Rieger's nomenclature[65]) for a $5d_{yz}$ ground state in C_{2v} symmetry (equation 1).

$$A_x - \langle A \rangle = P_d[-4/7a^2 + 2/3\Delta g_x - 5/42(\Delta g_y + \Delta g_z)] \qquad (1)$$

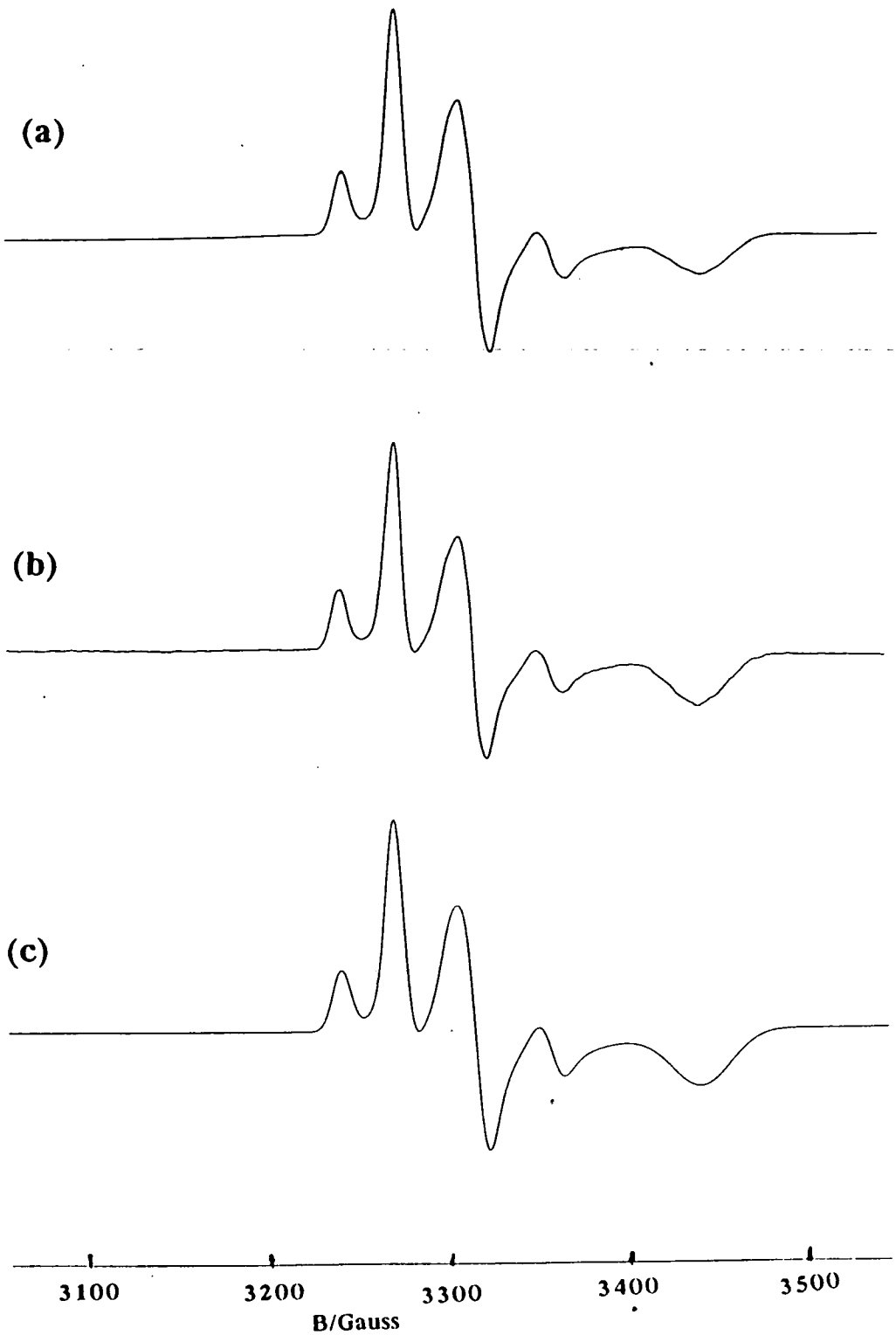

Figure 3.6 77 K X-band epr spectra of Γ electrochemically generated in 0.1 M $TBABF_4$/DMF (a), chemically generated by $NaBH_4$ (b) and simulation using the parameters in table 3.5 with Gaussian half linewidths of 10 G, 12 G and 30 G for g_1, g_2 and g_3 respectively (c)

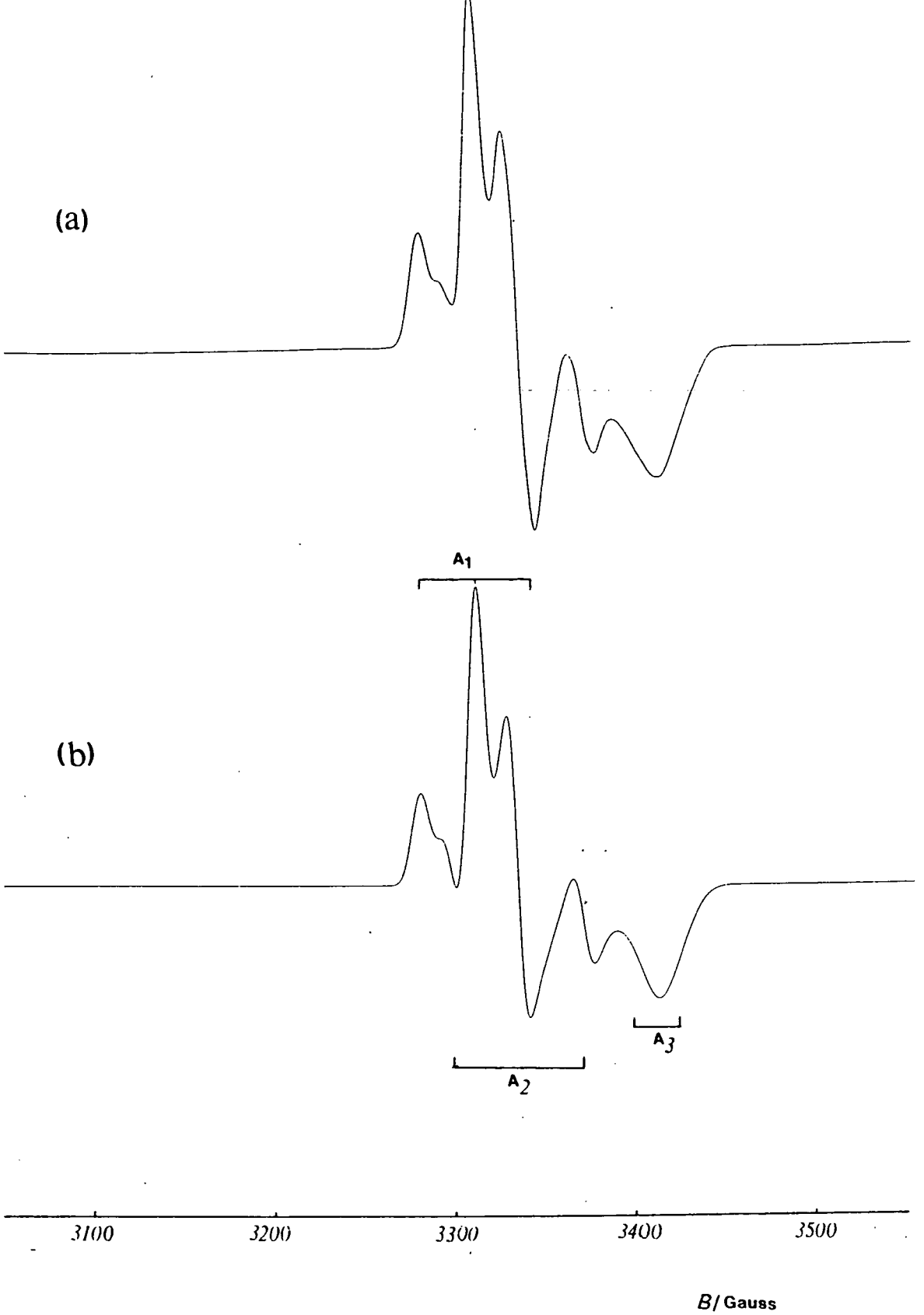

Figure 3.7 77 K X-band epr spectrum of $\mathbf{IV}^-$ in 0.1 M $TBABF_4$/DMF (a) and simulation using the parameters in table 3.5 and Gaussian half linewidths of 9 G, 10 G and 18 G for g_1, g_2 and g_3 respectively (b)

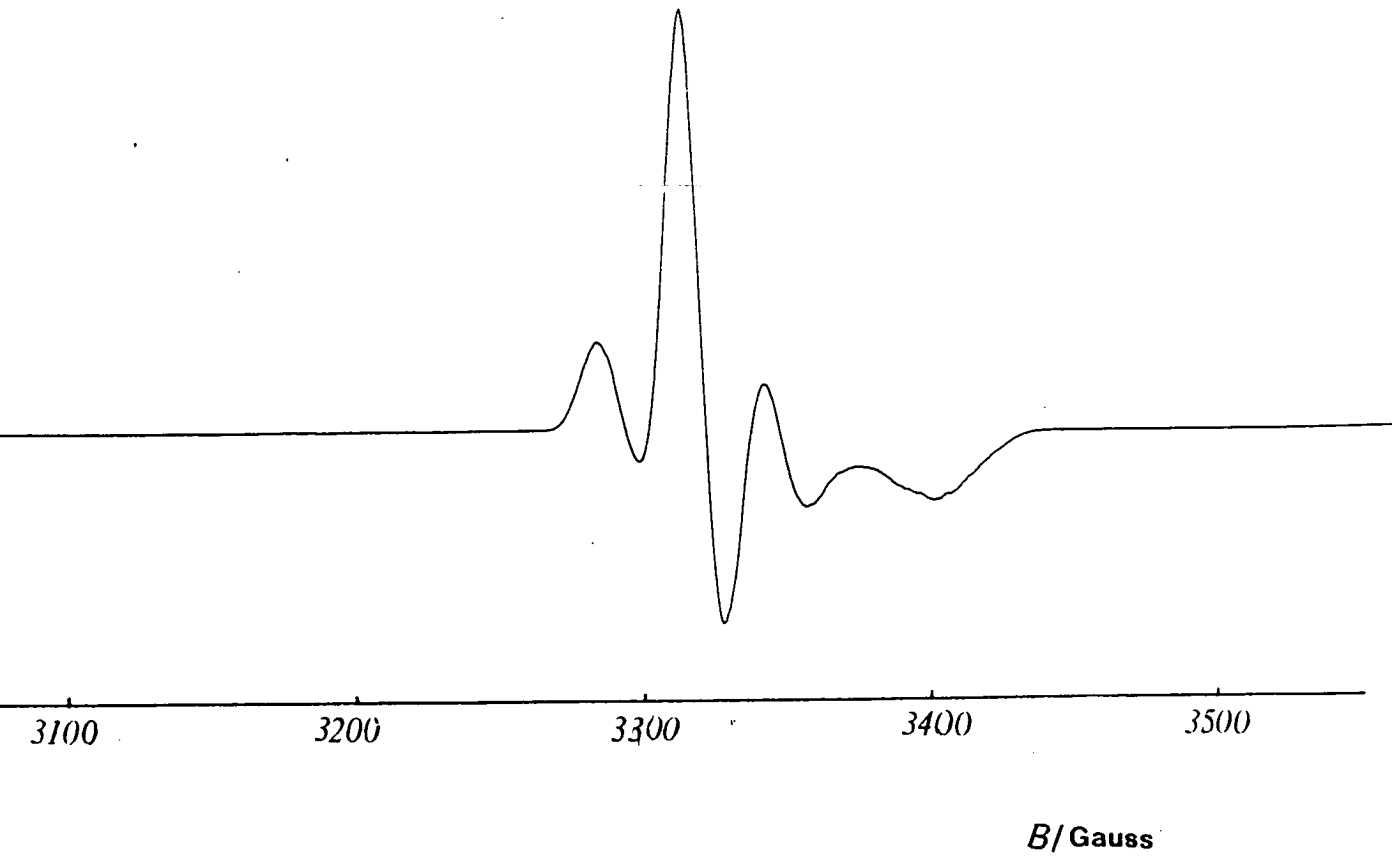

Figure 3.8 77 K X-band epr spectrum of V^- in 0.1 M $TBABF_4$/DMF

Where $\langle A \rangle = (A_1 + A_2 + A_3)/3$

$\Delta g_i = g_i - g_e$

P_d = the electron-nuclear dipolar coupling parameter for 5d electrons

$= +492 \times 10^{-4}\ cm^{-1}$ for ^{195}Pt[66]

a = the linear combination of atomic orbitals coefficient of the $5d_{yz}$ orbital in the SOMO. *i.e.* a^2 = metal $5d_{yz}$ admixture to the SOMO.

We have assigned our anisotropic spectra to g_1, g_2, g_3, A_1, A_2 and A_3 as given in table 3.5. It is now necessary to assign these to the molecular axes x, y and z. Assigning g_3 and A_3 to g_x and A_x yields meaningless values of a^2 on substituting the parameters into equation 1. Taking g_1 and g_2 as g_x gives a^2 values of 0.068 and 0.12 respectively for **I** (table 3.6). Rieger has argued that A_x should be the largest hyperfine term for $[(\eta^5\text{-}C_5Ph_5)M(CO)_2]^-$ (M=Co, Rh), which has a $5d_{yz}$ ground state in C_{2v} symmetry.[65] We therefore assign A_2 to A_x. In C_{2v} symmetry the g and metal hyperfine axes must be coincident and therefore we assign g_2 to g_x. Meaningless values of a^2 are obtained if the hyperfine coupling constants are assigned as positive. Thus, there is a maximum Pt $5d_{yz}$ admixture in the SOMO of **I** of 12%, *i.e.* the orbital is not primarily metal based. There are small but observable changes in a^2 as L is changed.

Our EHMO calculations show the Pt $6p_z$ contribution to the LUMO of $[Pt(bpy)L_2]$ to be comparable with the $5d_{yz}$. However, there is no comprehensive treatment for 6p orbital contributions to anisotropic spectra and therefore the the epr spectral results cannot be used to describe the full amount of Pt orbital contributions to the SOMO.

Table 3.6 Pt $5d_{yz}$ orbital admixtures to the SOMO of $[Pt(bpy)L_2]^-$

Complex	$g_x=g_1$	$g_x=g_2$	$g_x=g_3$
I$^-$	0.068[a]	0.12	-
II$^-$	0.057	0.074	-
IV$^-$	0.051	0.064	-
VI$^-$	0.090	0.093	-

(a) a^2 calculated from equation 1 using parameters in table 3.5

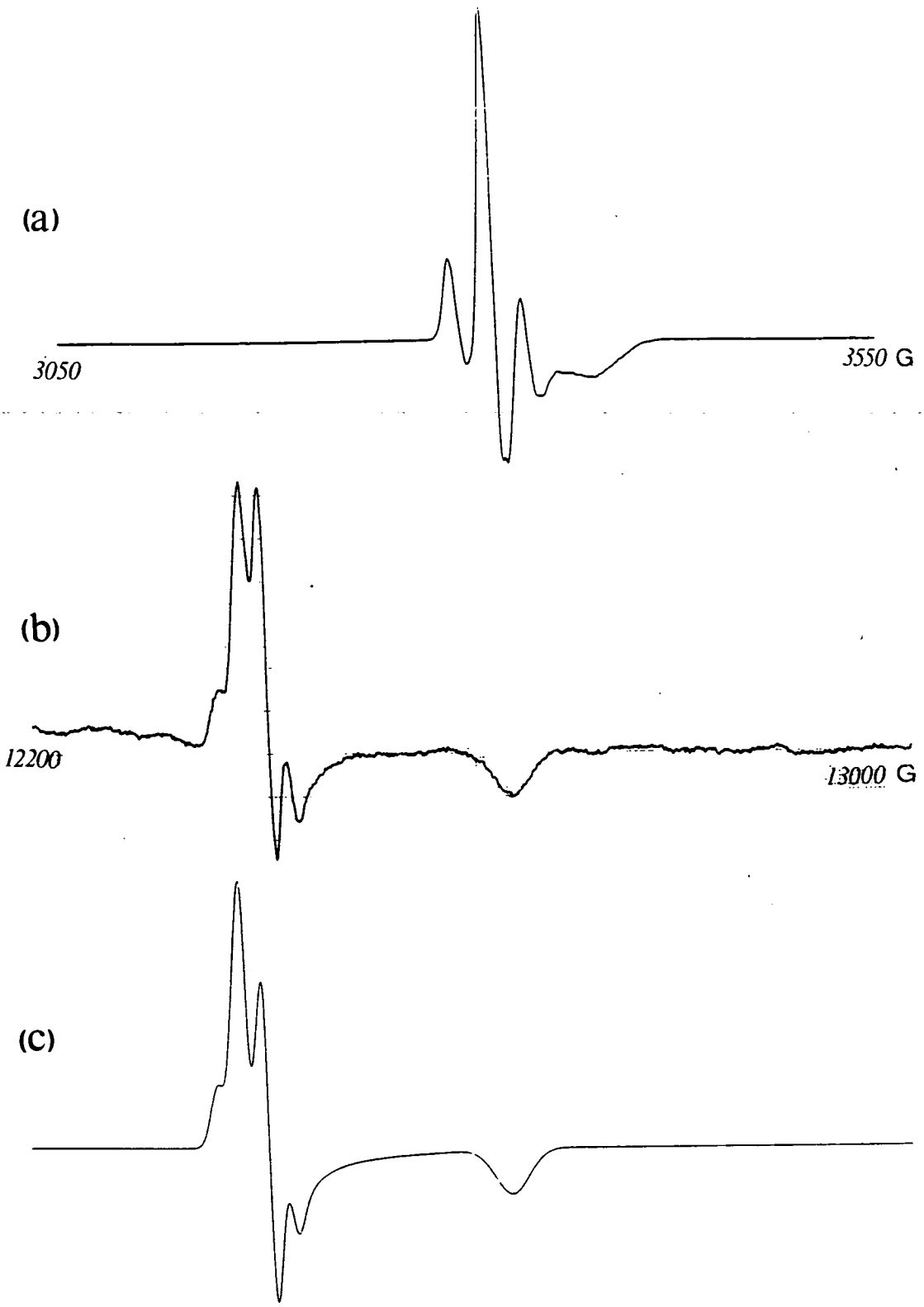

Figure 3.9 77 K X-band epr spectrum of **VI** in 0.1 M $TBABF_4$/DMF (a), 150 K Q-band epr spectrum in DMF (b) and simulation using the parameters in table 3.5 with Gaussian half linewidths of 12 G, 11 G and 26 G for g_1, g_2 and g_3 respectively (c)

3.6 Redox Chemistry of $[Pd(bpy)Cl_2]$

Cyclic voltammetry of $[Pd(bpy)Cl_2]$ in 0.1M $TBABF_4$/DMF solution reveals an irreversible reduction at -0.82 V *vs.* Ag/AgCl (figure 3.10). Bulk electrolysis shows this to be a two-electron process and results in the deposition of a black deposit (Pd metal) in the electrolysis cell. The decomposition of the complex on reduction is confirmed by a reduction process at -2.05 V in the cyclic voltammogram corresponding to the reduction of free bpy. Thus the LUMO of $[Pd(bpy)Cl_2]$ is metal-based. This is consistent with the uv/vis spectrum of $[Pd(bpy)Cl_2]$ which shows $\pi-\pi^*$ bands at 31.5 kcm^{-1} in DMF solution but no low energy MLCT band.

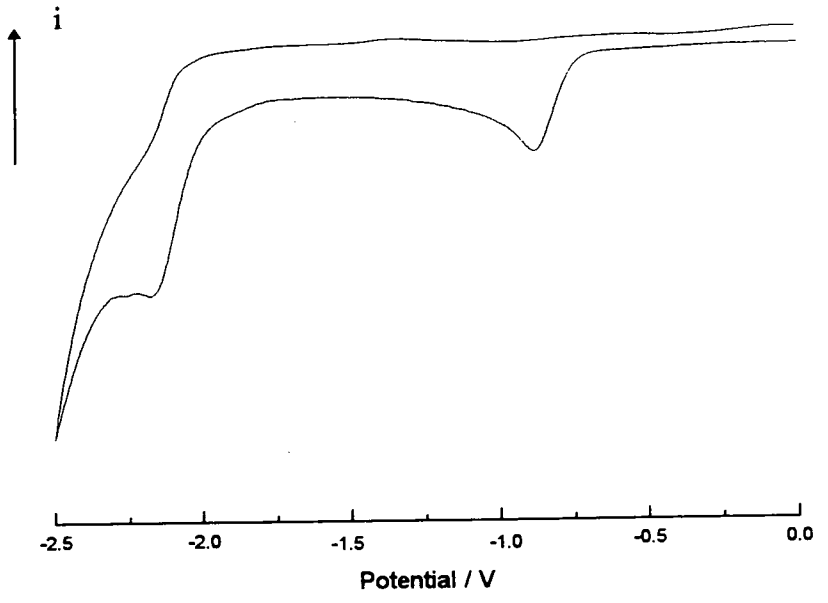

Figure 3.10 Cyclic voltammogram of $[Pd(bpy)Cl_2]$ in 0.1 M $TBABF_4$/DMF at 293 K

3.7 Conclusions

The electrochemical and uv/vis/nir spectroelectrochemical results show the first reduction of $[Pt(bpy)L_2]$ to be a ligand localised process to yield $[Pt^{II}(bpy^{\cdot-})L_2]^{\cdot}$. Epr

results indicate a significant (*ca.* 10%) admixture of Pt $5d_{yz}$ orbital in the redox-active orbital. There is a good qualitative agreement between the epr and EHMO results.

It must be stressed that the electronic character of the redox-active LUMO for *all* the complexes studied is very similar. The reduction potentials are close as is the energy of the MLCT transition in the reduced complexes.

By contast to $[Pt(bpy)Cl_2]$, the LUMO of $[Pd(bpy)Cl_2]$ is metal-based. This can be explained by the lower energy of the empty Pd 4d orbitals compared to Pt 5d.

Chapter 4. (4,4'-X_2-2,2'-bipyridine)dichloroplatinum(II), [Pt(4,4'-X_2-bpy)Cl_2]

4.1 Introduction

There has been considerable interest in synthesising derivatives of the 2,2'-bipyridine ligand.[23,24,26,67] By introducing electron-donating or -withdrawing substituents to the rings it is possible to tune the photophysical and electrochemical properties of both the ligand itself and complexes derived therefrom. Of particular interest have been species of general formula $[Ru(4,4'\text{-}X_2\text{-}bpy)_3]^{2+}$ where X is a strong electron-acceptor such as CF_3, NO_2, PEt_3^+, SO_3H or CN.[14,25,27,68-74] It is proposed that such substituents should extend the lifetime of the photoexcited MLCT (d-π^*) state by stabilising the coordinated bpy radical anion formed. An electron-donating X group would be expected to blue-shift absorption MLCT maxima and related emission spectra and shift the $E_{1/2}$ values of ligand based reductions to more negative potentials while an electron-withdrawing X group would be expected to have the reverse effect. For example the cyclic voltammogram of $[Ru(4,4'\text{-}(CO_2Me)_2\text{-}bpy)_3](PF_6)_2$ reveals six ligand-based reductions at -0.89, -1.01, -1.19, -1.63, -1.83 and -2.15 V *vs.* SCE in 0.1 M $TBABF_4$/MeCN solution rather than the three observed at -1.27, -1.46 and -1.70 V for the parent complex $[Ru(bpy)_3](PF_6)_2$ within the same potential window.[14] Thus the electron-withdrawing effect of the ester moieties makes the second reductions of the bpy ligands accessible.

Various authors have tried to correlate the physical properties of 4,4'-disubstituted bipyridines with σ_p, the Hammett parameter of the substituent X (essentially a measure of the electron-withdrawing or -donating power of X[75]). Connor *et al.* report a linear correlation of σ_p with the emission and absorption maxima of $[Mo(4,4'\text{-}X_2\text{-}bpy)(CO)_4]$ (X=NMe_2, NH_2, OMe, CMe_3, Me, H, Ph, CO_2H, Cl, CO_2Me, NO_2) and the $E_{1/2}$ of the first ligand-based reduction (X=NMe_2, CMe_3, Cl, CO_2Me).[76] Worf *et al.* note similar correlations for $[Re(4,4'\text{-}X_2\text{-}bpy)(CO)_3Cl]$.[31]

A few platinum complexes of derivatised bpys have been reported. Miskowski *et al.* reported that [Pt(3,3'-$(CO_2Me)_2$-bpy)Cl_2] has a lowest energy ^{3}MLCT excited state.[54] They also noted the distorted nature of the ligand set due to the steric demands of the 3 and 3' positions. Other reports have noted the uv/vis absorption spectra of [Pt(4,4'-X_2-bpy)$(CN)_2$] (X=Me, CO_2H, t-Bu) and [M(3,3'-$(CO_2Me)_2$-bpy)Cl_2] (M=Pd and Pt).[77,78]

In this chapter we report the synthesis, redox chemistry and spectroelectrochemistry (uv/vis/nir, epr) of a series of complexes of general formula [Pt(4,4'-X_2-bpy)Cl_2] where X is changed systematically from a powerful electron-donor (X=NH_2) to a powerful electron-acceptor (X=NO_2). The choice of 4 and 4' substituents ensures that only changes due to electronic (and not steric) factors are observed. We present good evidence that the redox orbital is similar in each case, *i.e.* the lowest unoccupied π^* orbital of the X_2bpy ligand. We also show that the metal-based LUMO of [Pd(4,4'-X_2-bpy)Cl_2] is unaffected by substituting X= CO_2Me for X=H. The complexes [M(4,4'-$(NO_2)_2$-bpy)Cl_2] (M=Pd, Pt) exhibit unique electrochemical behaviour and are considered separately in chapter 5.

4.2 4,4'-X_2-2,2'-Bipyridine Ligands

All the ligands studied except X=NH_2 (X=OEt, Me, H, Ph, Cl, CO_2Me and NO_2) undergo reductive processes as shown by cyclic voltammetry (table 4.1). Bpy itself (X=H) undergoes a reversible one-electron reduction at -2.05 V *vs.* Ag/AgCl in 0.1 M $TBABF_4$/DMF solution. The one-electron reductions of 4,4'-$(OEt)_2$-bpy and 4,4'-Cl_2-bpy are completely chemically irreversible showing no anodic peaks at all temperatures and scan speeds studied, *i.e.* the anionic species rapidly decompose. No reduction is observed for 4,4'-$(NH_2)_2$-bpy, presumably because the reduction lies at more negative potentials than the solvent breakdown limit (*ca.* -2.5 V). Table 4.1 shows that the presence of electron-withdrawing substituents facilitates reduction of the ligand *i.e.* the ligand reduces at more positive potentials, while electron-donating substituents have the opposite effect. A second reduction is observed for 4,4'-

$(CO_2Me)_2$-bpy at a potential 490 mV more negative than the first. This probably corresponds to the spin pairing of the second reduction electron with the first, *i.e.* the second reduction electron enters the same π^* orbital as the first reduction electron.

Table 4.1 Redox potentials of 4,4'-X_2-bpy

X	E_1/ V	E_2/ V
NH_2	-	-
OEt	-2.33[a]	-
Me	-2.13[b](0.140)[c]	-
H	-2.05(0.100)	-
Ph	-1.79(0.060)	-
Cl	-1.69[a]	-
CO_2Me	-1.48(0.070)	-1.97(0.130)

(a) irreversible, cathodic peak quoted

(b) $(E_f+E_r)/2$, (c) (E_f-E_r)

4.3 Synthesis of [Pt(4,4'-X_2-bpy)Cl_2]

The complexes [Pt(4,4'-X_2-bpy)Cl_2] (X=NH_2 (**VII**), OEt (**VIII**), Me (**IX**),Ph (**X**), H (**I**), Cl (**XI**), CO_2Me (**XII**) and NO_2 (**XIII**)) were prepared by heating to reflux a suspension of the appropriate ligand in an aqueous solution of $K_2[PtCl_4]$. It is interesting to note the variation in reflux times required to attain a reasonable yield (*ca.* 80%) of the product, varying from 15 minutes for **VII** to 5 hours for **XIII**. Thus the electron-withdrawing substituent deactivates the free ligand towards coordination while an electron-donating substituent activates the ligand. This is reflected in the pK_a values of the ligands. For example 4,4'-$(NO_2)_2$-bpy has a pK_a value of 0.06 compared to 4.27 for bpy itself,[69] *i.e.* it is considerably less basic and is less able to donate electron density from the lone pairs of electrons on the ring nitrogens to the metal. Full experimental details are given in chapter 2.

4.4 Redox Chemistry of [Pt(4,4'-X_2-bpy)Cl_2]

Cyclic voltammetric studies of **VIII-XII** in 0.1 M $TBABF_4$/DMF solution at 293 K reveal a fully reversible reduction process at potentials from -1.23 to -0.67 V (**VIII** and **XII** respectively, table 4.2). Coulometric studies at 243 K confirm a one-electron process in each case. The reduction of **VII** is irreversible at ambient temperatures showing no anodic peak. At 213 K a return wave is observed - yielding an $E_{1/2}$ of -1.53 V - along with an associated daughter peak at -0.11 V (figure 4.1). Thus the electron transfer process is followed by a rapid chemical reaction for **VII**. The nature of the daughter product was not investigated further.

Table 4.2 Redox potentials of [Pt(4,4'-X_2-bpy)Cl_2]

Complex	σ_p[a]	E_1/ V	E_2/ V	E_1-E_2/ V
VII	-0.66	-1.53[b](0.140)[c]	-	-
VIII	-0.24	-1.23(0.070)	-1.86(0.160)	0.630
IX	-0.17	-1.16(0.070)	-1.92[d]	0.760
X	-0.01	-1.01(0.070)	-1.62(0.110)	0.610
I	0.00	-1.06(0.070)	-1.79(0.110)	0.730
XI	0.23	-0.83(0.080)	-1.56[d]	0.730
XII	0.45	-0.67(0.070)	-1.25(0.080)	0.580

(a) Hammett parameter for substituent X, reference 75, (b) $(E_f+E_r)/2$, (c) (E_f-E_r)

(d) anodic peak not observed, cathodic peak quoted

For all other complexes a second reduction process is observed at potentials 580-760 mV more negative than the first. This potential separation is associated with the spin pairing energy of the two added electrons in the redox-active orbital. The second reduction is fully reversible for **XII** (figure 4.2), quasi-reversible for **VIII** and **X** but irreversible for **IX** and **XI**.

The $E_{1/2}$ of the first reduction process varies linearly with the Hammett parameter σ_p of the substituent X (figure 4.3) for all the complexes studied. Such a correlation is indicative of a similar reaction mechanism in each case, *viz.*, reduction of the bipyridyl

moiety. Thus electron-withdrawing substituents stabilise the LUMO while electron-donors destabilise the LUMO of [Pt(4,4'-X_2-bpy)Cl_2] compared to [Pt(bpy)Cl_2].

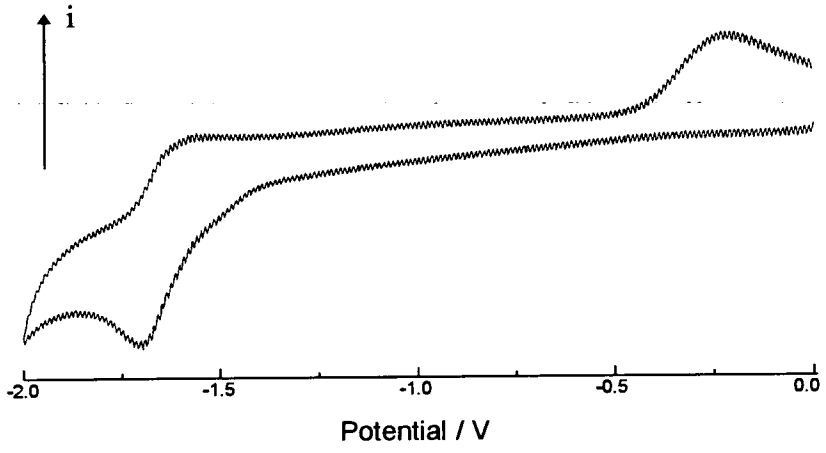

Figure 4.1 Cyclic voltammogram of **VII** at 213 K in 0.1 M $TBABF_4$/DMF solution

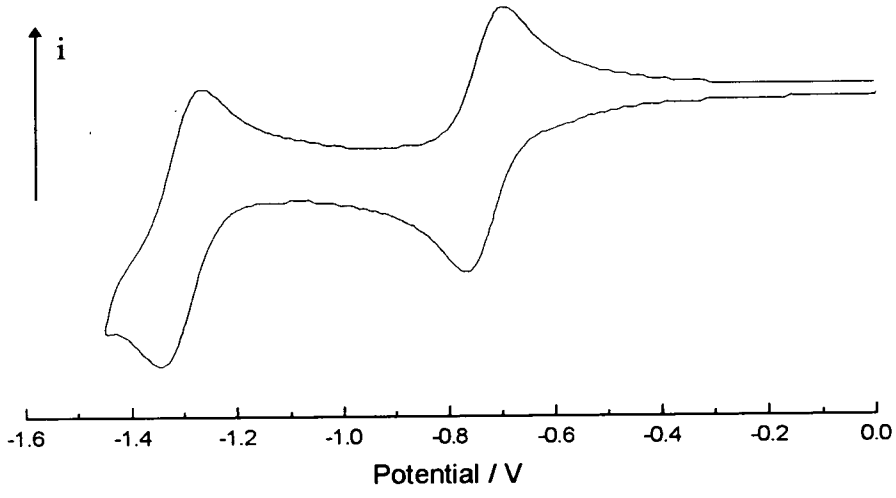

Figure 4.2 Cyclic voltammogram of **XII** at 293 K in 0.1 M $TBABF_4$/DMF solution

4.5 Uv/Vis/Nir Spectroelectrochemistry

The lowest energy features in the uv/vis spectrum of [Pt(4,4'-X_2-bpy)Cl_2] in DMF solution are assigned as MLCT (d-π^*) by comparison with the spectrum of **I** (table 4.3). Other higher energy bands are seen which are probably combinations of internal ligand $\pi-\pi^*$ and higher energy MLCT transitions (for example figure 4.4). The ν_{max} of the MLCT transition in DMF solution varies linearly with σ_p (figure 4.5). This is consistent with the observed electrochemical trends.

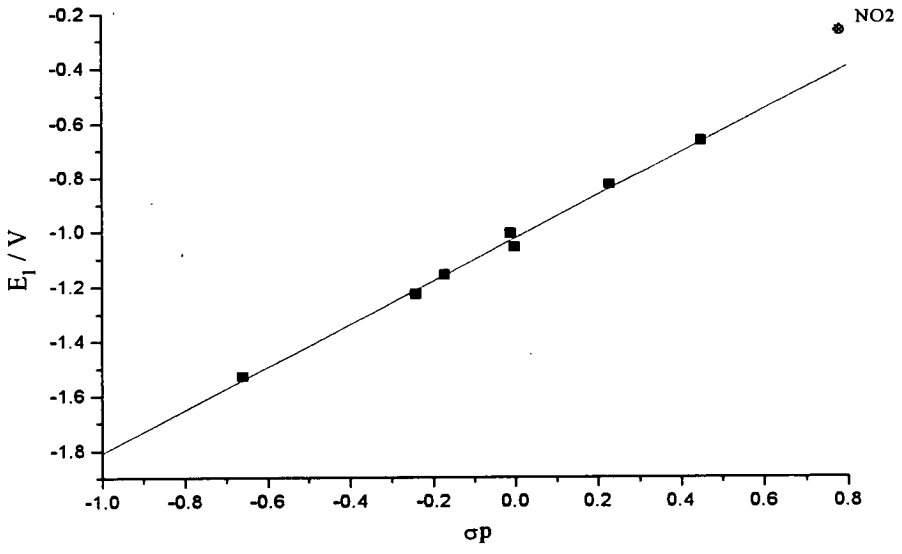

Figure 4.3 E_1 of [Pt(4,4'-X_2-bpy)Cl_2] *versus* Hammet parameter σ_p

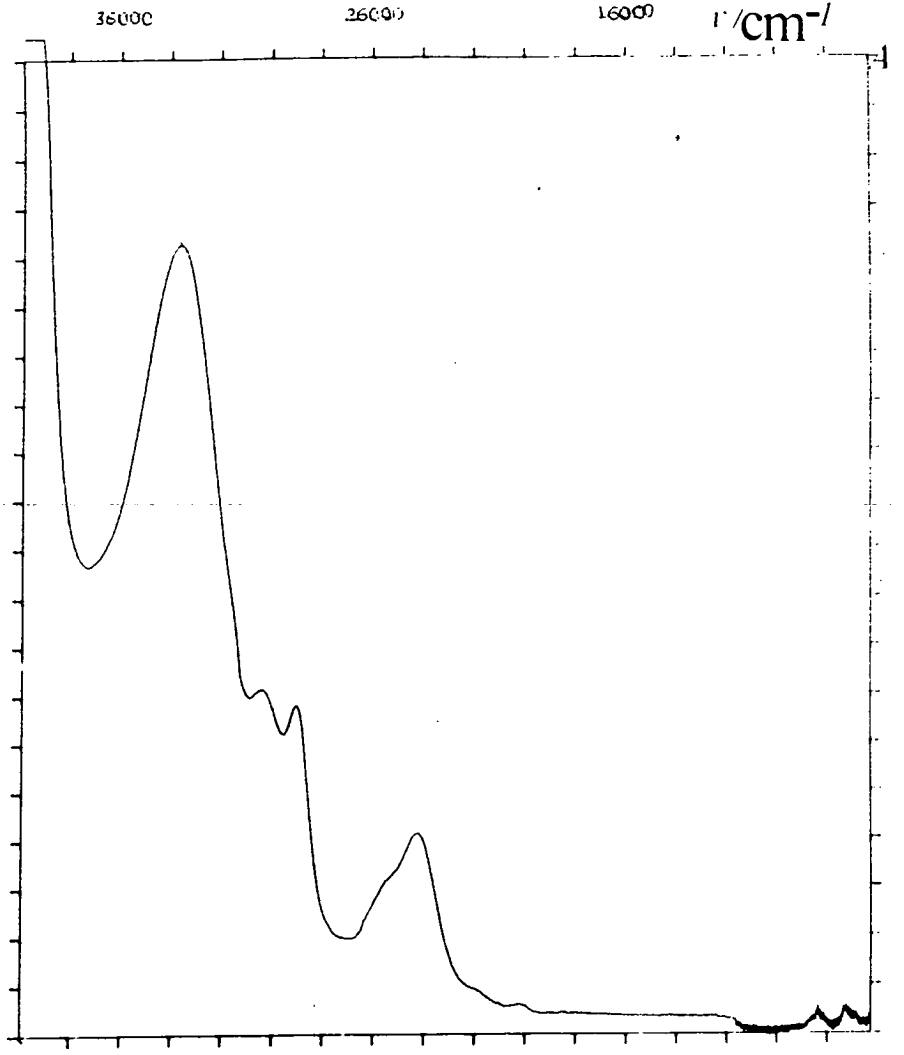

Figure 4.4 Uv/vis spectrum of **XII** in DMF solution

Table 4.3 MLCT ν_{max} of [Pt(4,4'-X_2-bpy)Cl_2] in DMF solution

Complex	σ_p[a]	MLCT ν_{max} / kcm^{-1}
VII	-0.66	27.6 (0.19)[b]
VIII	-0.24	26.2 (0.27)
IX	-0.17	26.0 (0.27)
X	-0.01	25.0 (0.45)
I	0.00	25.7 (0.45)
XI	0.23	24.8 (0.15)
XII	0.45	24.1 (0.54)

(a) Hammett parameter of substituent X, reference 75, (b) ε / 10^4 $M^{-1}cm^{-1}$

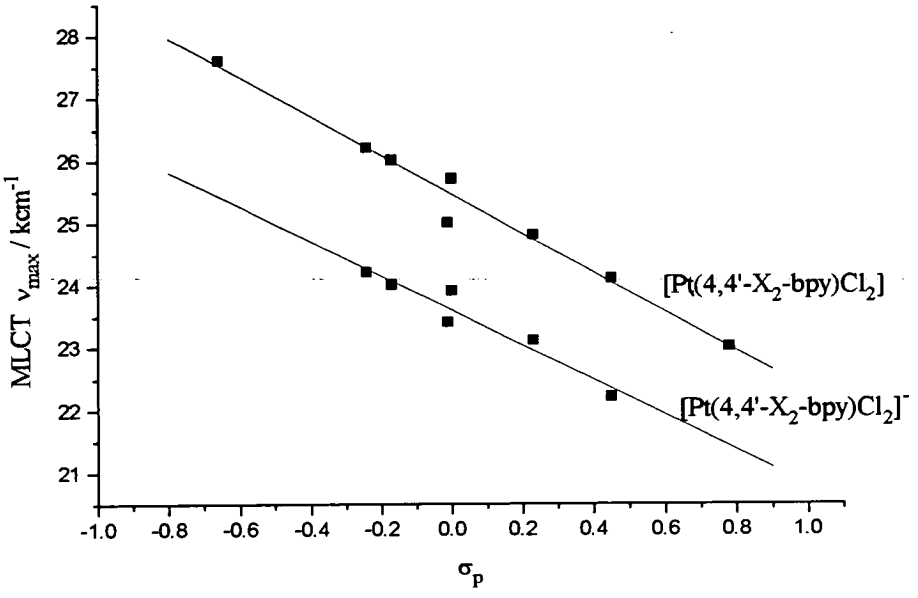

Figure 4.5 MLCT ν_{max} of [Pt(4,4'-X_2-bpy)Cl_2] *versus* Hammett parameter σ_p

It is interesting to note that the equivalent MLCT transition in [Pt(3,3'-$(CO_2Me)_2$-bpy)Cl_2] is observed at 23.1 kcm^{-1} in DMF solution (22.5 kcm^{-1} in $CHCl_3$ or CH_2Cl_2 solution)[54,78] compared to 24.1 kcm^{-1} for [Pt(4,4'-$(CO_2Me)_2$-bpy)Cl_2], *i.e.* the 3,3' ligand is a better electron-acceptor than the 4,4' derivative. This is supported by electrochemical measurements in 0.1 M $TBABF_4$/DMF solution which show two reversible reductions at -0.56 V(0.070) and -1.21 V(0.070) *vs.* Ag/AgCl. This is curious as the buckled nature of the ligand in the 3,3' derivative would be expected to decrease the aromaticity of the ligand and consequently make the ligand a poorer electron-acceptor.[54]

On reduction of complexes **X** and **XII** to **X**$^-$ and **XII**$^-$ at 243 K uv/vis/nir spectra are obtained which are similar to that of **I**$^-$, *i.e.* the bands expected for the coordinated anion radical bpy$^-$ (for example figure 4.6) and a red-shifted MLCT band are observed, and the transitions are assigned similarly. Complex **VII** was not studied due to the irreversibilty of its reduction. Complexes **VIII**$^-$, **IX**$^-$ and **XI**$^-$ show the expected transitions in the visible and uv regions of their spectra but the broad near

infra-red band is absent above 6000 cm^{-1} (table 4.4). This may be due to differences in the uv/vis/nir spectra of the reduced forms of the modified X_2bpy ligands. However, the uv/vis/nir spectra of the mono-reduced ligands $(4,4'\text{-}(CO_2Me)_2\text{-bpy})^-$ and $(4,4'\text{-}Ph_2\text{-bpy})^-$, generated in an OTE cell at 243 K, bear little resemblance to the spectra of their reduced complexes **XII**$^-$ and **X**$^-$. The other ligands could not be studied due to the irreversible nature of their reduction processes as shown by cyclic voltammetry. For a meaningful comparison of the uv/vis/nir spectra of the reduced ligands with those of $[Pt(4,4'\text{-}X_2\text{-bpy})Cl_2]^-$, the free ligand in the reduced form, a planar molecule, must be forced into a cis-geometry, *i.e.* the ring nitrogens must lie on the same side of the C-C bridge. This is the case for the ion-pair $Na^+(bpy^-)$ but not for the electrochemically reduced species which will adopt a trans-geometry.

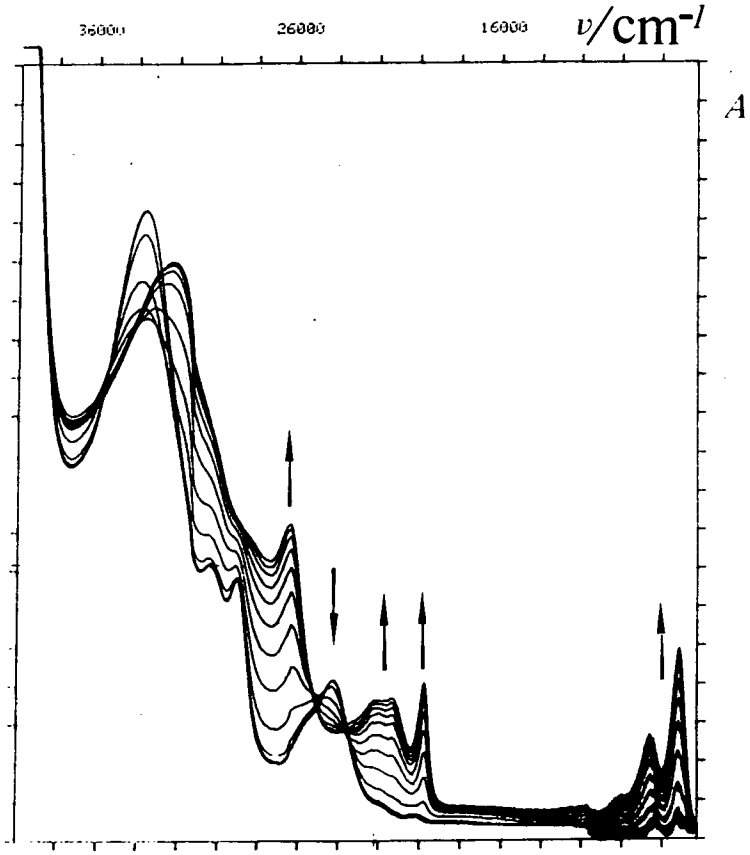

Figure 4.6 OTE reduction of $\mathbf{XII}^{0/-}$ in 0.1 M $TBABF_4$/DMF at 243 K

Table 4.4 Uv/vis/nir spectra of $[Pt(4,4'\text{-}X_2\text{-}bpy)Cl_2]^-$ in 0.1M $TBABF_4$/DMF at 243 K

Complex	π(7-8,9)*	π(7-10)*	MLCT	π(6-7)*/ kcm^{-1}
VIII$^-$	-	20.2, 21.8	24.2	28.6
IX$^-$	-	19.7, 21.2	24.0	29.1
X$^-$	8.4	17.9, 19.2	23.4[a]	27.1
I$^-$	11.2	20.1, 21.6	23.9	25.9
XI$^-$	-	19.8, 21.2	23.1	27.6
XII$^-$	7.2, 8.6	19.8, 21.3	22.2[a]	26.4

(a) shoulder

The ν_{max} of the MLCT transition in the anionic species varies linearly with σ_p (figure 4.5, table 4.3). This supports the assignment of this transition as the Pt d to singly-occupied X_2bpy π* orbital.

4.6 Epr Spectroelectrochemistry

Bulk electrochemical reduction of **VIII-XII** in 0.1 M $TBABF_4$/DMF solution at 243 K yields epr active solutions. The room temperature solution epr spectra of **VIII**$^-$ and **X**$^-$-**XII**$^-$ are all similar showing a broad central line with ^{195}Pt satellites and can be interpreted as for **I**$^-$, that is, coupling of the unpaired electron to the Pt nucleus with any superhyperfine coupling to ligand nuclei unresolved. Complexes **VIII**, **X** and **XI** can be chemically reduced with $NaBH_4$ to give rise to spectra which are identical to those generated by electrochemical reduction. Likewise **XII** can be reduced with cobaltocene. Note that cobaltocene is not a powerful enough reducing agent to reduce the other compounds. **IX** decomposes on reduction with $NaBH_4$ to yield epr silent species.

On cooling to 77 K rhombic X-band epr spectra are obtained similar to that observed for **I**$^-$ (figure 4.7, table 4.5) and may be treated similarly. Again the high-field g_3 ^{195}Pt coupling is not resolved in any of the spectra. A_3 can be estimated from the magnitudes of A_{iso}, A_1 and A_2 (equation 2). The estimated A_3 for **IX**$^-$ assumes a

similar isotropic coupling to **I**. The estimated A_3 values are listed in table 4.5 and lie in the range 5-25x10^{-4} cm^{-1}. In all cases A_3 appears to have the same sign as A_1, A_2 and A_{iso}.

$$A_3 = 3A_{iso}-(A_1+A_2) \qquad (2)$$

Table 4.5 Epr parameters for $[Pt(4,4'-X_2-bpy)Cl_2]^-$

Complex	g_{iso}[a]	g_1[b]	g_2	g_3	A_{iso}[c]	A_1	A_2	A_3
VIII$^-$	2.001[d]	2.031	2.010	1.964	-44	-46	-63	(-23)
IX$^-$	-	2.036	2.011	1.946	-	-53	-85	(-24)
X$^-$	1.999	2.040	2.011	1.939	-54	-55	-93	(-14)
I$^-$	1.998	2.038	2.009	1.935	-54	-56	-95	(-11)
XI$^-$	2.000	2.042	2.014	1.944	-51	-52	-96	(-5)
XII$^-$	1.997	2.052	2.010	1.925	-60	-61	-100	(-19)

(a) isotropic data from chemically generated species in DMF, (b) anisotropic data from electrochemically generated species in 0.1 M $TBABF_4$/DMF, (c) A / 10^{-4} cm^{-1}, (d) all parameters estimated directly from spectra

A_1, A_2, A_3, g_1, g_2 and g_3 can be assigned to the molecular axes x, y and z as for **I**. Hence, g_2 and A_2 are assigned to g_x and A_x respectively. The Pt $5d_{yz}$ orbital admixture to the SOMO of $[Pt(4,4'-X_2-bpy)Cl_2]^-$ can be calculated using equation 1. The d_{yz} orbital is still the only d-orbital of the correct symmetry to mix with the ligand π^* orbital. Tables 4.5 and 4.6 show that as X changes from an electron-donor (**VIII**$^-$) to an electron-acceptor (**XII**$^-$) the g anisotropy (g_1-g_3) and ^{195}Pt hyperfine coupling constants increase. This indicates an increasing metal d_{yz}-orbital admixture to the primarily ligand-based SOMO. This is borne out by the calculated a^2 values where a^2 is the Pt $5d_{yz}$-orbital admixture to the SOMO (in calculating a^2 for **I**$^-$ in table 4.6 the experimental epr data were used as simulations were not available for the others in the series. Thus, the a^2 value calculated here is slightly higher than in chapter 3). This can be explained simply in molecular orbital terms. As the ligand π^* orbital energy is decreased by adding electron-withdrawing substituents there is a

better energy match with the filled low-lying $5d_{yz}$ orbital and hence a more efficient orbital overlap. This results in a ligand-based π^* orbital with increased metal character.

Table 4.6 Pt $5d_{yz}$ orbital admixtures to SOMO of $[Pt(4,4'\text{-}X_2\text{-}bpy)Cl_2]^-$

Complex	g_1-g_3	a^2
VIII$^-$	0.067	0.08
IX$^-$	0.090	0.13
X$^-$	0.101	0.15
I$^-$	0.103	0.16
XI$^-$	0.098	0.18
XII$^-$	0.127	0.16

On electrogenerating the dianionic species **XII**$^{2-}$ an epr signal is obtained at 77 K identical to that of the monoanion but with greatly reduced intensities. This signal is presumably due to residual monoanion **XII**$^-$, where **XII**$^{2-}$ is epr silent. Thus, the second added electron, corresponding to the second reduction process in the cyclic voltammogram, is spin-pairing with the first in the same π^* orbital to yield a diamagnetic product. This is consistent with the potential separation of the first and second reduction.

4.7 Redox Chemistry of $[Pd(4,4'\text{-}(CO_2Me)_2\text{-}bpy)Cl_2]$

$[Pd(4,4'\text{-}(CO_2Me)_2\text{-}bpy)Cl_2]$ undergoes a broad, irreversible two-electron (by coulometry) reduction at -0.70 V in 0.1 M $TBABF_4$/DMF solution at 293 K resulting in decomposition of the complex. Thus, despite the strong electron-withdrawing ester groups the lowest unoccupied π^* orbital of the ligand still lies above the 4d metal-based LUMO.

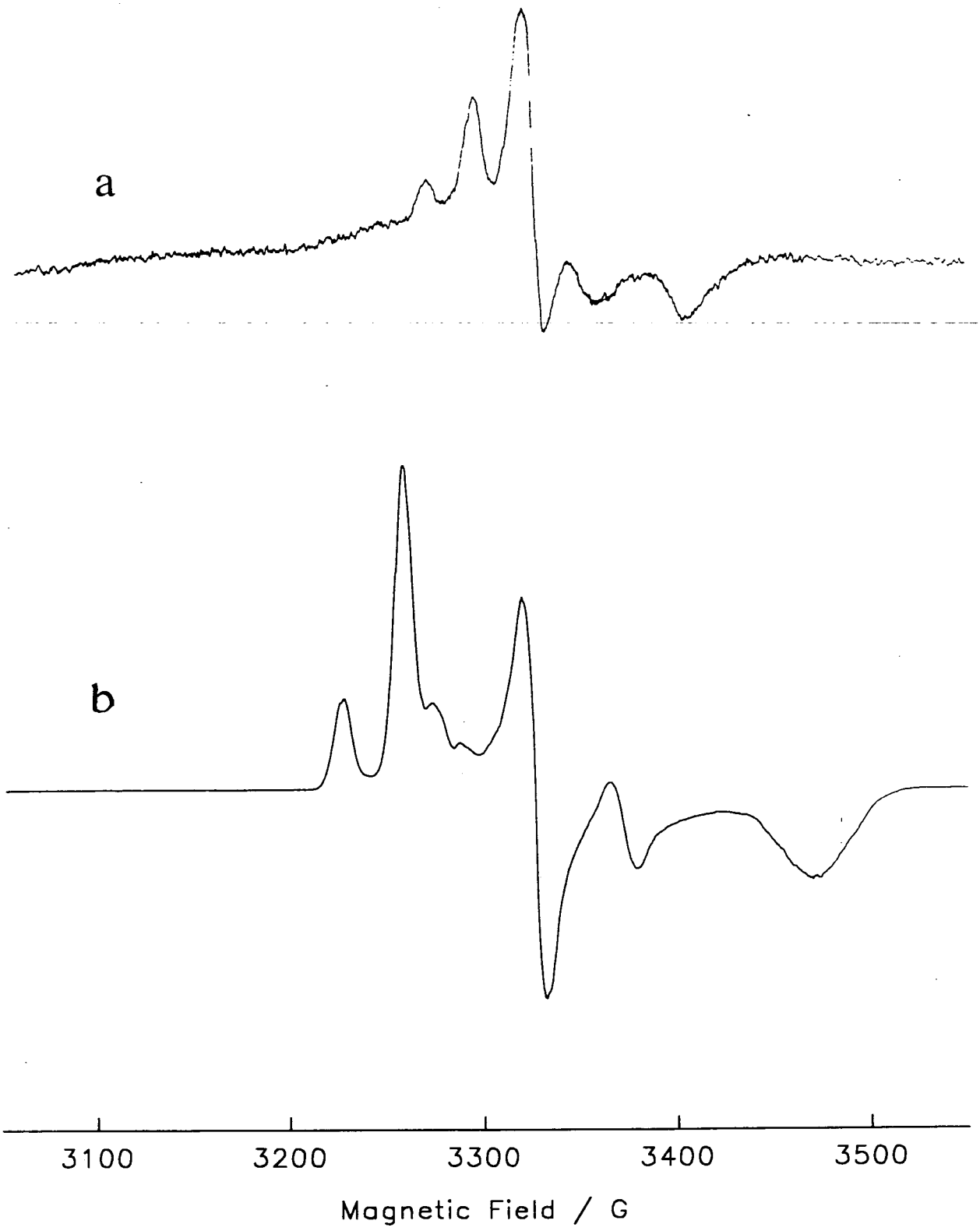

Figure 4.7 77 K epr spectra of **VIII**$^{-}$ (a) and **XII**$^{-}$ (b) in 0.1 M $TBABF_4$/DMF

4.8 Conclusions

The redox chemistry of [Pt(4,4'-X_2-bpy)Cl_2] can be explained in terms of two electrons entering the same orbital, *viz.*, the lowest unoccupied π^* orbital of the X_2bpy ligand. There is one exception where X=NH_2. Here a rapid decomposition follows the first electron transfer process. We can still assign the redox orbital as bpy based on the basis of the $E_{1/2}$ of the reduction process. Systematic variations in the substituent X allow us to control the energy of the π^* LUMO.

Chapter 5. Complexes of 4,4'-dinitro-2,2'-bipyridine

5.1 Introduction

Few transition metal complexes of 4,4'-$(NO_2)_2$-bpy and its mono-substituted analogue have been reported.[31,69-72,76] Basu *et al.* have concluded from resonance enhanced Raman vibrational spectra that there is extensive charge-transfer to the nitro group in the MLCT excited-state of $[Ru(4\text{-}(NO_2)\text{-}bpy)_3]^{2+}$, *i.e.* the ligand π^* orbital is highly delocalised onto the nitro group.[70,71] They then explain the puzzling lack of luminescence of these species as being due to vibrational depopulation of the excited state *via* solvent coupling to the nitro group. However, Cook *et al.* have reported an emission spectrum for $[Ru(4,4'\text{-}(NO_2)_2\text{-}bpy)_3]^{2+}$ centered at 700 nm in an EtOH/MeOH solution (4:1 v/v) at 293 K, red-shifted compared to the emission at 630 nm observed for $[Ru(bpy)_3]^{2+}$ under the same conditions.[27,72]

4,4'-$(NO_2)_2$-bpy has been reported to undergo two consecutive one-electron reductions at -0.80 and -0.91 V *vs.* SCE.[69] Only one complex of this ligand has been studied electrochemically. $[Re(4,4'\text{-}(NO_2)_2\text{-}bpy)(CO)_3Cl]$ is reported to undergo one ligand-based reduction process at -0.45 V *vs.* SCE in MeCN solution.[31]

In this chapter we reinvestigate the redox chemistry of $[Re(4,4'\text{-}(NO_2)_2\text{-}bpy)(CO)_3Cl]$ and of the square-planar, d^8 complexes $[M(4,4'\text{-}(NO_2)_2\text{-}bpy)L_2]^{n+}$ (M=Pd, Pt, L=Cl^-, n=0; M=Rh, L_2=1,5-cyclooctadiene, n=1). We find the complexed ligand can undergo four one-electron reduction processes and support the conclusion that the redox-orbitals are highly localised on the nitro groups.

5.2 Redox Chemistry of 4,4'-$(NO_2)_2$-bpy

4,4'-$(NO_2)_2$-bpy undergoes two quasi-reversible reductions at -0.65 V(0.100) and -0.79 V(0.170) and a third, poorly defined irreversible process at *ca.* -1.6 V *vs.* Ag/AgCl in 0.1

M $TBABF_4$/DMF solution at 293 K (figure 5.1). The small separation between E_1 and E_2 of 140 mV is inconsistent with spin pairing of the two added electrons in the same π^* orbital.

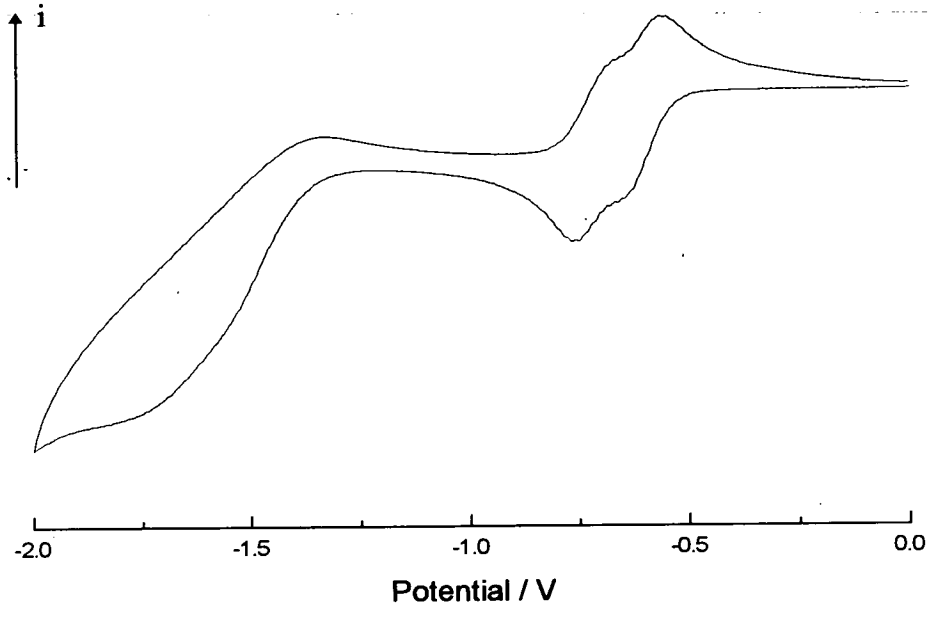

Figure 5.1 Cyclic voltammogram of 4,4'-$(NO_2)_2$-bpy in 0.1 M $TBABF_4$/DMF at 293 K

5.3 Synthesis of $[M(4,4'\text{-}(NO_2)_2\text{-}bpy)L_2]^{n+}$

$[M(4,4'\text{-}(NO_2)_2\text{-}bpy)Cl_2]$ (M= Pd and Pt) were prepared by heating to reflux a suspension of the free ligand in an aqueous solution of $K_2[MCl_4]$ for 3 to 4 hours. As noted in chapter 4, longer reflux times are required than for the analogous bpy complexes. $[Rh(4,4'\text{-}(NO_2)_2\text{-}bpy)(cod)]ClO_4$ was prepared by stirring a suspension of the free ligand with $[Rh(cod)Cl]_2$ for 1 hour at room temperature and addition of $NaClO_4$. This again requires a longer reaction time than for the analogous bpy complex

$[Rh(bpy)(cod)]ClO_4$ which is prepared by the same route but with stirring for 5 minutes.[34] Full experimental details are given in chapter 2.

5.4 Redox Chemistry of $[M(4,4'\text{-}(NO_2)_2\text{-}bpy)L_2]^{n+}$

Cyclic voltammetric studies of $[Pt(4,4'\text{-}(NO_2)_2\text{-}bpy)Cl_2]$ (**XIII**) in 0.1 M $TBABF_4$/DMF solution reveals four consecutive one-electron reductions in the 0 to -2 V range (figure 5.2a, table 5.1). The first two are fully reversible reductions while the third and fourth are quasi-reversible and irreversible respectively. This is perhaps unsurprising as the molecule carries a large charge of 4- after the fourth reduction. As for the free ligand the E_1-E_2 separation of 180 mV is too small to be considered a spin-pairing process, *i.e.* the first and second reduction electrons are entering different orbitals. Thus the redox chemistry suggests that the LUMO-second LUMO (SLUMO) gap is less than the spin pairing energy. The E_1-E_3 and E_2-E_4 separations of 780 and 1050 mV could be consistent with spin-pairing processes.

Figure 4.3 shows that the point for **XIII** lies off the Hammett curve for $E_{1/2}$ *vs.* σ_p. For the value of σ_p as quoted in the literature, +0.78,[75] the $E_{1/2}$ of the first reduction should be more negative (*i.e.* the reduction should be harder than observed). This indicates an extensive localisation of the added charge onto the positively charged nitrogen nuclei of the nitro groups, or in other words an extensive delocalisation of the π^* system onto the nitro groups. However, the MLCT ν_{max} position of **XIII** at 23.0 kcm^{-1} in DMF solution fits well on the Hammett curve for ν_{max} *vs.* σ_p (figure 4.5).

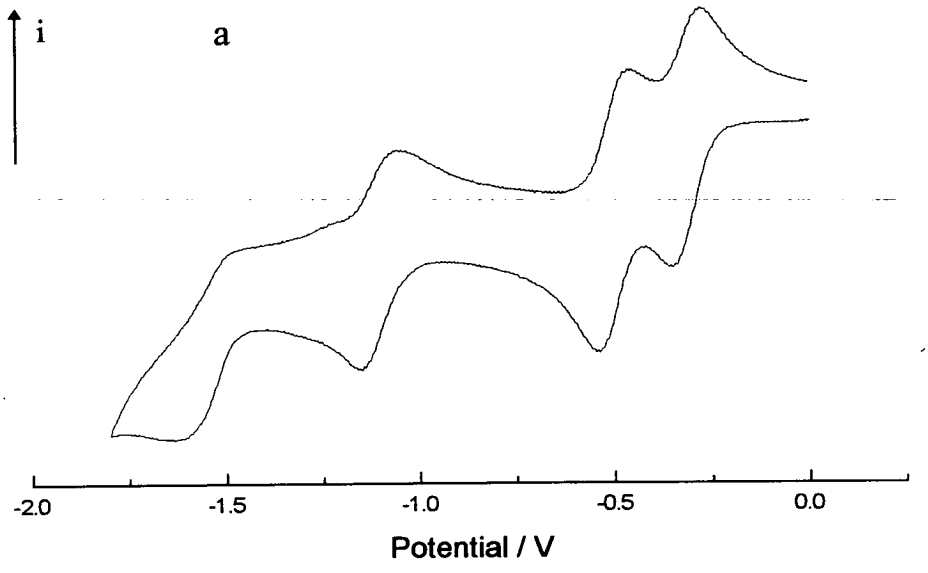

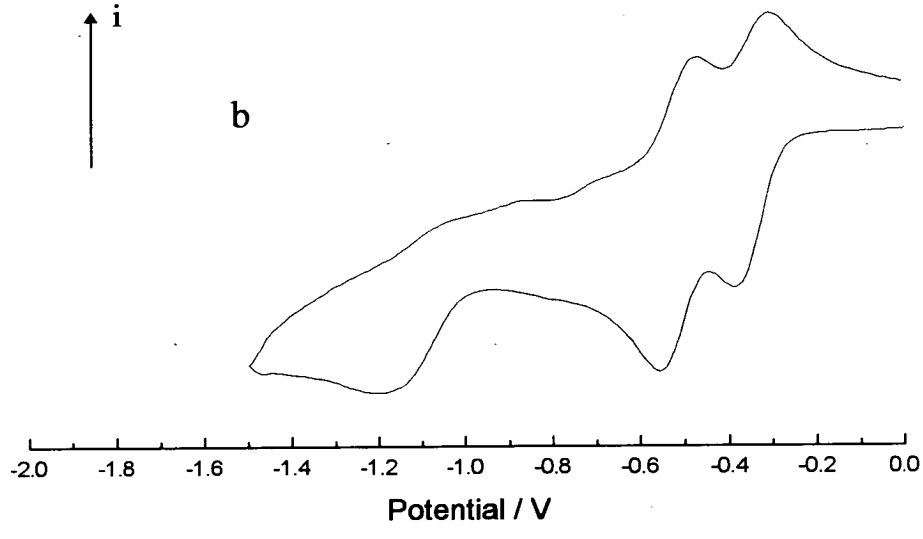

Figure 5.2 Cyclic voltammograms of **XIII** (a) and **XIV** (b) in 0.1 M $TBABF_4$/DMF at 293 K

[Pd(4,4'-$(NO_2)_2$-bpy)Cl_2] (**XIV**) undergoes two reversible one-electron reductions at -0.27 and -0.45 V followed by a broad irreversible reduction at -1.06 V (figure 5.2b, table 5.1). Thus, by substituting X=NO_2 for X=H or CO_2Me the LUMO of [Pd(4,4'-X_2-bpy)Cl_2] is changed from metal- to ligand-based. The similarity between the first two reduction potentials of **XIII** and **XIV** suggests that the change in metal from Pd to Pt has little effect on the ligand orbital energies. The third reduction of **XIV** may be the metal-based reduction, rather than the third ligand-based reduction. The irreversibility of this process and the absence of a fourth reduction in the cyclic voltammogram support this hypothesis.

Table 5.1 Redox potentials of $[M(4,4'\text{-}(NO_2)_2\text{-bpy})L_2]^{n+}$

Complex	E_1/ V	E_2/ V	E_3/ V	E_4/ V	Solvent
XIII	-0.27[a](0.080)[b]	-0.45(0.080)	-1.05(0.100)	-1.50(0.170)	DMF
XIV	-0.27(0.080)	-0.45(0.080)	-1.06	-	DMF
XV	-0.24(0.060)	-0.39(0.090)	-0.97(0.090)	-1.36(0.160)	DMF
	-0.16(0.070)	-0.35(0.090)	-0.84(0.070)	-1.11(0.130)	CH_2Cl_2
XVI	-0.31(0.070)	-0.45(0.070)	-0.97(0.100)	-1.35(0.380)	MeCN

(a) $(E_f+E_r)/2$, (b) (E_f-E_r)

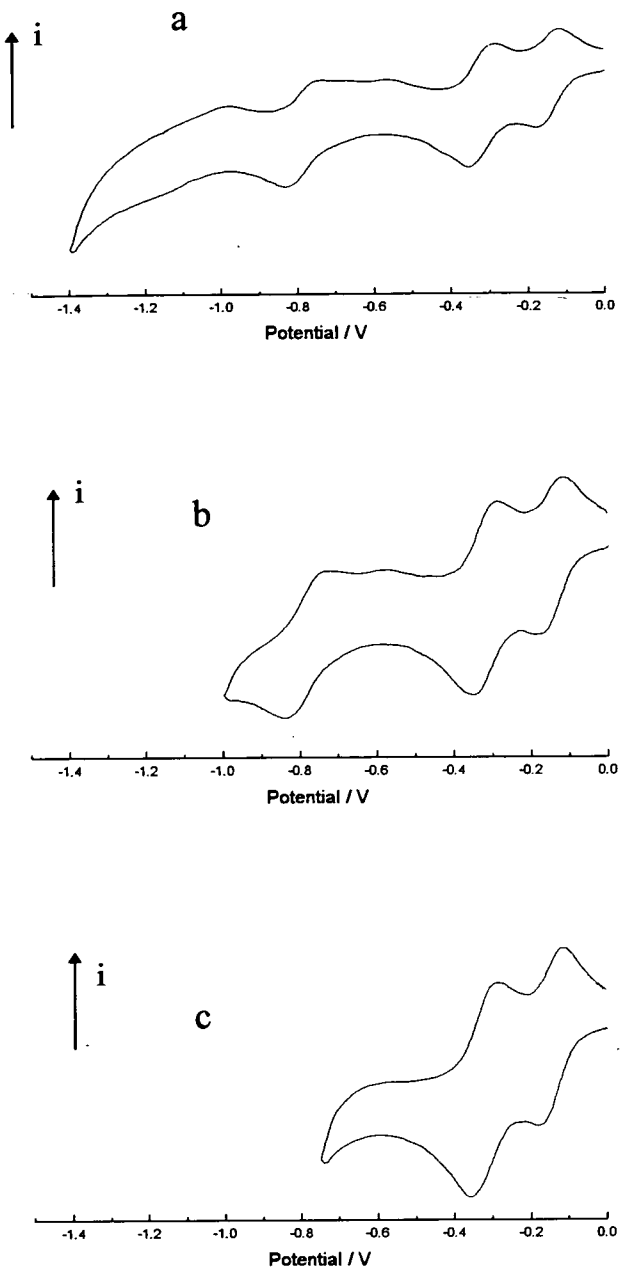

Figure 5.3 Cyclic voltammograms of **XV** in 0.5 M $TBABF_4/CH_2Cl_2$ solution at 293 K

$[Rh(bpy)(cod)]ClO_4$ undergoes two reversible one-electron reductions at -1.26 and -1.73 V *vs.* SCE in 0.1 M $[Et_4N]ClO_4$/MeCN solution.[79] These processes have been assigned

as the first two reductions of the bpy ligand on the basis of their epr spectra ([Rh(bpy)(cod)]$^{-}$ is epr silent). [Rh(4,4'-$(NO_2)_2$-bpy)(cod)]$^{+}$ (**XV**) undergoes the same four reduction processes as **XIII** in 0.5 M $TBABF_4/CH_2Cl_2$ or 0.1 M $TBABF_4$/DMF solution (figure 5.3). There is a significant shift in E_1 of 80 mV between DMF and CH_2Cl_2 solution. This solvatochromic behaviour is also apparent in the uv/vis spectrum of **XV** where the MLCT (d→$(NO_2)_2$bpy π^*) transition shifts from 17.7 kcm^{-1} in DMF solution to 17.0 kcm^{-1} in CH_2Cl_2 solution.

Reduced forms of **XV** are more stable in CH_2Cl_2 solution than DMF as shown by the improved reversibility of the reduction processes in the cyclic voltammogram. Peaks are observed at -0.70 and -0.59 V on the return sweep of the cyclic voltammogram which correspond to reoxidation of the di-reduced form of the free ligand (figure 5.3a). If the switching potential is set just before the third reduction (-0.75 V) then these peaks are not observed, *i.e.* the complex begins to dissociate after the third reduction, liberating the di-reduced form of the free ligand (figure 5.3c).

[Re(4,4'-$(NO_2)_2$-bpy)$(CO)_3$Cl] (**XVI**) is reported to undergo only one ligand-based reduction.[31] In light of the redox chemistry of **XIII**, **XIV** and **XV** this species was reinvestigated. We find that **XVI** does in fact undergo four reductions at -0.31, -0.45, -0.97 and -1.35 V as well as the irreversible Re(I/II) oxidation at +1.65 V (anodic peak) in 0.1 M $TBABF_4$/MeCN solution (figure 5.4). The Re(I/II) oxidation showed no signs of increasing reversibility at low temperatures or at increased scan rates.

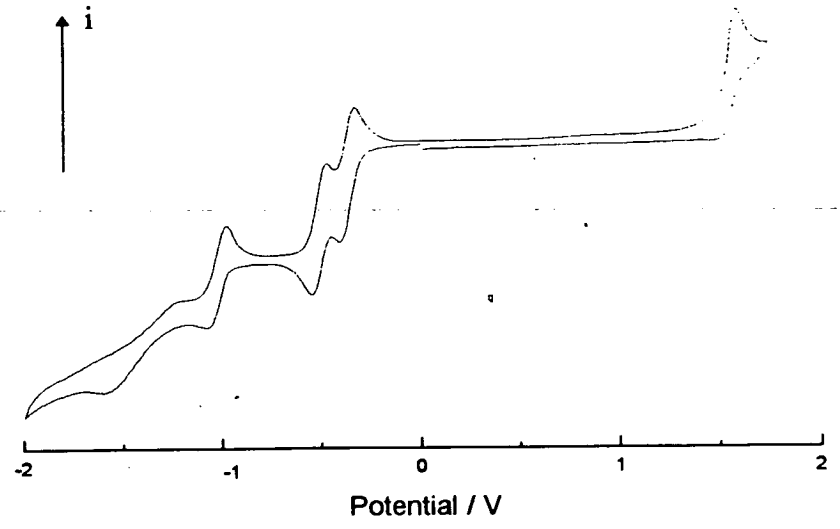

Figure 5.4 Cyclic voltammogram of **XVI** in 0.1 M $TBABF_4$/MeCN solution at 293 K

5.5 Crystal structure of [Pt(4,4'-$(NO_2)_2$-bpy)Cl_2]

A single crystal of **XIII** was grown from MeCN solution. Full experimental details of structure determination are given in chapter 2. Table 5.2 lists interatomic distances and interbond angles. Figure 5.5 shows a view of one of the independent molecules in the unit cell. Despite the refinement problems discussed in chapter 2, the grossly planar nature of the molecule is established. A discussion of the intermolecular packing interactions and a full list of fractional co-ordinates are given in appendix A.

Table 5.2 Interatomic distances (Å) and interbond angles (°) for **XIII**

Pt(A)	-Cl(1A)	2.322(12)	Pt(B)	-Cl(1B)	2.293(13)
Pt(A)	-Cl(2A)	2.240(22)	Pt(B)	-Cl(2B)	2.301(16)
Pt(A)	-N(1A)	2.05(3)	Pt(B)	-N(1B)	1.99(3)
Pt(A)	-N(2A)	1.95(4)	Pt(B)	-N(2B)	1.94(3)
N(1A)	-C(1A)	1.36(5)	N(1B)	-C(1B)	1.40(5)
N(1A)	-C(5A)	1.41(6)	N(1B)	-C(5B)	1.45(5)

C(1A)	-C(2A)	1.39(6)	C(1B)	-C(2B)	1.39(6)
C(1A)	-C(6A)	1.51(6)	C(1B)	-C(6B)	1.44(6)
C(2A)	-C(3A)	1.38(6)	C(2B)	-C(3B)	1.42(5)
C(3A)	-C(4A)	1.37(6)	C(3B)	-C(4B)	1.41(6)
C(3A)	-N(3A)	1.49(5)	C(3B)	-N(3B)	1.47(5)
C(4A)	-C(5A)	1.40(7)	C(4B)	-C(5B)	1.36(6)
N(3A)	-O(1A)	1.18(8)	N(3B)	-O(1B)	1.18(5)
N(3A)	-O(2A)	1.19(6)	N(3B)	-O(2B)	1.15(5)
N(2A)	-C(6A)	1.43(6)	N(2B)	-C(6B)	1.34(5)
N(2A)	-C(10A)	1.41(9)	N(2B)	-C(10B)	1.34(5)
C(6A)	-C(7A)	1.35(6)	C(6B)	-C(7B)	1.37(6)
C(7A)	-C(8A)	1.38(6)	C(7B)	-C(8B)	1.40(6)
C(8A)	-C(9A)	1.42(6)	C(8B)	-C(9B)	1.37(6)
C(8A)	-N(4A)	1.54(7)	C(8B)	-N(4B)	1.53(6)
C(9A)	-C(10A)	1.41(9)	C(9B)	-C(10B)	1.35(6)
N(4A)	-C(3A)	1.17(7)	N(4B)	-O(3B)	1.20(6)
N(4A)	-O(4A)	1.22(7)	N(4B)	-O(4B)	1.14(6)

Cl(1A)	-Pt(A)	-Cl(2A) 89.8(6)	Cl(1B)	-Pt(B)	-Cl(2B) 89.0(5)
Cl(1A)	-Pt(A)	-N(1A) 93.4(9)	Cl(1B)	-Pt(B)	-N(1B) 178.3(9)
Cl(1A)	-Pt(A)	-N(2A) 176.2(13)	Cl(1B)	-Pt(B)	-N(2B) 97.7(10)
Cl(2A)	-Pt(A)	-N(1A) 175.9(10)	Cl(2B)	-Pt(B)	-N(1B) 92.6(9)
Cl(2A)	-Pt(A)	-N(2A) 94.0(14)	Cl(2B)	-Pt(B)	-N(2B) 173.2(10)
N(1A)	-Pt(A)	-N(2A) 82.8(16)	N(1B)	-Pt(B)	-N(2B) 80.7(12)
Pt(A)	-N(1A)	-C(1A) 111.8(25)	Pt(B)	-N(1B)	-C(1B) 112.6(23)
Pt(A)	-N(1A)	-C(5A) 122.9(29)	Pt(B)	-N(1B)	-C(5B) 131.4(23)
C(1A)	-N(1A)	-C(5A) 124.9(36)	C(1B)	-N(1B)	-C(5B) 114.8(29)
N(1A)	-C(1A)	-C(2A) 118.9(38)	N(1B)	-C(1B)	-C(2B) 119.8(34)
N(1A)	-C(1A)	-C(6A) 117.7(36)	N(1B)	-C(1B)	-C(6B) 115.8(33)
C(2A)	-C(1A)	-C(6A) 123.3(38)	C(2B)	-C(1B)	-C(6B) 124.4(36)
C(1A)	-C(2A)	-C(3A) 120.3(40)	C(1B)	-C(2B)	-C(3B) 120.6(36)
C(2A)	-C(3A)	-C(4A) 116.4(37)	C(2B)	-C(3B)	-C(4B) 120.5(36)
C(2A)	-C(3A)	-N(3A) 122.8(37)	C(2B)	-C(3B)	-N(3B) 119.1(33)
C(4A)	-C(3A)	-N(3A) 119.3(35)	C(4B)	-C(3B)	-N(3B) 120.3(35)
C(3A)	-C(4A)	-C(5A) 126.5(40)	C(3B)	-C(4B)	-C(5B) 113.5(39)
N(1A)	-C(5A)	-C(4A) 110.2(41)	N(1B)	-C(5B)	-C(4B) 122.7(36)
C(3A)	-N(3A)	-O(1A) 101.5(46)	C(3B)	-N(3B)	-O(1B) 107.2(31)
C(3A)	-N(3A)	-O(2A) 120.6(38)	C(3B)	-N(3B)	-O(2B) 115.2(34)
O(1A)	-N(3A)	-O(2A) 132.9(53)	O(1B)	-N(3B)	-O(2B) 137.5(39)
Pt(A)	-N(2A)	-C(6A) 116.7(32)	Pt(B)	-N(2B)	-C(6B) 118.9(26)
Pt(A)	-N(2A)	-C(10A) 126.5(44)	Pt(B)	-N(2B)	-C(10B) 126.5(27)
C(6A)	-N(2A)	-C(10A) 111.4(48)	C(6B)	-N(2B)	-C(10B) 113.9(33)
C(1A)	-C(6A)	-N(2A) 110.7(37)	C(1B)	-C(6B)	-N(2B) 111.7(34)
C(1A)	-C(6A)	-C(7A) 122.9(40)	C(1B)	-C(6B)	-C(7B) 124.6(37)
N(2A)	-C(6A)	-C(7A) 126.3(42)	N(2B)	-C(6B)	-C(7B) 123.5(37)
C(6A)	-C(7A)	-C(8A) 115.3(41)	C(6B)	-C(7B)	-C(8B) 116.3(36)
C(7A)	-C(8A)	-C(9A) 121.5(41)	C(7B)	-C(8B)	-C(9B) 123.2(37)
C(7A)	-C(8A)	-N(4A) 117.6(41)	C(7B)	-C(8B)	-N(4B) 115.4(36)
C(9A)	-C(8A)	-N(4A) 120.5(41)	C(9B)	-C(8B)	-N(4B) 120.7(37)
C(8A)	-C(9A)	-C(10A) 115.2(48)	C(8B)	-C(9B)	-C(10B) 111.8(36)
N(2A)	-C(10A)	-C(9A) 115.7(62)	N(2B)	-C(10B)	-C(9B) 129.7(38)
C(8A)	-N(4A)	-O(3A) 111.7(48)	C(8B)	-N(4B)	-O(3B) 116.3(41)
C(8A)	-N(4A)	-O(4A) 120.7(48)	C(8B)	-N(4B)	-O(4B) 119.5(42)
O(3A)	-N(4A)	-O(4A) 125.2(55)	O(3B)	-N(4B)	-O(4B) 123.9(47)

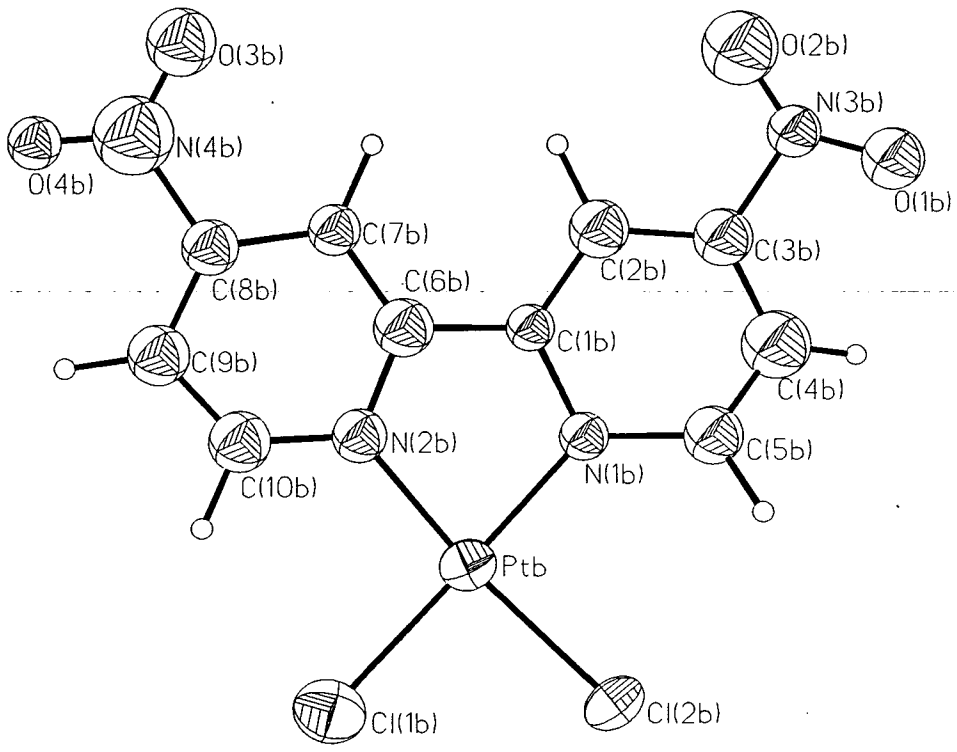

Figure 5.5 Crystal structure of **XIII**

5.6 EHMO Calculations of I *vs.* XIII

Figure 5.6 shows energy level schemes of **I** and **XIII**. The energy of the HOMO, an in plane $d_{x^2-y^2}/\sigma$-bonding orbital, is unaffected by the change in ligand set. The LUMO of **XIII** is at -10.65 eV compared to -9.64 eV for **I**, in good agreement with the observation that **XIII** reduces at a potential 0.74 V more positive than **I**. The LUMO-SLUMO gap of **XIII** is calculated to be 100 meV compared to 670 meV for **I**. This supports the small LUMO-SLUMO gap model proposed to explain the unique electrochemistry of **XIII**. For both **I** and **XIII** the SLUMO is the next highest π^* orbital on the bpy ligand. Nuclear coefficients of the LUMO and SLUMO of **XIII** are given in table 5. Note that N2 and N2' are the nitrogen nuclei of the NO_2 groups. The LUMO and SLUMO of

XIII are 65% and 76% localised on the nitro groups respectively and only differ significantly in their symmetry (b_2 and b_1 respectively).

Table 5.3 Nuclear coefficients of LUMO and SLUMO of **XIII**

Atom	Orbital	LUMO	SLUMO
N1,1'	$2p_z$	0.106	0.061
C2,2'	$2p_z$	0.038	0.019
C3,3'	$2p_z$	0.028	0.081
C4,4'	$2p_z$	0.048	0.030
C5,5'	$2p_z$	0.076	0.038
C6,6'	$2p_z$	0.036	0.021
N2,2'	$2p_z$	0.392	0.456
O1,1'	$2p_z$	0.130	0.144
O2,2'	$2p_z$	0.129	0.145
Pt	$5d_{yz}$	0.024	-
	$5d_{xz}$	-	0.009
	$6p_z$	0.011	-

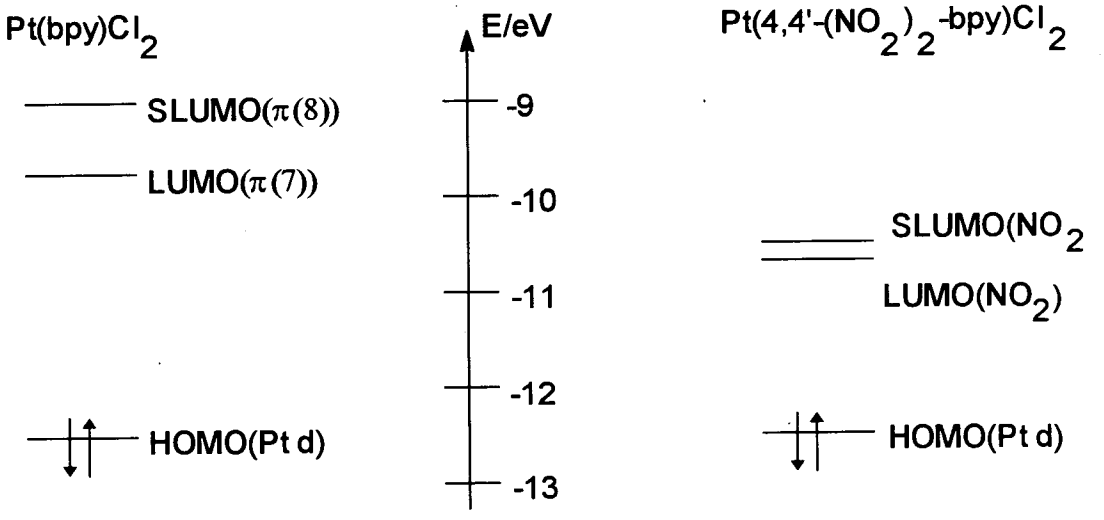

Figure 5.6 Energy level scheme for **I** and **XIII**

5.7 Epr Spectroelectrochemistry

The electroreduced monoanion **XIII**$^-$ gives solution and frozen glass epr spectra similar to others in the [Pt(4,4'-X_2-bpy)Cl_2] series (table 4.5, figure 5.7), *i.e.* interaction of the unpaired electron is only observed with the ^{195}Pt nucleus and not with ligand nuclei. An isotropic ^{195}Pt hyperfine coupling constant of A_{iso}=-43x10^{-4} cm^{-1} centered at g_{iso}=2.006 is observed in 0.1 M $TBABF_4$/DMF solution at room temperature. Rhombic g and ^{195}Pt hyperfine tensors are observed at 77 K with g_1=2.042, g_2=2.016, g_3=1.977, A_1=-33x10^{-4} cm^{-1} and A_2=-60x10^{-4} cm^{-1}. The hyperfine splitting of the high field g_3 component (A_3) is unresolved. A significantly smaller Pt $5d_{yz}$ orbital admixture of 7% to the SOMO is calculated from equation 1 using the parameters estimated directly from the epr spectrum. This can be explained by the strong π-accepting influence of the nitro groups.

On reduction to the dianionic **XIII**$^{2-}$ an epr spectrum is observed at room temperature and at 77 K. This confirms the two added electrons are unpaired, *i.e.* a spin-triplet state species is generated. The solution spectrum in DMF at room temperature exhibits both hyperfine coupling to ^{195}Pt and superhyperfine to ligand nuclei (figure 5.8a) centered at g_{iso}=2.018. This can be succesfully simulated by assuming coupling to ^{195}Pt (29.5 G (27.8x10^{-4} cm^{-1})), to two equivalent ^{14}N nuclei and to two equivalent ^{1}H nuclei (4.4 G (4.1x10^{-4} cm^{-1}) and 2.8 G (2.8x10^{-4} cm^{-1}) respectively) with a Lorentzian linewidth of 0.75 G (figure 5.8b). We assign the ^{14}N coupling to the nitro group nitrogens on the basis of the EHMO calculations, but do not attempt to assign the position of the ^{1}H nuclei. The EHMO calculations suggest that after the N2 and N2' superhyperfine coupling the next largest in magnitude should be to N1 and N1'. However, a better computer simulation of the experimental spectrum is possible using the model detailed above, *viz.*, coupling to two nitrogen nuclei and two hydrogen nuclei. Thus the EHMO calculations appear to be correct in the gross picture but inaccurate in the minor details.

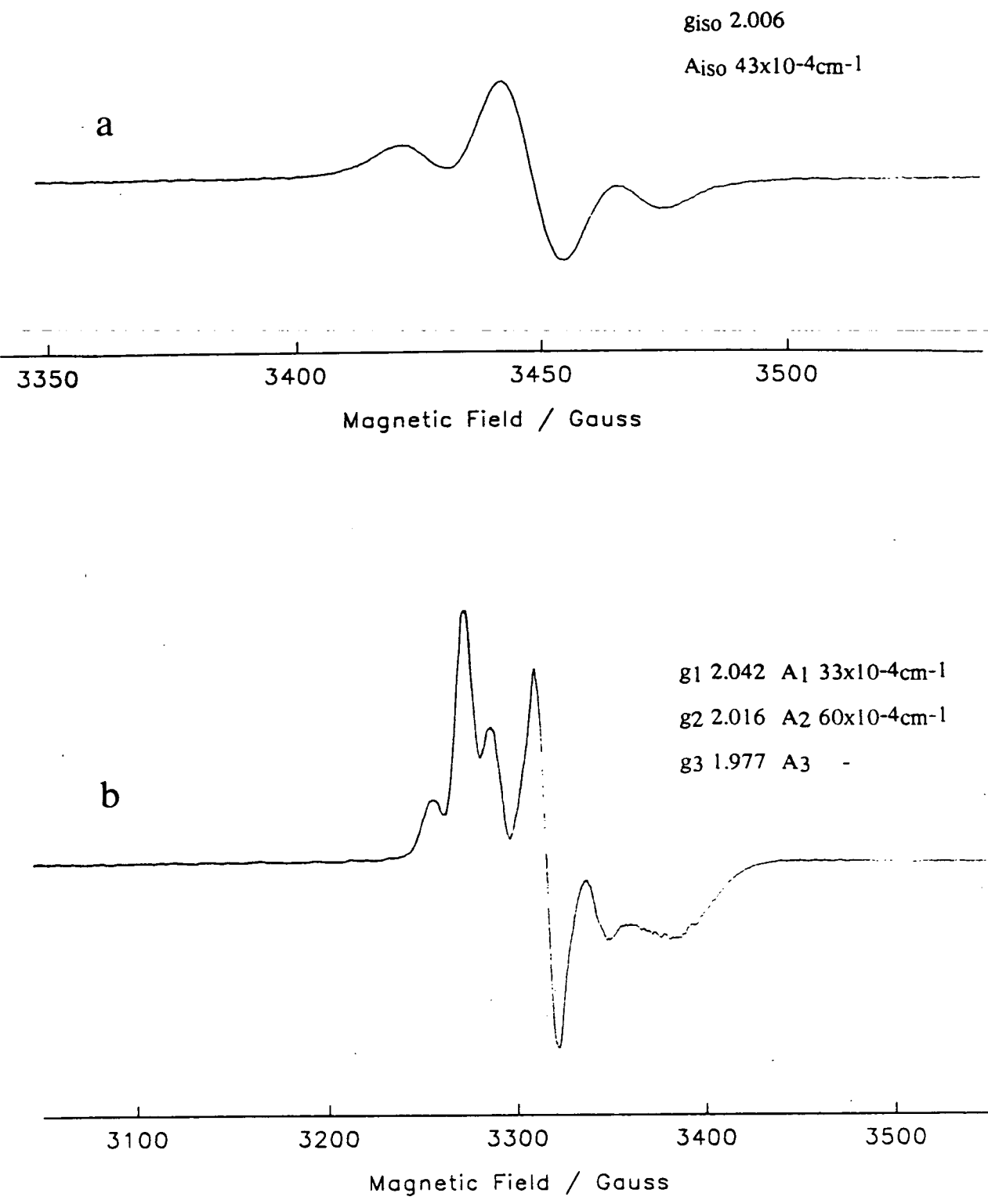

Figure 5.7 Solution (a) and frozen glass (b) epr spectra of **XIII** in 0.1 M $TBABF_4$/DMF

On cooling to 77 K a rhombic signal is observed (figure 5.9) but there are no resolvable hyperfine interactions. No features appear in the spectrum typical of a spin-triplet system, *i.e.* there is no observable electron-electron coupling fine structure. This can be indicative of a very small zero-field splitting compared to the microwave frequency.

The large difference in the linewidth of the solution spectra of **XIII**$^{-}$ (13.3 G) and **XIII**$^{2-}$ (0.75 G) may be due to an "electron hopping" mechanism. In the monoanion the unpaired electron can be thermally excited to the low-lying excited state (the SLUMO of the neutral molecule). This hopping between orbitals can contribute to line broadening in the observed epr spectrum. In the dianion the low-lying excited state is already occupied and hence this hopping mechanism cannot occur. De Armond *et al.* proposed this mechanism to explain the difference in the observed linewidths of the solution epr spectra of complexes such as $[Fe^{II}(bpy)_2(bpy^{-})]^{+}$ and $[Fe^{II}(bpy^{-})_3]^{-}$.[17] It would therefore be expected that the linewidth of **XIII**$^{-}$ would be temperature dependent while that of **XIII**$^{2-}$ would not. Unfortunately neither species exhibits any significant linewidth variation over the temperarure range 293 to 213 K in DMF solution. This may imply that the gap between the orbitals is too small for this process to be significantly retarded over the temperature range studied.

The tri- and tetra-anionic species proved to be too unstable on an electrosynthesis timescale to be studied further at any temperature.

The solution epr spectrum of **XIV**$^{-}$ at room temperature shows a broad single line at g_{iso}=2.010 (linewidth 10.7 G) with no observable ^{105}Pd hyperfine coupling (22% natural abundance, I=5/2). At 77 K the epr spectrum shows a broad asymmetric line with some observable structure on the high-field side (figure 5.10a). This may be coupling to ^{14}N rather than ^{105}Pd.

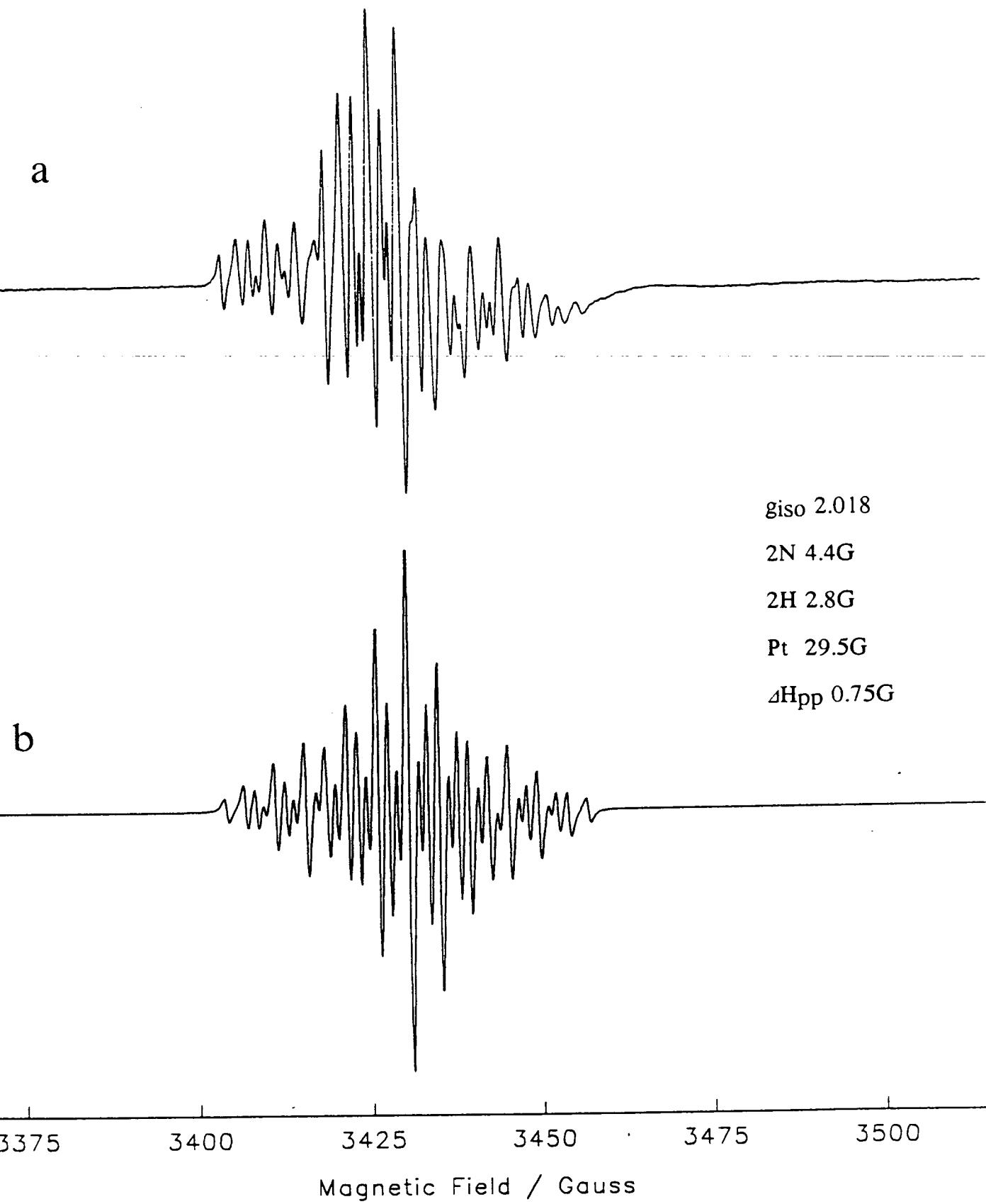

Figure 5.8 Solution epr spectrum of $XIII^{2-}$ in DMF at 293 K (a) and simulation (b)

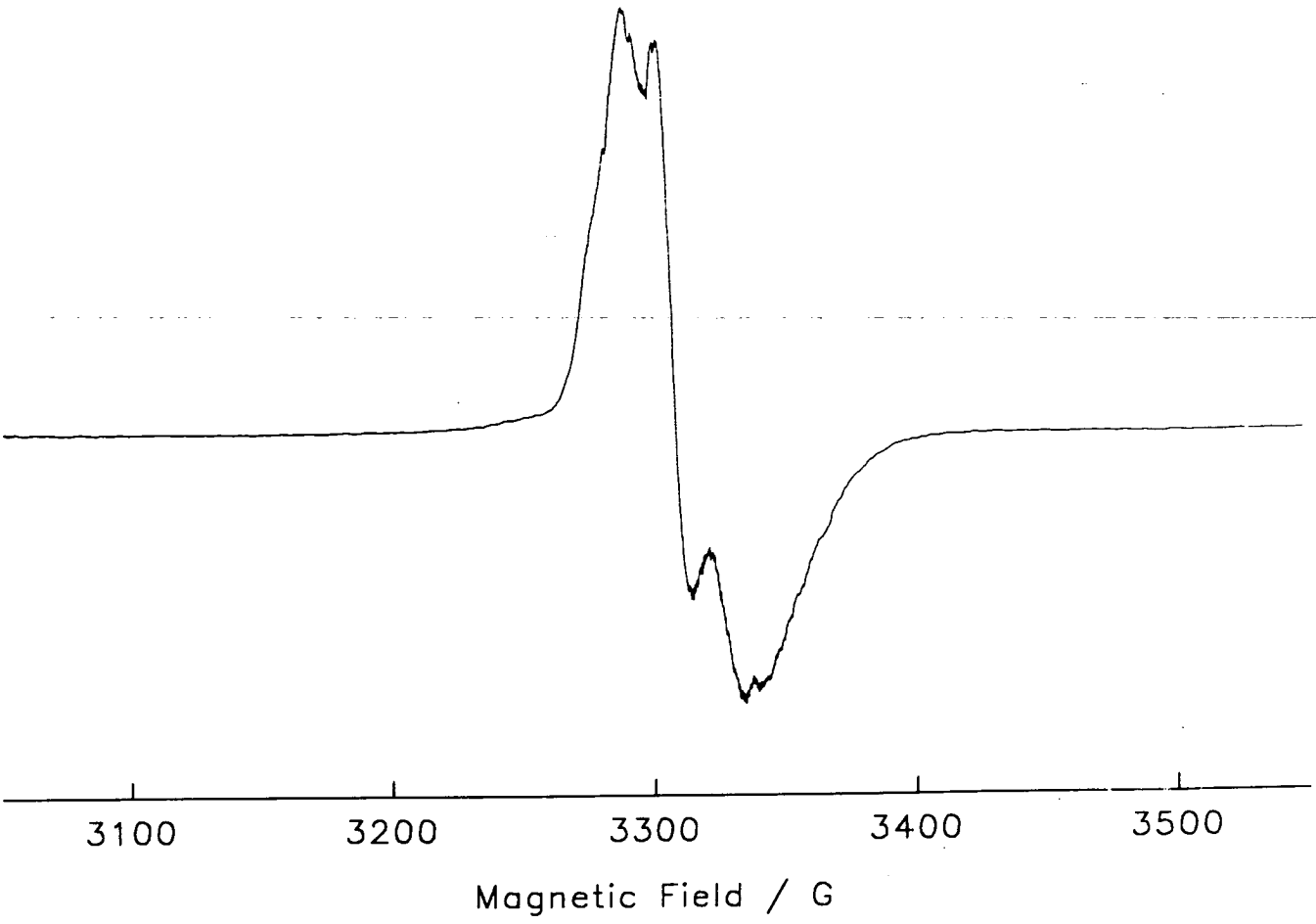

Figure 5.9 77 K epr spectrum of $\mathbf{XIII}^{2-}$ in 0.1 M $TBABF_4$/DMF

The solution epr spectrum of dianionic $\mathbf{XIV}^{2-}$ again shows a much smaller intrinsic linewidth (*ca.* 0.7 G) and superhyperfine coupling to ligand nuclei is observed (figure 5.11a) centered at g_{iso}=2.014. ^{105}Pd hyperfine coupling can be observed on both the high-field and low-field wings and is estimated to be in the order of 2-3 G. We have, as yet, been unable to simulate satisfactorily this spectrum. This may be due to slight dissociation of the complex on reduction releasing the reduced form of the ligand thereby complicating the spectrum. At 77 K a single featureless asymmetric line is observed (figure 5.11b).

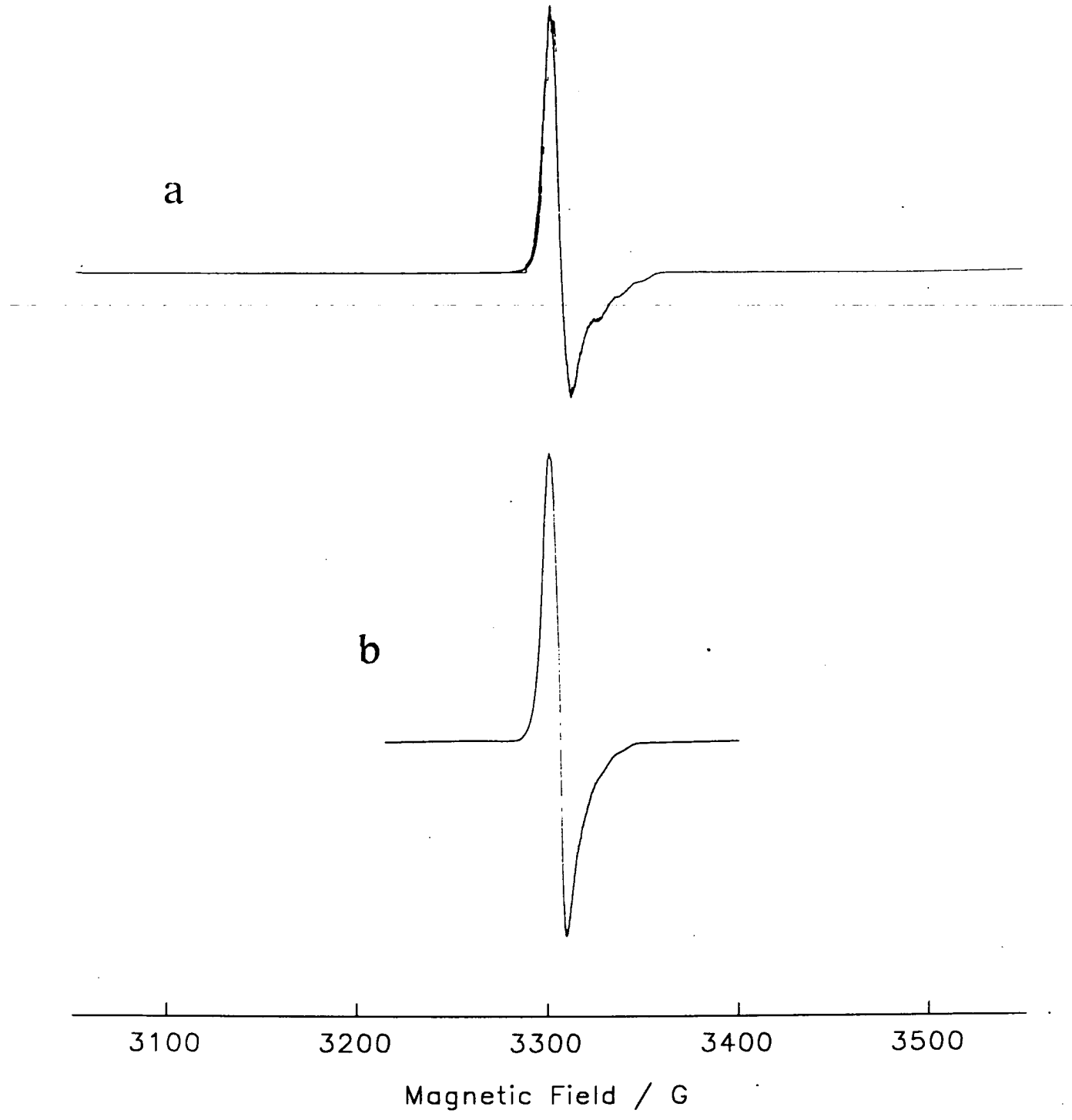

Figure 5.10 77 K epr spectra of **XIV**$^{-}$ in DMF (a) and **XV**$^{-}$ in CH_2Cl_2 (b)

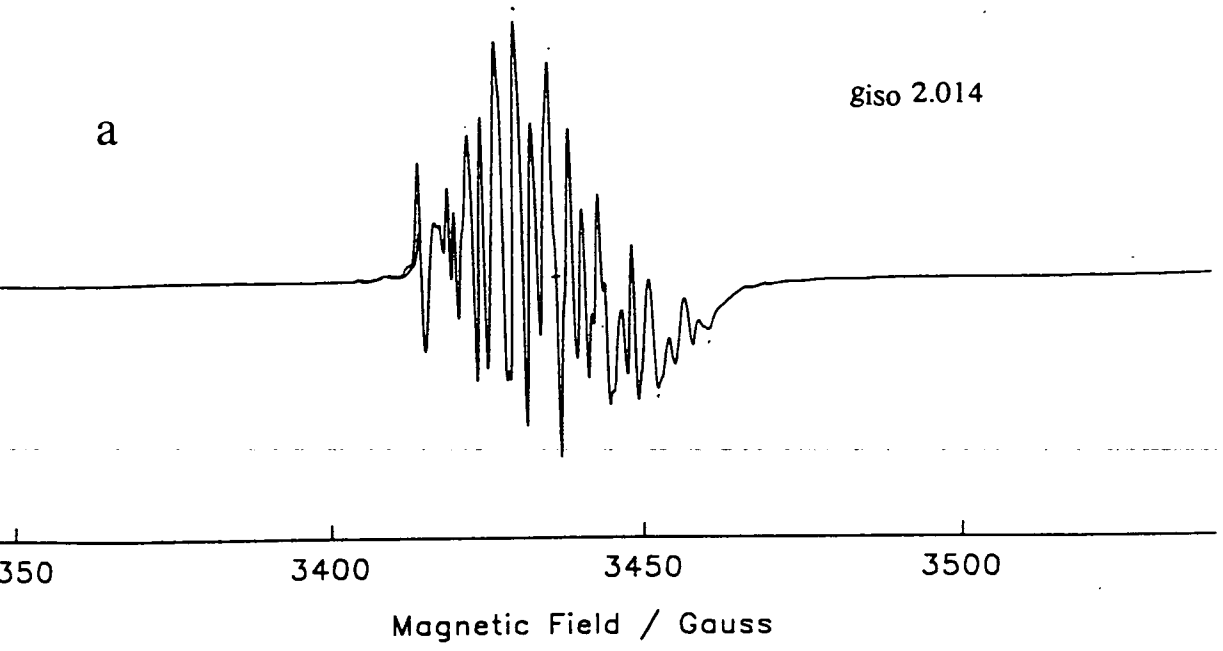

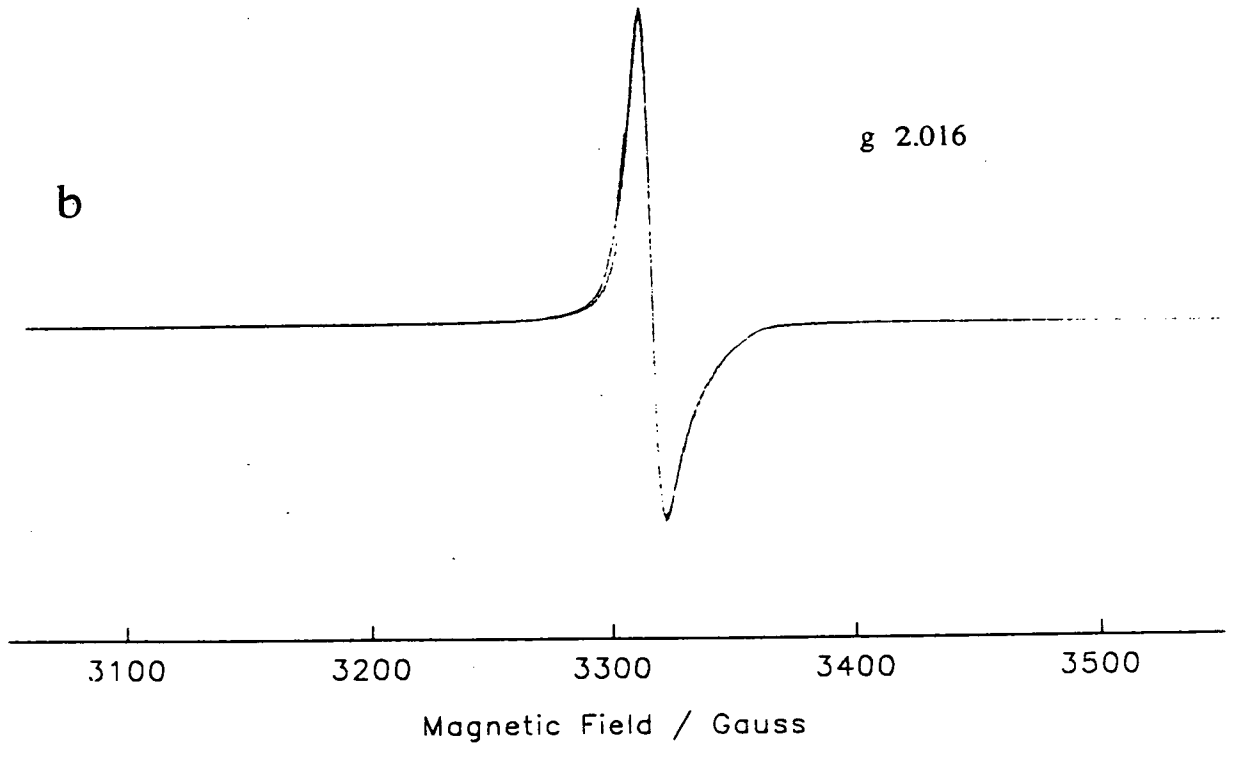

Figure 5.11 Solution(a) and frozen glass (b) epr spectra of XIV^{2-} in 0.1M $TBABF_4$/DMF

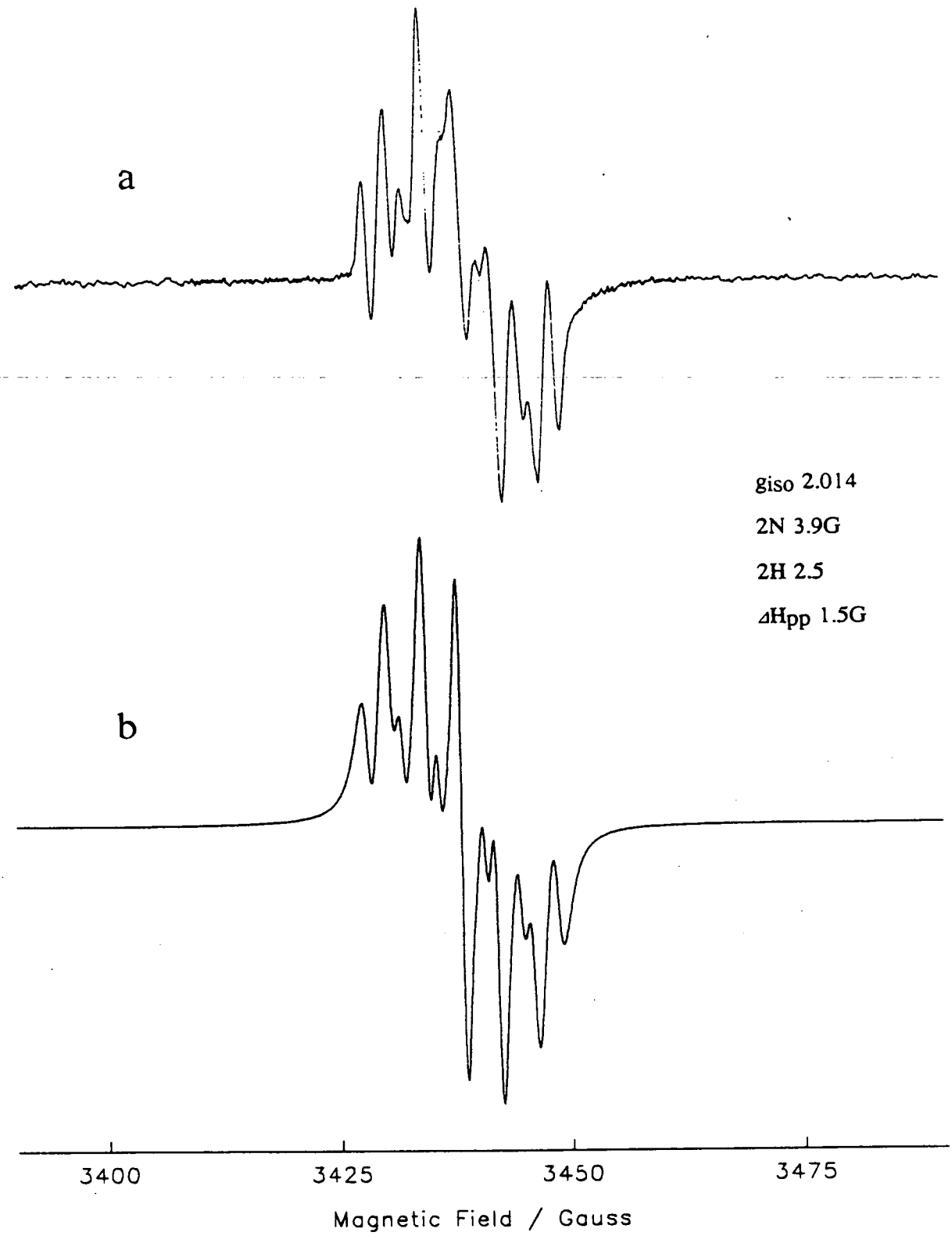

Figure 5.12 CH_2Cl_2 solution epr spectrum of $\mathbf{XV}^{2-}$ at 293 K (a) and simulation (b)

A similar pattern is observed for the mono- and di-reduced **XV**. The mono-reduced $\mathbf{XV}^-$ has g_{iso}=2.012 in 0.5 M $TBABF_4/CH_2Cl_2$ solution and shows a similar 77 K epr spectrum to $\mathbf{XIV}^-$ with the same high-field features. This supports the assignment of these as ^{14}N coupling rather than metal hyperfine (figure 5.10b). The solution epr spectrum of $\mathbf{XV}^{2-}$ shows superhyperfine coupling to ligand nuclei with g_{iso}=2.014 and can be simulated assuming coupling to two equivalent ^{14}N nuclei and two equivalent ^{1}H nuclei (3.9 G ($3.7x10^{-4}$ cm^{-1}) and 2.5 G ($2.4x10^{-4}$ cm^{-1}) respectively) with a Lorentzian linewidth of 1.5 G (figure 5.12a and b). No ^{103}Rh hyperfine coupling (100%, I=1/2) is observed and consequently must be smaller in magnitude than the observed linewidth. The model used to simulate this spectrum is similar to that used for $\mathbf{XIII}^{2-}$ (2N and 2H) and we assign the couplings accordingly.

Thus the epr spectra of the mono- and di-reduced forms of **XIII**, **XIV** and **XV** are entirely consistent with the observed redox chemistry and EHMO calculations, *viz.*, a very small LUMO-SLUMO gap with the orbitals mainly sited on the nitro groups.

5.8 Uv/Vis/Nir Spectroelectrochemistry

The uv/vis spectra of **XIII** and **XIV** in DMF solution are similar except for the presence of an MLCT band at 23000 cm^{-1} (ε=$0.45x10^4$ $M^{-1}cm^{-1}$) for **XIII** (5d-π^*). The analogous 4d-π^* MLCT transition for **XIV** would be expected at much higher energy. Higher energy bands appear at 29.5 and 32.7 kcm^{-1} for **XIII** and 29.6 and 32.1 kcm^{-1} for **XIV** (figures 5.13 a and b). These are probably a combination of internal ligand π–π^* and higher energy MLCT transitions. Both species are yellow in solution.

On reduction to $\mathbf{XIV}^-$ a broad band appears at low energy (*ca.* 7 kcm^{-1}) as well as two bands at 18.0 and 19.6 kcm^{-1} (figure 5.14b). The spectrum of $\mathbf{XIII}^-$ is more complicated than anticipated possibly due to the presence of residual **XIII** in solution (figure 5.14a).

On di-reduction the broad nir bands blue-shift for both species while the bands at *ca.* 20 kcm^{-1} intensify (figure 5.15). The major difference between the spectra of $\mathbf{XIII}^{2-}$ and $\mathbf{XIV}^{2-}$ is the presence of an intense peak at 23.1 kcm^{-1} for $\mathbf{XIII}^{2-}$ which is therefore assigned as the MLCT transition. We assign the broad nir bands and the visible bands as intra-ligand transitions. The mono-anionic species are both pale red, which darkens to a deep red on di-reduction.

5.9 Conclusions

The anomalous electrochemical behaviour of **XIII** can be fully explained in terms of a molecular orbital scheme with a low-lying LUMO and small LUMO-SLUMO gap where both orbitals are highly localised on the nitro groups. Thus di-reduction of **XIII** leads to the spin-triplet state species $\mathbf{XIII}^{2-}$. The energy of these ligand-based orbitals is little perturbed by changing the metal from Pt to Pd as witnessed by the identical redox potentials for the first two reduction processes in the cyclic voltammograms of **XIII** and **XIV**. Complex **XIV** has a ligand-based LUMO in contrast to $[Pd(bpy)Cl_2]$ which has a metal-based LUMO.

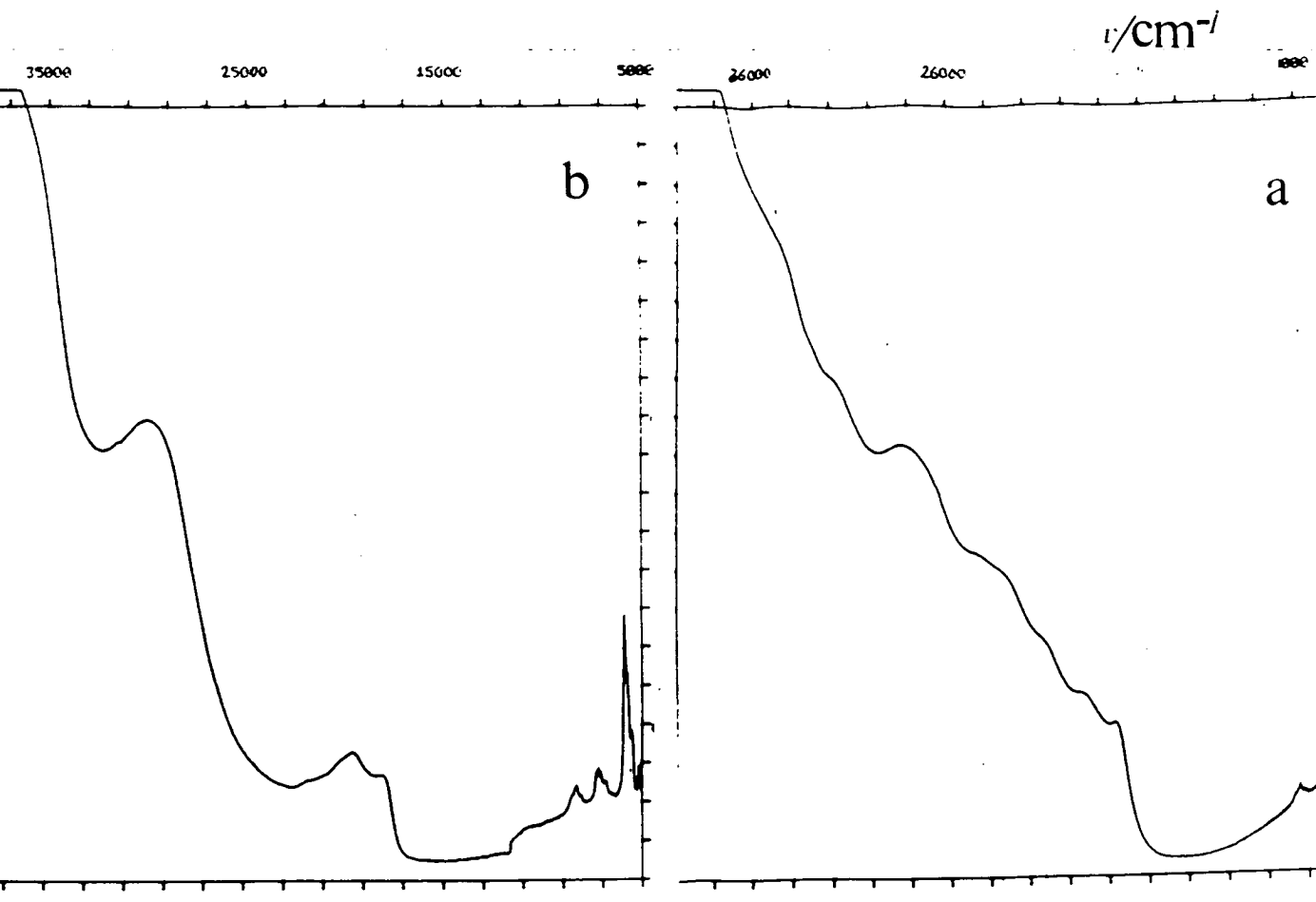

Figure 5.14 Uv/vis/nir spectra of **XIII**$^{+}$ (a) and **XIV**$^{-}$ (b) in 0.1M $TBABF_4$/DMF at 243 K

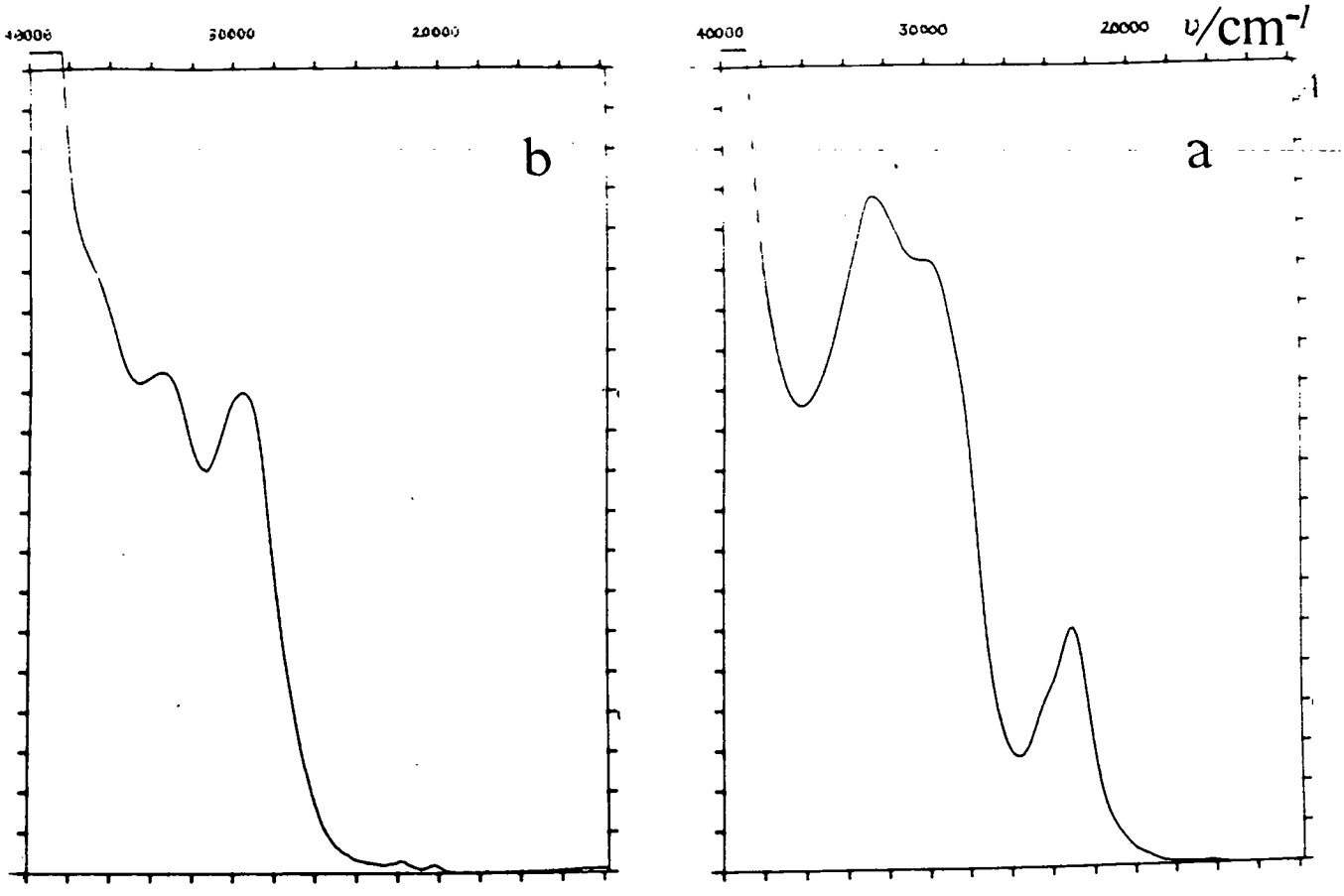

Figure 5.13 Uv/vis spectra of **XIII** (a) and **XIV** (b) in DMF solution at 293 K

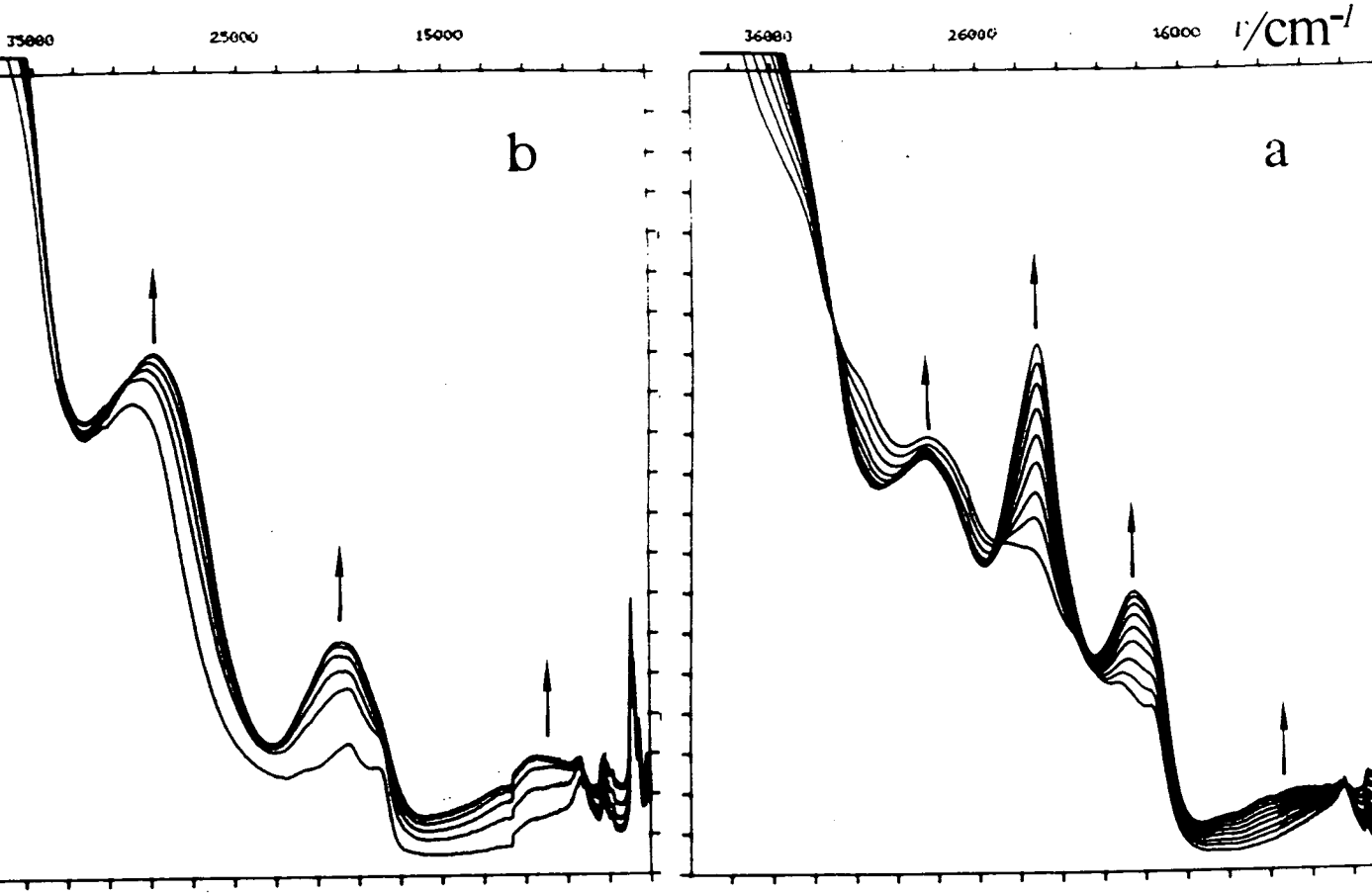

Figure 5.15 OTE reduction of $XIII^{-/2-}$ (a) and $XIV^{-/2-}$ (b) in 0.1M $TBABF_4$/DMF at 243K

Chapter 6. [Bis(2,2'-bipyridine)platinum(II)]$^{2+}$

6.1 Introduction

There have been a number of studies on transition metal bis-bipyridyl complexes due to their interesting structural[80-85] and electronic properties.[53,86-92] The bpy ligands on such systems are unable to adopt coplanar positions due to the steric repulsions between the 6 and 6' hydrogen atoms of the opposing bipyridyl ligands. Thus a distortion away from square planar is forced. This distortion can take two forms: (i) a "twist" deformation where the bpys retain their planarity but twist away from each other (*i.e.* a compressed tetrahedral geometry), or (ii) a "bow" distortion where the PtN_4 moiety remains planar but each bpy buckles (figure 6.1). For example $[Pt(bpy)_2](NO_3)_2$ adopts the twist form while $[Pt(bpy)_2](tcnq)_2$ (tcnq=7,7,8,8-tetracyanoquinodimethane) adopts the bow form in the solid state.[80,81] The solution geometry is not clear.

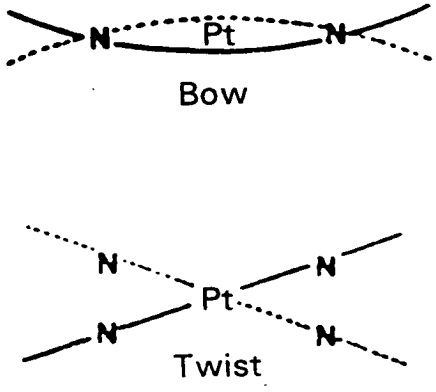

Figure 6.1 Distortions of the $[Pt(bpy)_2]^{2+}$ cation

The electrochemistry of both $[Rh(bpy)_2]^+$ and $[Pt(bpy)_2]^{2+}$ have been reported. $[Rh(bpy)_2]^+$, generated by the two electron reduction of $[Rh(bpy)_3]^{3+}$, undergoes two consecutive reversible one-electron reductions at -1.46 and -1.67 V *vs.* SCE in MeCN solution.[88] Căldăraru *et al.* reported the epr spectrum of the mono-reduced $[Rh(bpy)_2]^0$ as having a strong axially symmetric signal in the g=2 region and a weak, broad asymmetric signal in the g=4 region in an MeCN glass at 77 K.[89] They assign the former to the monomeric spin 1/2 species with the unpaired electron delocalised over the entire molecule, and the latter to a small concentration of a spin 1 dimeric species.

Two reports have appeared on the electrochemistry of $[Pt(bpy)_2]^{2+}$. The first describes an irreversible reduction at -0.97 V followed by two reversible reductions at -1.51 and -2.53 V *vs.* SCE in DMF solution.[90] The second reports the same irreversible reduction at -1.26 V followed by reversible reductions at -1.75 and -1.92 V *vs.* Ag/AgCl in the same solvent.[91] The first reduction was assigned as a metal-based process simply on the irreversibility of the reduction. However, the lowest energy excited state of $[Pt(bpy)_2]^{2+}$ has been assigned as ligand centered from its vibronically structured emission spectrum in a butyronitrile glass at 77 K.[53,92]

In this chapter we find both the previous reports on the redox chemistry of $[Pt(bpy)_2]^{2+}$ to be in error. We present strong evidence for a redox induced dimerisation process of this species and fully assign the cyclic voltammogram. We conclude the LUMO of this complex to be ligand-based.

6.2 Redox Chemistry and Spectroelectrochemistry

$[Pt(bpy)_2]^{2+}$ **(XVII)** is unique among the $[Pt(bpy)L_2]$ species discussed in chapter 3 in that it undergoes a completely irreversible one-electron (by coulometry) reduction at -0.60 V *vs.* Ag/AgCl in 0.1 M $TBABF_4$/DMF solution at room temperature (figure 6.2a, process a). Thus a rapid chemical reaction follows electron transfer. Bulk electrolysis at

-0.80 V affords an intense yellow species, "**XVII**", which exhibits an identical cyclic voltammogram to **XVII** minus the irreversible reduction at -0.60 V (figure 6.3). "**XVII**" is epr silent and hence the radical species formed by the one-electron reduction of **XVII** are combining to give a diamagnetic product, most likely a dimer (*vide infra*). Such redox-induced dimerisations have been observed for monomeric Pt(II) complexes such as $[Pt(RNC)_4]^{2+}$ and cis-$[Pt(RNC)_2Cl_2]$ (R=for example 2,4,6-Bu^t_3-C_6H_2).[93-95]

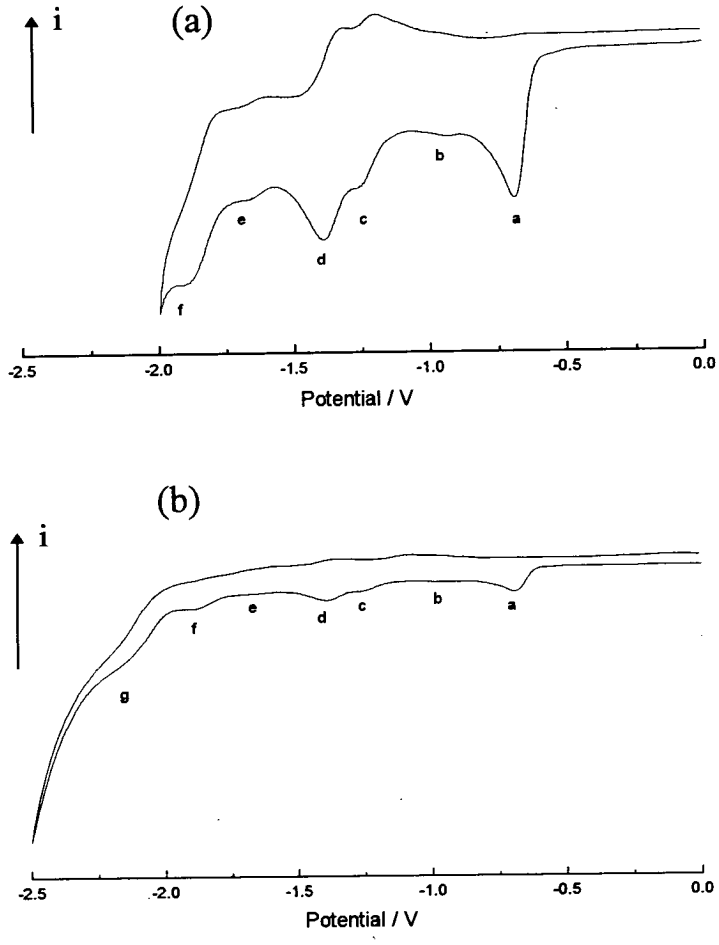

Figure 6.2 Cyclic voltammograms of **XVII** in 0.1 M $TBABF_4$/DMF at 293 K

The uv/vis spectral changes on reduction of **XVII** to "**XVII**" in 0.1 M $TBABF_4$/DMF solution involve the growth of an intense band at 35.8 kcm^{-1} which corresponds to the expected frequency for free bpy and the collapse of the coordinated bpy $\pi-\pi^*$ bands to approximately half their original intensity (figure 6.4). Thus the redox-induced reaction seems to involve coupling of the radical species and loss of bpy which would necessitate coordination of solvent at the vacant coordination site if four coordinate geometry at Pt is to be maintained. The loss of bpy is supported by a reduction process at *ca.* -2 V in the cyclic voltammogram of **XVII** (figure 6.2b, process g). Free bpy reduces at -2.05 V in DMF solution.

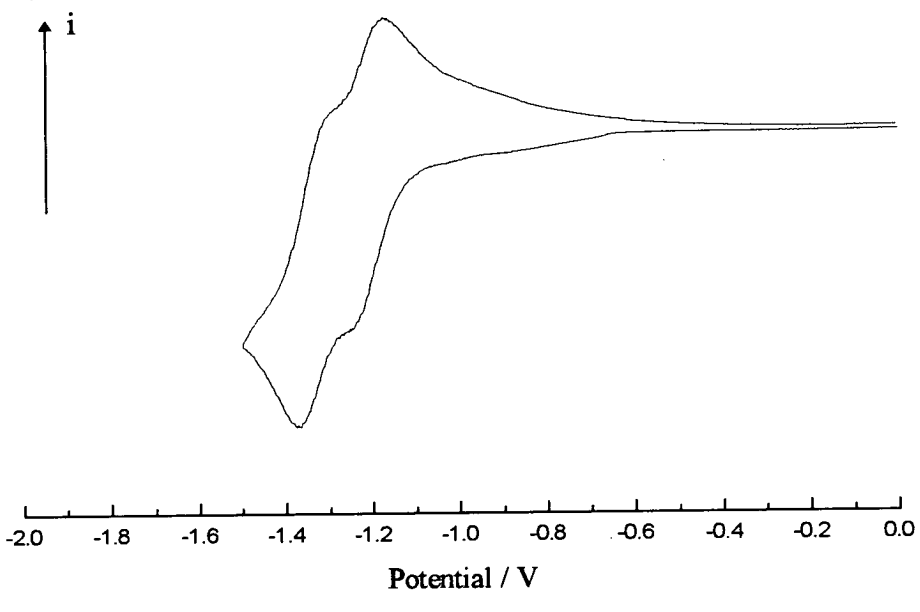

Figure 6.3 Cyclic voltammogram of "**XVII**" in 0.1 M $TBABF_4$/DMF at 293 K

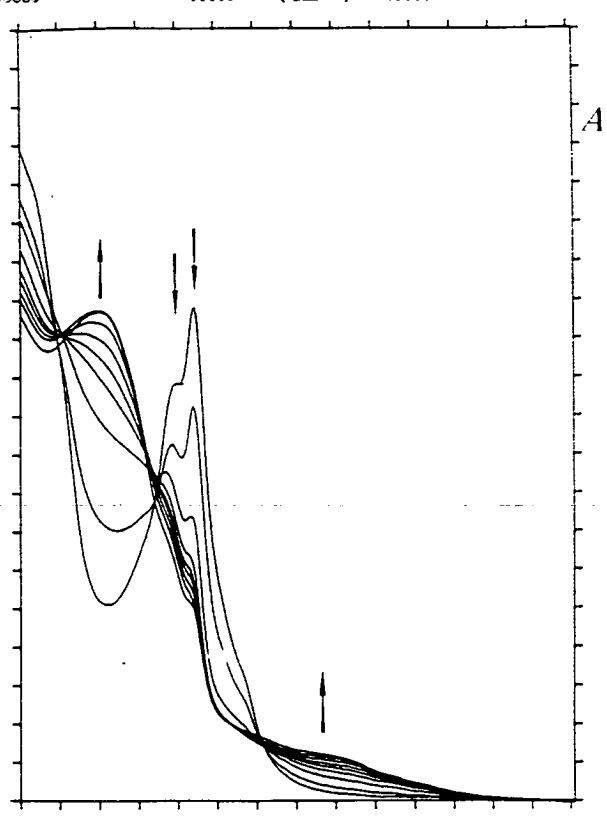

Figure 6.4 OTE reduction of **XVII** → "**XVII**" in 0.1 M $TBABF_4$/DMF at 293 K

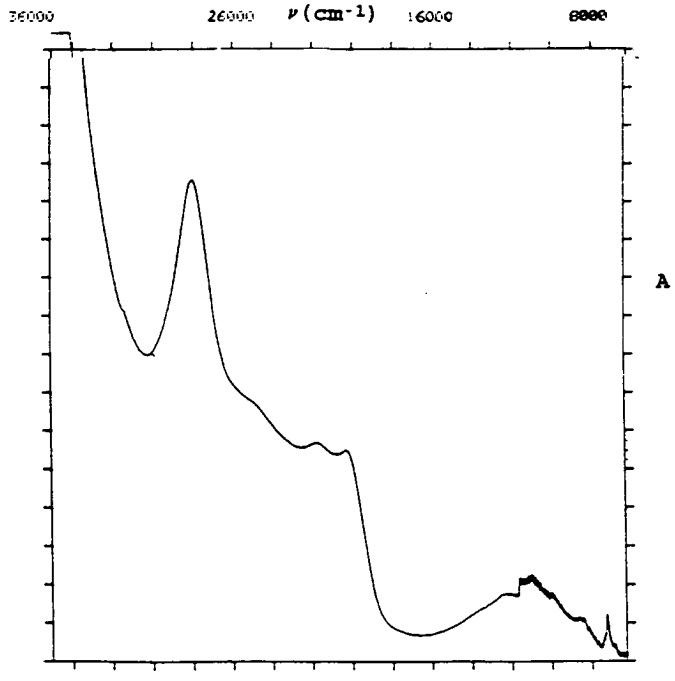

Figure 6.5 Uv/vis/nir spectrum of di-reduced dimeric species in 0.1 M $TBABF_4$/DMF

The "dimer" produced undergoes two consecutive reversible one-electron reductions at -1.15 and -1.26 V (figure 6.2a, processes c and d). Coulometric experiments show these two reductions to be a one-electron process in total with respect to the monomeric species. This supports the formation of a dimer. The uv/vis/nir spectrum of the dark green tri-reduced species generated at -1.40 V in 0.1 M $TBABF_4$/DMF solution has maxima at 11.0, 20.5, 22.0 and 28.0 kcm^{-1} all of which can be assigned as internal transitions of coordinated bpy^- (figure 6.5). The epr spectra of this species at 77 K and room temperature in DMF solution are consistent with this assignment (figure 6.6).

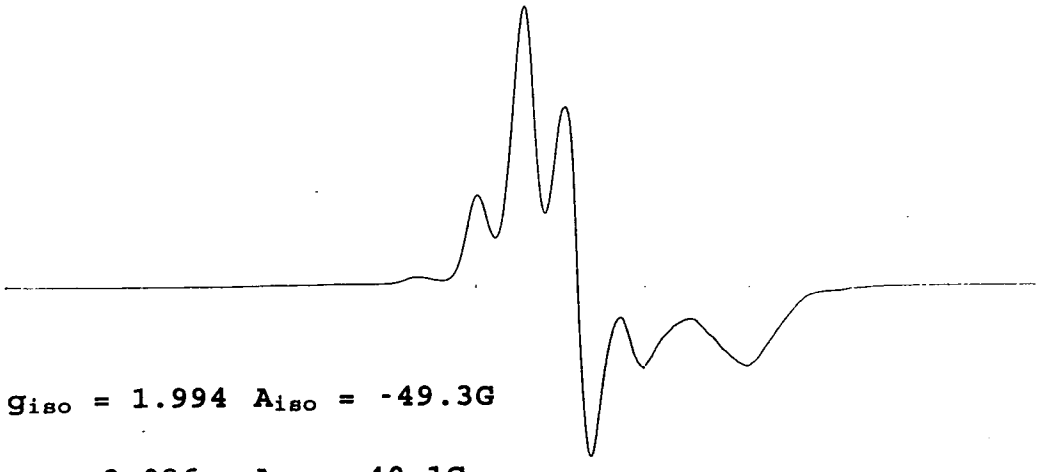

Figure 6.6 77K epr spectrum of di-reduced dimeric species in 0.1 M $TBABF_4$/DMF

The third reduction of the dimer is observed at -1.75 V, most likely the second reduction of one of the bpy ligands (figure 6.2, process f). The potential separation of 600 mV between processes c and f is consistent with this assignment. The proposed electrochemical scheme of **XVII** at room temperature is shown in scheme 6.1

$$[Pt(bpy)_2]^{2+} \overset{e^-}{\rightleftharpoons} [Pt(bpy)_2]^{+} \rightarrow [Pt(bpy)(S)]_2^{2+}$$

Scheme 6.1

At 213K the cyclic voltammogram of **XVII** shows four consecutive one-electron reductions at -0.65, -0.98, -1.56 and -1.95 V in 0.1 M $TBABF_4$/DMF solution (figure 6.7b). A return wave is now observed for the first reduction process (figure 6.7a), *i.e.* the chemical reaction following electron-transfer has been sufficiently slowed for the genuine mono-reduced **XVII** to be stable in solution on the cyclic voltammetric timescale. The observation of four reductions and the potential separations between the first and third and the second and fourth reductions (910 and 970 mV respectively) suggest that these processes are the stepwise reductions of the bpy ligands. The poor stability of the reduction products on an electrosynthesis timescale prevented spectroelectrochemical studies on these species.

The second and third reductions of the monomeric complex are seen in the cyclic voltammogram of **XVII** at room temperature as weak peaks (figure 6.2a, processes b and e).

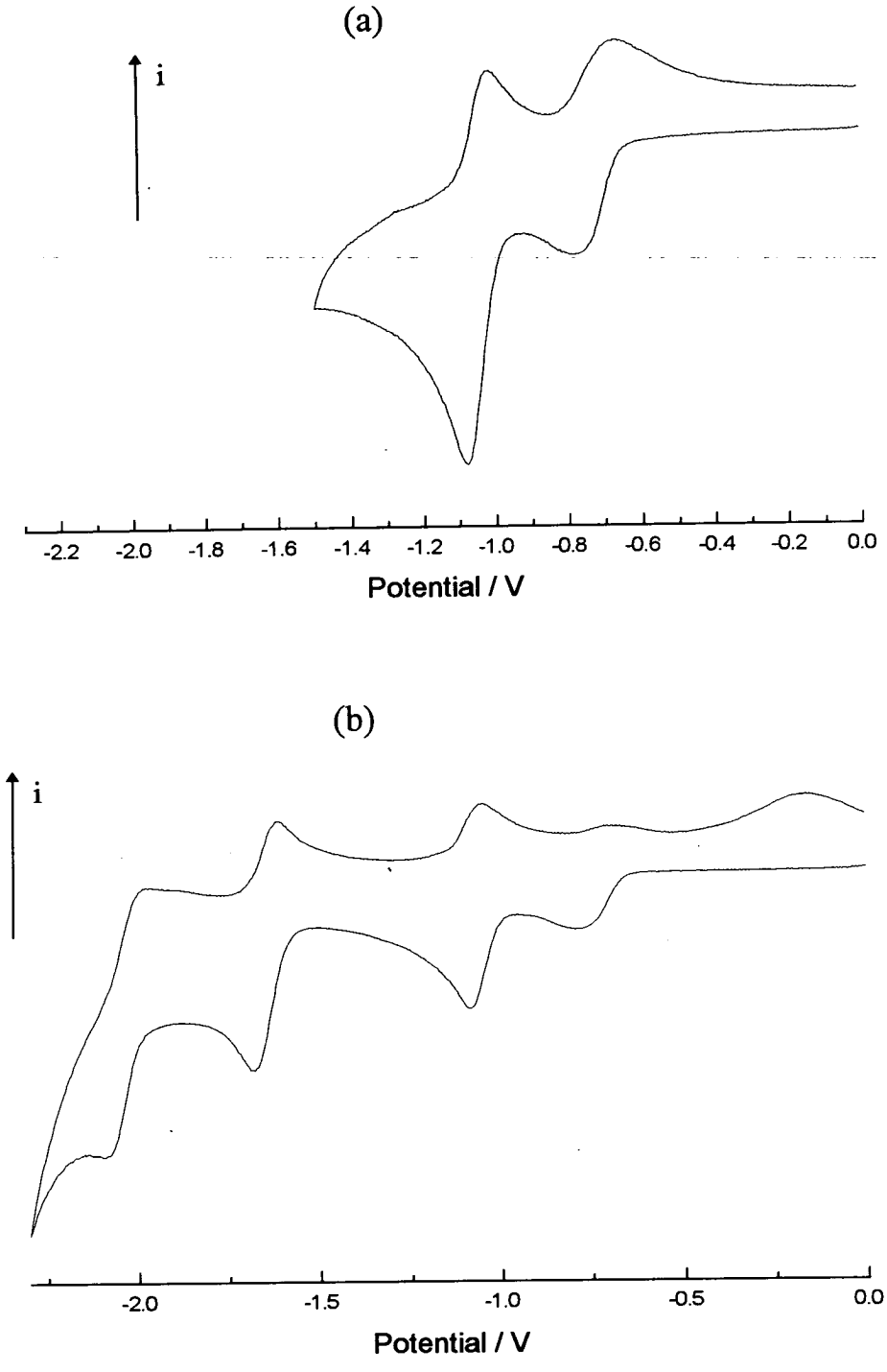

Figure 6.7 Cyclic voltammograms of **XVII** in 0.1 M $TBABF_4$/DMF at 213 K

Thus, the first reduction of **XVII** appears to be bpy based, similar to other $[Pt(bpy)L_2]$ species studied, yet it leads to a dimerisation reaction. This anomalous behavior may be due to the distorted nature of the ligand set. The bpy radical anion wants to be planar to allow maximum aromaticity of the π-system. Thus, on reduction of the bpy ligand the desire for the reduced bpy^- ligand to be planar may provide a strong driving force for the loss of bpy and the consequent coupling of the remaining fragments. At low temperatures this dissociation takes place much more slowly.

Preliminary dimerisation kinetic studies are in agreement with scheme 6.1. Repeating the study in the presence of free bpy inhibits the proposed dimerisation reaction. This indicates that dissociation of the reduced form of the monomeric complex to release free bpy is involved in the rate-determinig step.

6.3 Conclusions

$[Pt(bpy)_2]^{2+}$ undergoes a redox-induced dimerisation reaction on reduction at ambient temperatures, possibly to form $[Pt(bpy)S]_2^{2+}$ (S=solvent). The LUMO of $[Pt(bpy)_2]^{2+}$ is most likely ligand-based as shown by low-temperature cyclic voltammetry. The distorted nature of the ligand set may lead to the dissociation of the mono-reduced $[Pt(bpy)_2]^+$.

Conclusions and Discussion

Cyclic voltammetry, uv/vis/nir absorption and epr spectroscopies and EHMO calculations have been used to characterise the LUMO of $[Pt(bpy)L_2]$. While the results of the experiments are consistent with each other, each technique has its own merits and drawbacks. For example, while the uv/vis/nir spectra of $[Pt(bpy)L_2]^-$ grossly characterises the SOMO as a ligand-based π^* orbital, they offer no insight into the extent of ligand-metal orbital mixing. Epr spectroscopy affords a more explicit molecular orbital picture and a more sensitive probe to minor changes in the ligand set. For example, changing L from Cl^- to CN^- has little effect on the uv/vis/nir spectrum of $[Pt(bpy)L_2]^-$ but a significant effect on the epr spectrum. The main limitation of the epr experiment is the inability to determine metal p-orbital spin-densities. Work is in progress to address this problem by extending the relevant equations for d-orbital spin-density to include p-orbital admixtures and to estimate empirically the unknown parameters from high-level MO calculations.

It is perhaps surprising that the relatively low level EHMO calculations are in good agreement with the experimental results, giving MO schemes which are consistent with the observed redox-chemistry (for example, correctly predicting the relative size of the LUMO-SLUMO gap for **I** and **XIII**) and ligand-based redox-active orbitals. However, comparison of epr derived MO coefficients in the SOMO of $[Pt(bpy)L_2]^-$ and the theoretically calculated values reveal that the EHMO calculations consistently underplay the role of the metal orbitals. Equally, EHMO calculations often wrongly predict the distribution of electron-density about the bipyridyl rings as witnessed by the models required to simulate epr spectra where superhyperfine coupling to the ligand nuclei has been resolved.

There is great scope for work on the complexes of 4,4'-$(NO_2)_2$-bpy. Q-band epr spectra of **XIV**$^-$ and **XV**$^-$ would clarify the nature of the observed high-field features. It is unfortunate that there is no observable superhyperfine features in the solution epr spectrum of **XIII**$^-$ as this would give a clearer picture of the electronic distribution in the SOMO without the complication of a second unpaired electron. Electron nuclear double resonance (ENDOR) studies may resolve this problem. No electron-electron fine structure is observed in the epr spectra of the spin-triplet species **XIII**$^{2-}$, **XIV**$^{2-}$ and **XV**$^{2-}$. It may be that the zero-field splittings of these systems are too small to be observed at X-band frequencies and it is may be possible to resolve the fine structure at S-band frequencies.

More generally, it would be of interest to extend the study of strongly electron-withdrawing group substituted bipyridyls. For example, 4,4'-$(CN)_2$-bpy might be expected to show similar redox-behaviour to 4,4'-$(NO_2)_2$-bpy but has never been studied electrochemically either in the free or complexed form. Equally, the effect of the position of the substituents has never been systematically studied and deserves greater attention.

Appendix A. Structure of [Pt(4,4'-$(NO_2)_2$-bpy)Cl_2]

[Pt(4,4'-$(NO_2)_2$-bpy)Cl_2] dissolves to give yellow solutions yet exists as a red solid in the anhydrous form (see chapter 2). Thus, there must be some intermolecular interaction in the solid state to give rise to the different colour. This is revealed in the single-crystal structure determination. There are three distinct intermolecular interactions in the solid state:

(i) molecule pairs held together by bpyH...Cl hydrogen bonds (figure A.1) of 2.62 and 2.84 Å,

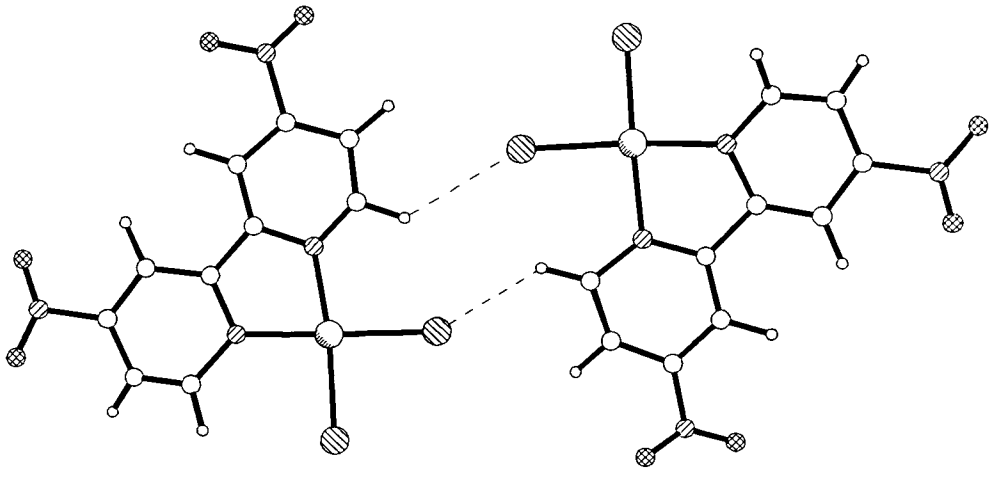

Figure A.1 Packing of [Pt(4,4'-$(NO_2)_2$-bpy)Cl_2]

(ii) a "diagonal" NOO...NO_2 interaction between the O atom of one nitro group and the N atom of a nitro group on a neighbouring molecule (figure A.2). This interaction is characterised by an O...N distance of 2.82 Å and is probably electrostatic in nature between the $N^{\delta+}$ and $O^{\delta-}$, and

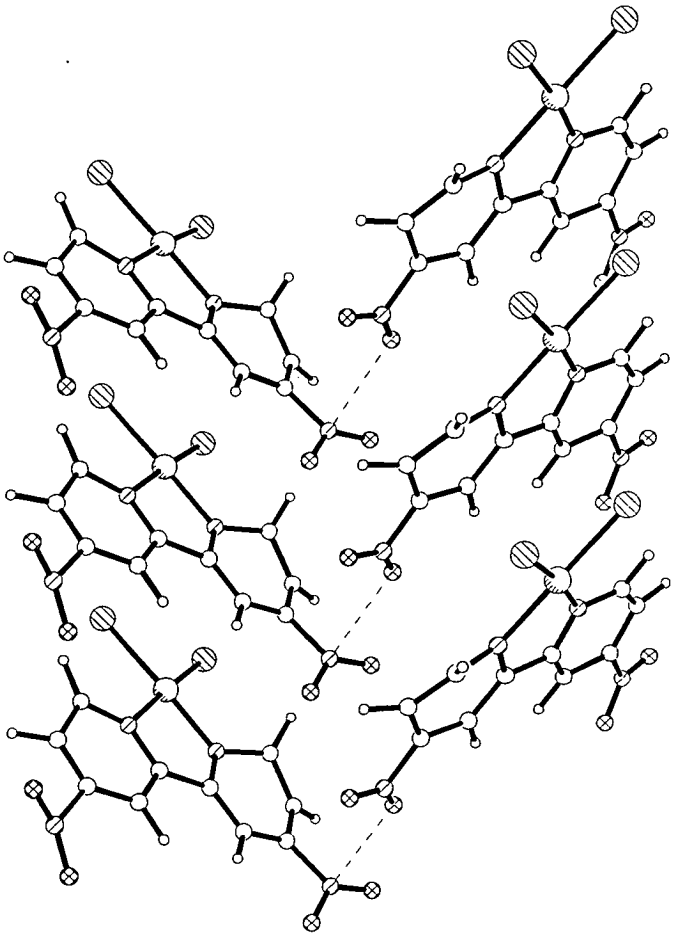

Figure A.2 Packing of [Pt(4,4'-$(NO_2)_2$-bpy)Cl_2]

(iii) hydrogen bonding between the O atoms of one molecule with the bipyridyl H atoms of neighbouring molecules (figure A.3) at O...H distances of 2.36 and 2.50 Å.

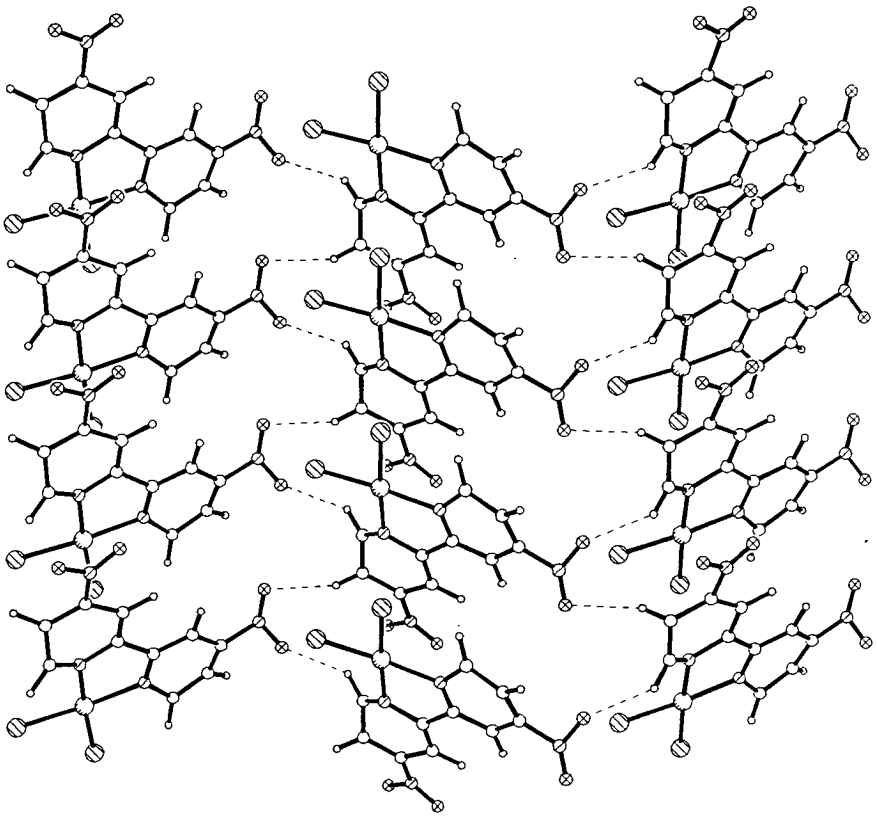

Figure A.3 Packing of [Pt(4,4'-$(NO_2)_2$-bpy)Cl_2]

There is no evident stacking of molecules as is observed for [Pt(bpy)Cl_2]. The separation of the adjacent molecules in the apparent molecular stacks in the *a* direction is

5.45 Å (*cf.* 3.45 Å in the red form of [Pt(bpy)Cl_2]),[44] the unit cell repeat distance, and is too large to be considered a genuine stacking interaction.

Table A.1 Fractional atomic co-ordinates for **XIII**

	x	y	z	Ueq
Pt(A)	-0.1522(3)	-0.41620(0)	-0.46809(6)	0.0341(10)
Pt(A2)	-0.3486(21)	-0.4080(7)	-0.4688(4)	0.041(4)
Cl(1A)	-0.4738(19)	-0.4124(8)	-0.4179(4)	0.056(6)
Cl(2A)	-0.262(3)	-0.5240(12)	-0.4877(8)	0.081(14)
N(1A)	-0.026(6)	-0.3196(16)	-0.4505(10)	0.039(8)
C(1A)	0.163(8)	-0.2989(21)	-0.4767(14)	0.049(10)
C(2A)	0.270(7)	-0.2345(24)	-0.4690(16)	0.050(15)
C(3A)	0.186(7)	-0.1927(20)	-0.4349(14)	0.044(10)
C(4A)	0.003(7)	-0.2197(20)	-0.4089(14)	0.048(10)
C(5A)	-0.141(10)	-0.278(3)	-0.4185(19)	0.084(18)
N(3A)	0.320(7)	-0.1298(19)	-0.4196(13)	0.050(9)
O(1A)	0.157(12)	-0.093(4)	-0.409(3)	0.18(3)
O(2A)	0.524(7)	-0.1190(20)	-0.4315(14)	0.085(12)
N(2A)	0.121(7)	-0.413(3)	-0.5093(15)	0.069(11)
C(6A)	0.256(7)	-0.3496(24)	-0.5109(17)	0.042(14)
C(7A)	0.440(8)	-0.3345(23)	-0.5391(14)	0.059(12)
C(8A)	0.505(9)	-0.3874(21)	-0.5679(16)	0.063(14)
C(9A)	0.380(7)	-0.4518(21)	-0.5680(15)	0.047(10)
C(10A)	0.144(13)	-0.451(5)	-0.549(3)	0.16(4)
N(4A)	0.696(10)	-0.371(3)	-0.6037(19)	0.105(20)
O(3A)	0.829(7)	-0.3264(23)	-0.5924(14)	0.082(12)
O(4A)	0.736(6)	-0.4118(21)	-0.6340(15)	0.071(10)
Pt(B)	-0.3377(4)	-0.73171(12)	-0.21651(7)	0.0379(12)
Pt(B2)	-0.148(3)	-0.7201(9)	-0.2153(6)	0.068(6)
Cl(1B)	-0.0268(20)	-0.7316(7)	-0.1655(4)	0.060(7)
Cl(2B)	-0.2228(22)	-0.6216(8)	-0.2377(7)	0.056(9)
N(1B)	-0.608(5)	-0.7349(15)	-0.2607(9)	0.032(7)
C(1B)	-0.749(6)	-0.7954(21)	-0.2573(15)	0.031(12)
C(2B)	-0.946(7)	-0.8053(20)	-0.2855(13)	0.047(10)
C(3B)	-1.004(7)	-0.7552(18)	-0.3187(13)	0.046(11)
C(4B)	-0.854(8)	-0.6966(24)	-0.3250(16)	0.066(13)
C(5B)	-0.710(7)	-0.6816(21)	-0.2893(14)	0.046(10)
N(3B)	-1.219(6)	-0.7663(16)	-0.3470(12)	0.039(9)
O(1B)	-1.240(5)	-0.7169(17)	-0.3697(12)	0.054(9)
O(2B)	-1.313(7)	-0.8196(20)	-0.3431(14)	0.077(11)
N(2B)	-0.468(6)	-0.8230(16)	-0.2030(11)	0.040(8)
C(6B)	-0.673(7)	-0.8439(21)	-0.2235(14)	0.048(10)
C(7B)	-0.783(6)	-0.9067(21)	-0.2157(13)	0.036(11)
C(8B)	-0.690(7)	-0.9455(21)	-0.1804(14)	0.043(10)
C(9B)	-0.476(7)	-0.9294(19)	-0.1591(14)	0.051(11)
C(10B)	-0.395(7)	-0.8656(20)	-0.1702(14)	0.051(11)
N(4B)	-0.821(9)	-1.0144(23)	-0.1714(18)	0.086(16)
O(3B)	-1.026(7)	-1.0193(16)	-0.1852(11)	0.061(9)
O(4B)	-0.730(4)	-1.0548(14)	-0.1493(10)	0.039(6)

H(2A)	0.4189	-0.2171	-0.4896	0.0600
H(4A)	-0.0331	-0.1934	-0.3778	0.0600
H(5A)	-0.3165	-0.2888	-0.4036	0.0600
H(7A)	0.5317	-0.2848	-0.5392	0.0600
H(9A)	0.4600	-0.4985	-0.5817	0.0600
H(10A)	-0.0081	-0.4776	-0.5639	0.0600
H(2B)	-1.0558	-0.8516	-0.2823	0.0600
H(4B)	-0.8541	-0.6665	-0.3552	0.0600
H(5B)	-0.6708	-0.6278	-0.2822	0.0600
H(7B)	-0.9337	-0.9250	-0.2357	0.0600
H(9B)	-0.3844	-0.9637	-0.1362	0.0600
H(10B)	-0.2489	-0.8458	-0.1497	0.0600

	U11	U22	U33	U23	U13	U12
Pt(A)	033(1)	034(1)	035(1)	006(1)	-006(1)	-012(1)
Cl(1A)	049(6)	065(6)	054(6)	007(7)	009(5)	-010(7)
Cl(2A)	079(11)	087(15)	077(15)	014(12)	003(8)	-030(8)
Pt(B)	040(1)	037(1)	037(1)	-005(1)	005(1)	000(1)
Cl(1B)	048(6)	068(7)	065(7)	-007(8)	001(5)	001(7)
Cl(2B)	059(7)	042(8)	066(12)	016(8)	-004(6)	-019(5)

Appendix B. Structure of 2,2'-bipyridinedichlorogold(III) tetrafluoroborate

$[Au(bpy)Cl_2]BF_4$ was prepared by a modification of the method of Harris and Lockyer.[96] An aqueous solution of bpy (4.2 mmol in 10 ml) was heated to reflux and an aqueous solution of $Na[AuCl_4]$ (2 mmol in 10 ml) added to yield an orange solution. Dropwise addition of excess $HBF_{4(aq)}$ with stirring precipitated crystals of the target species. Recrystallisation from MeOH afforded $[Au(bpy)Cl_2]BF_4$ as well-formed yellow needles in *ca.* 90% yield. C:H:N 23.53%:1.64%:5.47% (required 23.51%:1.58%:5.48%). Uv/vis (MeCN): ν_{max} 31970 cm^{-1} (ε 1.28×10^4 $M^{-1}cm^{-1}$). $[Au(bpy)Cl_2]BF_4$ undergoes a chemically irreversible two-electron (by coulometry) reduction at +0.52 V in 0.1 M $TBABF_4$/DMF solution at 293 K. Bulk electroreduction at +0.2 V results in decolourisation of the working solution and dissociation of the complex to generate free bpy, consistent with the formation of a linear d^{10} species.

Crystal Data

$C_{10}H_8AuBCl_2F_4N_2$

$M_r = 510.83$

Monoclinic

$P2_1/n$

$a = 6.850(4)$ Å

$b = 12.852(5)$ Å

$c = 15.537(5)$ Å

$\beta = 96.33(4)°$

$V = 1359.5(10)$ Å^3

$Z = 4$

$F(000) = 944$

$D_x = 2.495$ Mg m^{-3}

Mo K_α radiation

$\lambda = 0.71073$ Å

Cell parameters from 25 reflections

$\theta = 12\text{-}13°$

$\mu = 11.23$ mm^{-1}

T = 291 K

Needle

0.3 x 0.07 x 0.07 cm

Yellow

Data Collection

Enraf-Nonius CAD4 diffractometer

ω-2θ scans

Empirical absorption correction;[40] min and max absorption corrections 0.79 and 1.67

2599 measured reflections

2381 independent reflections

2041 observed reflections [$F>2.0\sigma(F)$]

$R_{int} = 0.048$

$\theta_{max} = 25°$

$h = -8 \rightarrow 8$

$k = 0 \rightarrow 15$

$l = 0 \rightarrow 18$

2 standard reflections monitored every 500 reflections; no intensity decay

Refinement

Refinement on F

$R = 0.0437$

$wR = 0.0592$

$S = 1.284$

2041 reflections

162 parameters

H atoms not positionally refined

$U_H = 0.090(16)$ Å^2

$w = 1/[\sigma^2(F) + 0.000804F^2]$

$(\Delta/\sigma)_{max} = 0.002$

$\Delta\rho_{max} = 2.34$ eÅ^{-3} [near F(3) and F(4)]

$\Delta\rho_{min} = -1.34$ eÅ^{-3}

Atomic scattering factors from *Internetional Tables*[36] and SHELX76[37]

Bipyridine H atoms were set in idealised positions and allowed to ride on their respective carbon atoms, with C-H = 1.08 Å. Au, C, Cl, N and B atoms were refined with anisotropic displacement parameters whilst F atoms were refined isotropically. A single (isotropic) thermal parameter for all H atoms was refined. Structure solution (Patterson

and difference Fourier syntheses) and refinement *via* SHELX76.[37] Molecular geometry calculations *via* CALC.[38]

Table B.1 lists the atomic co-ordinates of $[Au(bpy)Cl_2]BF_4$. A view of the cation in a direction perpendicular to its approximate molecular plane is given in figure B.1. Table B.2 lists interatomic distances and interbond angles. The $\{AuN_2Cl_2\}$ fragment of the cation is approximately planar (maximum atomic deviation from the least-squares plane < 0.05 Å) and the cation as a whole has near C_{2v} local symmetry. Whilst the ring of N(1') is essentially located in this plane (maximum deviation 0.24 Å, C(5')) all the atoms in the N(1) ring lie to one side of the metal co-ordination plan, with C(3) and C(4) exhibiting the maximum elevation (0.38 Å). It may be of relevance that H(5) is involved in H-bonding to F(2), characterised by CH...F 2.18 Å, C-H...F 167° and H...F-B 141°.

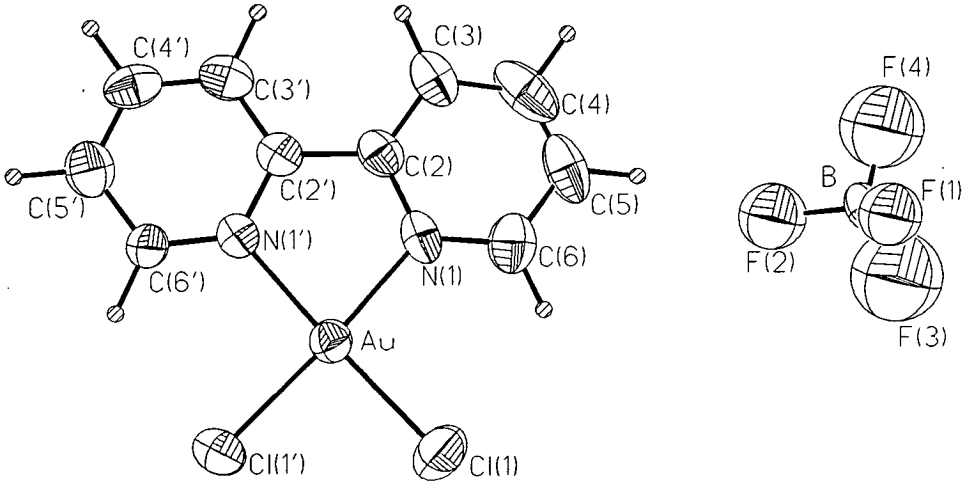

Figure B.1 Structure of $[Au(bpy)Cl_2]BF_4$

As far as we are aware, this represents only the second gold(III) bpy species to be crystallographically characterised. Au-N(1) and Au-N(1') are not significantly different from one another, average 2.037(13) Å, but do vary significantly from the average value in $[Au(bpy)(mes)_2]^+$ (mes=$C_6H_2Me_3$-2,4,6), 2.125(6) Å.[97] This presumably arises from the differing *trans* influences of Cl and mes. The Au-Cl distances in $[Au(bpy)Cl_2]^+$ are identical, 2.252(4) Å, and the C(2)-C(2') bridge distance is 1.457(15) Å.

In the crystal the closest approach of cations is 6.850 Å, *i.e.* the unit cell repeat in the *a* direction. Clearly this distance does not represent a significant interaction, *c.f.* 3.45 Å and 4.43 Å in the red and yellow forms, respectively, of $[Pt(bpy)Cl_2]$.[43,44]

Table B.1 Fractional atomic co-ordinates and equivalent isotropic displacement parameters ($Å^2$) for $[Au(bpy)Cl_2]BF_4$

	x	y	z	Ueq
Au	0.62915(6)	0.37873(3)	0.80294(2)	0.0423(3
Cl(1′)	0.4107(5)	0.3801(3)	0.90114(20)	0.0665(19
Cl(1)	0.8221(6)	0.4842(3)	0.89136(22)	0.0777(23
N(1)	0.8029(14)	0.3785(7)	0.7053(6)	0.048(5)
N(1′)	0.4660(12)	0.2821(6)	0.7186(5)	0.038(4)
C(6′)	0.3120(16)	0.2297(9)	0.7370(7)	0.047(6)
C(2′)	0.5391(14)	0.2727(8)	0.6421(6)	0.040(5)
C(3′)	0.4421(18)	0.2107(9)	0.5776(7)	0.053(7)
C(4)	0.9914(22)	0.3819(13)	0.5625(10)	0.081(10)
C(3)	0.8157(18)	0.3297(10)	0.5585(8)	0.058(7)
C(5′)	0.2104(20)	0.1642(10)	0.6745(8)	0.061(8)
C(6)	0.9707(19)	0.4311(11)	0.7034(9)	0.065(8)
C(4′)	0.2813(19)	0.1561(9)	0.5954(7)	0.055(7)
C(2)	0.7200(16)	0.3287(9)	0.6318(7)	0.047(6)
C(5)	1.0706(20)	0.4315(12)	0.6308(11)	0.074(9)
F(1)	1.4949(12)	0.7176(7)	0.6230(5)	0.0833(23
F(2)	1.4932(15)	0.5480(9)	0.6609(6)	0.106(3)
B	1.6011(18)	0.6305(10)	0.6359(8)	0.046(7)
F(3)	1.737(3)	0.6398(13)	0.7064(12)	0.200(7)
F(4)	1.6589(24)	0.5979(11)	0.5620(11)	0.165(6)

Table B.2 Interatomic distances (Å) and interbond angles (°) for $[Au(bpy)Cl_2]BF_4$

Au	-Cl(1′)	2.252(4)	C(3′)	-C(4′)	1.360(16)
Au	-Cl(1)	2.252(4)	C(4)	- C(3)	1.374(20)
Au	- N(1)	2.028(10)	C(4)	- C(5)	1.304(22)
Au	-N(1′)	2.046(8)	C(3)	- C(2)	1.374(17)
N(1)	- C(6)	1.337(17)	C(5′)	-C(4′)	1.375(17)
N(1)	- C(2)	1.377(14)	C(6)	- C(5)	1.381(21)
N(1′)	-C(6′)	1.309(14)	F(1)	- B	1.337(15)
N(1′)	-C(2′)	1.345(13)	F(2)	- B	1.373(16)
C(6′)	-C(5′)	1.410(17)	B	- F(3)	1.362(23)
C(2′)	-C(3′)	1.391(15)	B	- F(4)	1.322(20)
C(2′)	- C(2)	1.457(15)			

Cl(1′)	- Au	-Cl(1)	88.35(13)	C(2′)	-C(3′)	-C(4′)	118.8(10)
Cl(1′)	- Au	- N(1)	174.3(3)	C(3)	- C(4)	- C(5)	124.0(15)
Cl(1′)	- Au	-N(1′)	94.70(24)	C(4)	- C(3)	- C(2)	117.6(12)
Cl(1)	- Au	- N(1)	95.9(3)	C(6′)	-C(5′)	-C(4′)	117.7(11)
Cl(1)	- Au	-N(1′)	176.91(24)	N(1)	- C(6)	- C(5)	121.7(13)
N(1)	- Au	-N(1′)	81.1(4)	C(3′)	-C(4′)	-C(5′)	121.1(11)
Au	- N(1)	- C(6)	126.4(9)	N(1)	- C(2)	-C(2′)	114.6(9)
Au	- N(1)	- C(2)	113.5(7)	N(1)	- C(2)	- C(3)	119.5(10)
C(6)	- N(1)	- C(2)	119.5(10)	C(2′)	- C(2)	- C(3)	125.8(10)
Au	-N(1′)	-C(6′)	124.6(7)	C(4)	- C(5)	- C(6)	117.6(14)
Au	-N(1′)	-C(2′)	112.9(6)	F(1)	- B	- F(2)	112.8(11)
C(6′)	-N(1′)	-C(2′)	122.4(9)	F(1)	- B	- F(3)	111.0(13)
N(1′)	-C(6′)	-C(5′)	120.3(10)	F(1)	- B	- F(4)	110.2(12)
N(1′)	-C(2′)	-C(3′)	119.6(9)	F(2)	- B	- F(3)	100.4(12)
N(1′)	-C(2′)	- C(2)	117.2(9)	F(2)	- B	- F(4)	102.9(12)
C(3′)	-C(2′)	- C(2)	123.2(9)	F(3)	- B	- F(4)	118.9(14)

Acknowledgements

First and foremost I would like to thank Dr. Lesley J. Yellowlees for all her help and advice over the last three years.

Many thanks also to Prof. Alan J. Welch (Heriot Watt University) for help with *X*-ray crystallographic studies and EHMO calculations and Drs. Frank E. Mabbs, David Collison and Kenneth J. Taylor (University of Manchester) for computer simulations of anisotropic epr spectra and the Q-band epr spectrum of $[Pt(bpy)(CN)_2]^-$. I am grateful to all the above and to Dr. Richard E. P. Winpenny and Dr. Jeremy M. Rawson (Durham University) for many helpful discussions.

Thanks also to Lorna Eades (CHN microanalyses), Stuart Mains (technical services) and Christina Mandolini and Lorenzo Rovatti (some synthetic work in Chapter 4).

I am grateful to the Edith and Isaac Wolfson (Scotland) Trust for financial support and to the University of Edinburgh.

Last, but not least, thanks to all those who have worked in labs. 291 and 292 over the years.

References

1. E.C. Constable, *Adv. Inorg. Chem.* 1989, **34**, 1.

2. F.A. Cotton and G. Wilkinson, Advanced Inorganic Chemistry; John Wiley and Sons; New York, 1988.

3. A.H. Maki, N. Edelstein, A. Davidson and R.H. Holm, *J. Am. Chem. Soc.* 1964, **86** (4), 4580.

4. E. Billig, S.I. Shupack, J.H. Walters, R. Williams and H.B. Gray, *J. Am. Chem. Soc.* 1964, **86** (1), 927.

5. R.L. Schlupp and A.H. Maki, *Inorg. Chem.* 1974, **13** (1), 44.

6. W.E. Geiger, Jr., C.S. Allen, T.E. Mines and F.C. Senftleber, *Inorg. Chem.* 1977, **16** (8), 1474.

7. F.C. Senftleber and W.E. Geiger, Jr., *Inorg. Chem.* 1978, **17** (12), 3615.

8. W.B. Heuer, A.E. True, P.N. Swepston and B.M. Hoffman, *Inorg. Chem.* 1988, **27** (8), 2003.

9. W. Kaim, *Coord. Chem. Rev.* 1987, **76**, 187.

10. G.A. Heath, L.J. Yellowlees and P.S. Braterman, *J. Chem. Soc. Chem. Commun.* 1981, 287.

11. S.P. Best, S.A. Ciniawasky, R.J.H. Clark and R.C.S. McQueen, *J. Chem. Soc. Dalton Trans.* 1993, 2267.

12. A.P. Koley, R. Nirmala, L.S. Prassad, S. Ghosh and P.T. Manoharan, *Inorg. Chem.* 1992, **31** (10), 1764.

13. S.M. Angel, M.K. De Armond, R.J. Donohoe, K.W. Hanck and D.W. Wertz, *J. Am. Chem. Soc.* 1984, **106** (3), 3688.

14. C.M. Elliot and E.J. Hershenhart, *J. Am. Chem. Soc.* 1982, **104** (26), 7519.

15. E. Konig and S. Kremer, *Chem. Phys. Lett.* 1970, **5**, 87.

16. V.T. Coombe, G.A. Heath, A.J. MacKenzie and L.J. Yellowlees, *Inorg. Chem.* 1984, **23** (21), 3423.

17. A.G. Motten, K. Hanck and M.K. De Armond, *Chem. Phys. Lett.* 1981, **79** (3), 541.

18. D.E. Morris, K.W. Hanck and M.K. De Armond, *J. Am. Chem. Soc.* 1983, **105** (10), 3032.

19. L. Persaud and C.H. Langford, *Inorg. Chem.* 1985, **24** (22), 3562.

20. A. Davidson, N. Edelstein, R.H. Holm and A.H. Maki, *J. Am. Chem. Soc.* 1963, **85** (2), 2029.

21. R.L. Schlupp, Ph.D. Thesis, 1973, Uni. of California at Riverside, USA.

22. R.D. Schmidtt and A.H. Maki, *J. Am. Chem. Soc.* 1968, **90** (2), 2288.

23. K.D. Bos, J.G. Kraaijkamp and J.G. Noltes, *Synth. Commun.* 1979, **9** (6), 497.

24. D. Wenkert and R.B. Woodward, *J. Org. Chem.* 1983, **48** (3), 283.

25. S. Anderson, E.C. Constable, K.R. Seddon, J.E. Turp, J.E. Baggott and M.J. Pilling, *J. Chem. Soc. Dalton Trans.* 1985, 2247.

26. G. Maerker and F.H. Case, *J. Am. Chem. Soc.* 1958, **80** (2), 2745.

27. M.J. Cook, A.P. Lewis, G.S.G. McAuliffe, V. Skerda, A.J. Thomson, J.L. Glasper and D.J. Robbins, *J. Chem. Soc. Perkin Trans. II* 1984, 1293.

28. G.T. Morgan and F.H. Burstall, *J. Chem. Soc.* 1934, 965.

29. H.M. Colquhoun, J.F. Stoddart, D.J. Williams, J.B. Wolstenholme and R. Zarzycki, *Angew. Chem. Int. Ed. Engl.* 1981, **20** (12), 1051.

30. E. Bielli, P.M. Gidney, R.D. Gillard and B.T. Heaton, *J. Chem. Soc. Dalton Trans.* 1974, 219.

31. L.A. Worf, R. Deusing, P. Chen, L.D. Ciana and T.J. Meyer, *J. Chem. Soc. Dalton Trans.* 1991, 849.

32. S.E. Livingstone and B. Wheelahan, *Aust. J. Chem.* 1964, **17**, 219.

33. B.J. McCormick, E.N. Jaynes, Jr. and R.I. Kaplan, *Inorg. Synth.* 1972, **13**, 217.

34. C. Cocevar, G. Mestroni and A. Camus, *J. Organomet. Chem.* 1972, **35**, 389.

35. G.Giordano and R.H. Crabbe, *Inorg. Synth.* 1978, **19**, 218.

36. International Tables for *X*-ray Crystallography, vol. 4; Kynoch Press, Birmingham, England, 1974.

37. G.M. Sheldrick, SHELX76, Program for Crystal Structure Determination and Refinement, 1976, Uni. of Cambridge, England.

38. R.O. Gould and P. Taylor, CALC, Program for Molecular Geometry Calculations, 1986, Uni. of Edinburgh, Scotland.

39. G.M. Sheldrick, SHELXTL/PC User's Manual, Siemens Analytical *X*-ray Instruments Inc., Madison, Wisconsin, USA.

40. N.G. Walker and D. Stuart, *Acta Cryst.* 1983, **A39**, 158.

41. J. Howell, A. Rossi, D. Wallace, K. Haraki and R. Hoffmann, ICON, QCPE, Uni. of Indiana, 1977, no. 353.

42. J.H. Ammeter, H-B. Burgi, J.C. Thibeault and R. Hoffmann, *J. Am. Chem. Soc.* 1978, **100** (12), 3686.

43. R.H. Herber, M. Croft, M.J. Coyer, B. Bilash and A. Sahiner, *Inorg. Chem.* 1994, **33** (11), 2422.

44. R. Osborn and D. Rogers, *J. Chem. Soc. Dalton Trans.* 1974, 1002.

45. C-M. Che, L-Y. He, C-K. Poon and T.C.W. Mak, *Inorg. Chem.* 1989, **28** (15), 3081.

46. S.A. Macgregor, E. McInnes, R.J. Sorbie and L.J. Yellowlees, *Molecular Electrochemistry of Inorganic, Bioinorganic and Organometallic Compounds* (A.J.L. Pombeiro and J.A. McCleverty eds.).,1993, 503.

47. D. Collison and F.E. Mabbs, Program for EPR Spectrum Simulation, Uni. of Manchester, England.

48. J.M. Rawson, Program for Isotropic EPR Spectrum Simulation, 1994, Uni. of Edinburgh, Scotland.

49. M. Maekawa, M. Munakata, S. Kitagawa and N. Nakamura, *Anal. Sci.*1991, **7**, 521.

50. A.J. Carty, B.W. Skelton, P.R. Traill and A.H. White, *Aust. J. Chem.* 1992, **45**, 417.

51. P.M. Gidney, R.D. Gillard and B.T. Heaton, *J. Chem. Soc. Dalton Trans.* 1973, 132.

52. D.L. Webb and L.A. Rossiello, *Inorg. Chem.* 1971, **10** (10), 2213.

53. V.M. Miskowski and V.H. Holding, *Inorg. Chem.* 1989, **28** (8), 1529.

54. V.M. Miskowski, V.H. Holding, C-M. Che and Y. Wang, *Inorg. Chem.* 1993, **32** (11), 2518.

55. R. Ballardini, M.T. Gandolfi, L. Prodi, M. Ciano, V. Balzani, F.H. Kohnke, H. Shahrini-Zavareh, N. Spencer and J.F. Stoddart, *J. Am. Chem. Soc.* 1989, **111** (18), 7072.

56. C-M. Che, K-T. Wan, L-Y. He, C-K. Poon and V.W-W. Yam, *J. Chem. Soc. Chem. Commun.* 1989, 943.

57. V.M. Miskowski and V. Holding, *Inorg. Chem.* 1991, **30** (23), 4446.

58. J.A. Zuleta, M.S. Burberry and R. Eisenberg, *Coord. Chem. Rev.* 1990, **97**, 47.

59. J.B. Cooper, S.M. Rhodes and D.W. Wertz, *J. Phys. Chem.* 1991, **95** (12), 4800.

60. P.S. Braterman, J-I. Song, C. Vogler and W. Kaim, *Inorg. Chem.* 1992, **31** (2), 222.

61. P.S. Braterman, J-I. Song, F.W. Wimmer, S. Wimmer, W. Kaim, A. Klein and R.D. Peacock, *Inorg. Chem.* 1992, **31** (24), 5084.

62. J.A. Zuleta, J.M. Bevilacqua, D.M. Prosperpio, P.D. Harvey and R. Eisenberg, *Inorg. Chem.* 1992, **31** (12), 2396.

63. M. Symons, Chemical and Biochemical Aspects of ESR Spectroscopy; Van Nostrand Reinhold, 1978.

64. N.C. Brown, G.A. Carriedo, N.G. Connelly, F.J.G. Alonso, I.C. Quarmby, A.L. Rieger, P.H. Rieger, V. Riera and M. Vivanco, *J. Chem. Soc. Dalton Trans.* 1994, 3745.

65. N.G. Connelly, W.E. Geiger, G.A. Lane, S.J. Raven and P.H. Rieger, *J. Am. Chem. Soc.* 1986, **108** (20), 6219.

66. J.S. Morton and K.F. Preston, *J. Magn. Reson.* 1978, **30**, 577.

67. C.P. Whittle, *J. Heterocyclic Chem.* 1977, **14** (1), 191.

68. M.K. Furue, K. Maruyama, T. Ogumi, H. Naiki and M. Kamachi, *Inorg. Chem.* 1992, **31** (8), 3792.

69. M.A. Weiner and A. Basu, *Inorg. Chem.* 1980, **19** (9), 2797.

70. A. Basu, H.D. Gafney and T.C. Strekas, *Inorg. Chem.* 1982, **21** (6), 2231.

71. A. Basu, M. Weiner, T.C. Strekas and H.D. Gafney, *Inorg. Chem.* 1982, **21** (3), 1085.

72. M.J. Cook, A.P. Lewis, G.S.G. McAuliffe, V. Skarda, A.J. Thomson, J.L. Glasper and D.J. Robbins, *J. Chem. Soc. Perkin Trans. II* 1984, 1303.

73. R.J. Donohoe, C.D. Tait, M.K. De Armond and D.W. Wertz, *J. Phys. Chem.* 1986, **90** (17), 3923.

74. R.J. Donohoe, C.D. Tait, M.K. De Armond and D.W. Wertz, *J. Phys. Chem.* 1986, **90** (17), 3927.

75. C. Hansch, A. Leo and R.W. Taft, *Chem. Rev.* 1991, **91** (2), 165.

76. J.A. Connor, C. Overton and N.E. Murr, *J. Organomet. Chem.* 1984, **277**, 277.

77. K-C. Shih and R.H. Herber, *Inorg. Chem.* 1992, **31** (26), 5444.

78. S. Dholakia, R.D. Gillard and F.L. Wimmer, *Polyhedron* 1985, **4** (5), 791.

79. W.A. Fordyce, K.H. Pool and G.A. Crosby, *Inorg. Chem.* 1982, **21** (3), 1027.

80. Vu Dong, H. Endres, H.J. Keller, W. Morani and D. Nöthe, *Acta. Cryst.* 1977, **C33**, 2428.

81. A. Hazell, O. Simonsen and O. Wernberg, *Acta. Cryst.* 1986, **C42** (2), 1707.

82. S. Maeda, Y. Nishida, H. Okawa and S. Kida, *Bull. Chem. Soc. Jpn.* 1986, **59** (6), 2013.

83. P. Chieh, *J. Chem. Soc. Dalton Trans.* 1972, 1643.

84. M. Hinamoto, S. Ooi and H. Kuraya, *J. Chem. Soc. Chem. Commun.* 1972, 356.

85. A.J. Carty and P.C. Chieh, *J. Chem. Soc. Chem. Commun.* 1972, 158.

86. J. Foley, S Tyagi and B.J. Hathaway, *J. Chem. Soc. Dalton Trans.* 1984, 1.

87. B. Balaiah, B.A. Sastry, M.N. Chary, G. Ponticelli and M. Massacesi, *J. Mol. Struct.* 1982, **78**, 289.

88. G. Kew, K. De Armond and K. Hanck, *J. Phys. Chem.* 1974, **78** (7), 727.

89. H. Cãldãraru, M.K. De Armond, K.W. Hanck and V.E. Sahini, *J. Am. Chem. Soc.* 1976, **98** (15), 4455.

90. L. Chassot and A. Von Zelewsky, *Inorg. Chem.* 1987, **26** (17), 2814.

91. P.S. Braterman, J-I. Song, F.W. Wimmer and S. Wimmer, *Inorg. Chim. Acta.* 1991, **189**, 7.

92. M. Maestri, D. Sandrini, V. Balzani, A. Von Zelewsky, C. Deuschel-Cornioley and P. Jolliet, *Helv. Chim. Acta.* 1988, **71**, 1053.

93. Y. Yamamoto, K. Takahashi and H. Yamakazi, *Chem. Lett.* 1985, **2**, 201.

94. Y. Yamamoto, K. Takahashi, K. Matsuda and H. Yamazaki, *J. Chem. Soc. Dalton Trans.* 1987, 1833.

95. Y. Yamamoto and H. Yamazaki, *Organomet.* 1993, **12** (3), 933.

96. C.M. Harris and T.N. Lockyer, *J. Chem. Soc. (A)* 1959, 3083.

97. V.W-W. Yam, S.W-K. Choi, T-F. Lai and W-K. Lee, *J. Chem. Soc. Dalton Trans.* 1993, 1001.